MINISTÉRIO DA CIÊNCIA, TECNOLOGIA E INOVAÇÕES
INSTITUTO NACIONAL DE PESQUISAS ESPACIAIS

sid.inpe.br/mtc-m21d/2022/09.08.19.55-TDI

STUDY AND ESTIMATION OF THE SOLAR MAGNETIC FIELD IN AR11967 USING INVERSION METHODS

Alexandre José Ranieri Sacata Diogo

Master's Dissertation of the Graduate Course in Space Geophysics, guided by Drs. Tardelli Ronan Coelho Stekel, and Luís Eduardo Antunes Vieira, approved in September 09, 2022.

URL of the original document:
<http://urlib.net/8JMKD3MGP3W34T/47JKDLH>

INPE
São José dos Campos
2022

PUBLISHED BY:

Instituto Nacional de Pesquisas Espaciais - INPE
Coordenação de Ensino, Pesquisa e Extensão (COEPE)
Divisão de Biblioteca (DIBIB)
CEP 12.227-010
São José dos Campos - SP - Brasil
Tel.:(012) 3208-6923/7348
E-mail: pubtc@inpe.br

MINISTÉRIO DA CIÊNCIA, TECNOLOGIA E INOVAÇÕES
INSTITUTO NACIONAL DE PESQUISAS ESPACIAIS

sid.inpe.br/mtc-m21d/2022/09.08.19.55-TDI

STUDY AND ESTIMATION OF THE SOLAR MAGNETIC FIELD IN AR11967 USING INVERSION METHODS

Alexandre José Ranieri Sacata Diogo

Master's Dissertation of the Graduate Course in Space Geophysics, guided by Drs. Tardelli Ronan Coelho Stekel, and Luís Eduardo Antunes Vieira, approved in September 09, 2022.

URL of the original document:
<http://urlib.net/8JMKD3MGP3W34T/47JKDLH>

INPE
São José dos Campos
2022

Cataloging in Publication Data

Diogo, Alexandre José Ranieri Sacata.

D621s Study and estimation of the solar magnetic field in AR11967 using inversion methods / Alexandre José Ranieri Sacata Diogo. – São José dos Campos : INPE, 2022.

xxx + 133 p. ; (sid.inpe.br/mtc-m21d/2022/09.08.19.55-TDI)

Dissertation (Master in Space Geophysics) – Instituto Nacional de Pesquisas Espaciais, São José dos Campos, 2022.

Guiding : Drs. Tardelli Ronan Coelho Stekel, and Luís Eduardo Antunes Vieira.

1. pyMilne. 2. Inversion. 3. Inverse problems. 4. AR11967. 5. Hinode mission. I.Title.

CDU 52:619.16

MINISTÉRIO DA CIÊNCIA, TECNOLOGIA E INOVAÇÕES

INSTITUTO NACIONAL DE PESQUISAS ESPACIAIS
Secretaria de Pós-Graduação - SEPGR

DEFESA FINAL DE DISSERTAÇÃO DE ALEXANDRE JOSÉ RANIEIRE SACATA DIOGO BANCA Nº 226/2022, REG 50826/2020

No dia 02 de setembro de 2022, por teleconferência, o(a) aluno(a) mencionado(a) acima defendeu seu trabalho final (apresentação oral seguida de arguição) perante uma Banca Examinadora, cujos membros estão listados abaixo. O(A) aluno(a) foi APROVADO(A) pela Banca Examinadora, por unanimidade, em cumprimento ao requisito exigido para obtenção do Título de Mestre em Geofísica Espacial/Ciências do Ambiente Solar-Terrestre. O trabalho precisa da incorporação das correções sugeridas pela Banca Examinadora e revisão final pelo(s) orientador(es).

Título: "STUDY AND ESTIMATION OF THE SOLAR MAGNETIC FIELD IN AR11967 USING INVERSION METHODS"

Membros da banca:

Dr. Alisson Dal Lago – Presidente – INPE
Dr. Tardelli Ronan Coelho Stekel – Orientador – IFSP
Dr. Joaquim Eduardo Rezende Costa – Membro Interno – INPE
Dra. Franciele Carlesso – Membro interno – INPE
Dr. Paulo José de Aguiar Simões – Membro externo – Mackenzie

Documento assinado eletronicamente por **Joaquim Eduardo Rezende Costa**, **Chefe da Divisão de Clima Espacial**, em 05/09/2022, às 14:37 (horário oficial de Brasília), com fundamento no § 3º do art. 4º do Decreto nº 10.543, de 13 de novembro de 2020.

Documento assinado eletronicamente por **Alisson Dal Lago**, **Chefe da Divisão de Heliofísica, Ciências Planetárias e Aeronomia**, em 05/09/2022, às 22:45 (horário oficial de Brasília), com fundamento no § 3º do art. 4º do Decreto nº 10.543, de 13 de novembro de 2020.

Documento assinado eletronicamente por **Paulo José de Aguiar Simões (E)**, **Usuário Externo**, em 15/09/2022, às 09:57 (horário oficial de Brasília), com fundamento no § 3º do art. 4º do Decreto nº 10.543, de 13 de novembro de 2020.

Documento assinado eletronicamente por **Tardellli Ronan coelho stekel (E)**, **Usuário Externo**, em 15/09/2022, às 11:35 (horário oficial de Brasília), com fundamento no § 3º do art. 4º do Decreto nº 10.543, de 13 de novembro de 2020.

Documento assinado eletronicamente por **Franciele carlesso (E)**, **Usuário Externo**, em 20/09/2022, às 09:04 (horário oficial de Brasília), com fundamento no § 3º do art. 4º do Decreto nº 10.543, de 13 de novembro de 2020.

A autenticidade deste documento pode ser conferida no site https://sei.mcti.gov.br/verifica.html, informando o código verificador **10317581** e o código CRC **6ED7AF34**.

Referência: Processo nº 01340.006664/2022-16 SEI nº 10317581

"Humility forms the basis of honor, just as the low ground forms the foundation of a high elevation.".

BRUCE LEE

I dedicate this work to the Brazilian nation which I have always sought to serve, and to my mother who has always been supportive and a reason to continue.

ACKNOWLEDGEMENTS

First, I would like to thank my supervisors Tardelli Ronan Coelho Stekel (PhD) and Professor Luís Eduardo Antunes Vieira (PhD) for accepting to guide me, for their patience, for the explanations and for helping me.
I would like to thank the Brazilian Ministry of Science, Technology and Innovation and the Brazilian Space Agency.
I would like to thank the CAPES agency for believing in me and for the financial support given to me through my scholarship. And I would also like to thank the Brazilian taxpayer who maintains the CAPES agency, which is a very important agency for Brazil.
I would like to deeply thank the National Institute for Space Research (INPE) for believing in me, for the chance given to me, for the knowledge I acquired, for the excellent services provided to Brazilian society, and for the services provided to national science. Thank you INPE for the excellent services provided to Brazil.
I would like to thank the professors I had at INPE, especially Professor Alisson Dal Lago, who always had a lot of patience to explain, to Professor Marcelo Banik de Pádua, for his patience in explaining topics related to computing.
I would like to thank my classmates for helping me a lot. I would like to thank the author of the pyMilne inversion code, Professor Jaime de la Cruz Rodríguez (PhD), for making the inversion code.
I would like to thank Professor Ivan Milic (PhD) and the NSO team for the excellent workshops that helped me a lot.
I would like to thank the Hinode Mission team. Hinode is a Japanese mission developed and launched by ISAS/JAXA, collaborating with NAOJ as a domestic partner, NASA and STFC (UK) as international partners. Scientific operation of the Hinode mission is conducted by the Hinode science team organized at ISAS/JAXA. This team mainly consists of scientists from institutes in the partner countries. Support for the post-launch operation is provided by JAXA and NAOJ (Japan), STFC (U.K.), NASA, ESA, and NSC (Norway).
And, above all, I am immensely grateful to my mother, Adriane Ranieri Sacata. My mother raised me alone, always made an effort to help me, always reinforced the importance of dedicating herself, my mother who always gave me support and a reason to continue. Thank you mom.

ABSTRACT

On February 4, 2014 around 19:00 UT, the Hinode Mission Solar Optical Telescope Spectropolarimetrer on booard of the Hinode satellite observed Active Region 11967, and using the inversion code Milne-Eddington gRid Linear Inversion Network (MERLIN), Hinode Mission was able to obtain several interesting and important data, such as line-of-sight velocity, damping, line-to-continuum absorption coefficient ratio, magnetic field inclination, magnetic field azimuth, magnetic field strength, among others, besides being able to observe a region that resembles a lightbridge where one of the strongest magnetic fields has ever been observed and which has a magnitude of approximately 6.2 kG. Our objective in this work is to study the active region 11967 observed on February 4, 2014 at 19:00 UT using the Milne-Eddington pyMilne inversion code, where we will try to obtain atmospheric parameters such as the intensity, inclination and azimuth of the magnetic field, line-of-sight velocity, in addition to comparing two different inversion codes (pyMilne and MERLIN), that is, comparing the results obtained by the codes. In addition, we will also study the region that resembles a lightbridge.

Keywords: pyMilne. Inversion. Inverse Problems. AR11967. Hinode Mission. Magnetic fields. Comparison.

ESTUDO E ESTIMATIVA DO CAMPO MAGNÉTICO SOLAR EM AR11967 USANDO MÉTODOS DE INVERSÃO

RESUMO

Em 4 de fevereiro de 2014, por volta das 19:00 UT, o Espectropolarímetro do Telescópio Óptico Solar da Missão Hinode a bordo do satélite Hinode observou a Região Ativa 11967, e usando o código de inversão Milne-Eddington gRid Linear Inversion Network (MERLIN). A missão Hinode conseguiu obter diversos dados interessantes e importantes, como velocidade de linha de visada, amortecimento, razão do coeficiente de absorção linha-contínuo, inclinação do campo magnético, azimute do campo magnético, intensidade do campo magnético, entre outros, além de poder observe uma região que se assemelha a uma lightbridge onde um dos campos magnéticos mais fortes já foi observado e que tem uma magnitude de aproximadamente $6,2$ kG. Nosso objetivo neste trabalho é estudar a região ativa 11967 observada em 04 de fevereiro de 2014 às 19:00 UT usando o código de inversão Milne-Eddington pyMilne, onde tentaremos obter parâmetros atmosféricos como intensidade, inclinação e azimute do campo magnético, velocidade de visada, além de comparar dois códigos de inversão diferentes (pyMilne e MERLIN), ou seja, comparar os resultados obtidos pelos códigos. Além disso, também estudaremos a região que se assemelha a uma lightbridge.

Palavras-chave: pyMilne. Inversão. Problemas Inversos. AR11967. Missão Hinode. Campo magnético. Comparações.

LIST OF FIGURES

Page

2.1 Image detailing solar structures and other phenomena on the Sun. 3
2.2 The Hertzsprung-Russell diagram. 4
2.3 Representation of the so-called *Butterfly Diagram* of sunspots. The image shows the fractional coverage of sunspots as a function of time and solar latitude. 13

3.1 Transversal Zeeman effect. When the magnetic field is perpendicular to the line-of-sight (LOS). The observer can visualize the π component, the σ_b component and the σ_r component and they are all linearly polarized. . 32
3.2 Longitudinal Zeeman effect. In this case, the LOS is parallel to the magnetic field and the observer can visualize only the σ_r and σ_b components, both circularly polarized and in opposite directions. 32
3.3 Here there is a more general view, where the polarization of the different Zeeman components is shown (which depend on the type of component and the angle between the observation direction and the magnetic field vector). 33
3.4 Anomalous Zeeman effect. Note the transition between energy levels for the absence and presence of the magnetic field. At both levels $J = 2$, then the upper and lower energy level split in the presence of a magnetic field. 38
3.5 Normal Zeeman effect. Transition between energy levels for the absence and presence of the magnetic field. Due to $J_l = 0$, the lowest energy level does not split in the presence of a magnetic field. When $J_u = 1$, the upper energy level splits into three different sublevels with the magnetic quantum numbers $M \in \{-1, 0, +1\}$. At the bottom, the spectral aspect for both cases. 40
3.6 The Zeeman effect and line separation on the Stokes I map in AR11967 (region where this work focuses). 40

4.1 Artist's conception of the Hinode satellite. The cylinder in the center (door open) is the SOT. The black box at the top is the EIS. Below the SOT we have the XRT (also with the port open). 54
4.2 Optical layout of the SOT including the OTA and the FPP. 57
4.3 Representation of the SOT. 58

4.4 Definition of polarization response matrix and error in polarization measurements. 63
4.5 Reformatted scientific data file format for SOT and XRT. 68

5.1 Note that in this case the Stokes profiles are out of scale, so it might be useful to add the weight ω_i so that the merit function χ^2 "feel" the others Stokes parameters. 72
5.2 With the ω_i weight multiplied the other Stokes profiles can be "felt" by the merit function which in turn makes them more "influential" in the merit function calculation. 72
5.3 The following is a representation of the general inverse problem. 73

6.1 AR11967 seen on the 4th of February 2014 around 19:00 UT. In the square, we highlight the region where a very strong magnetic field was observed. Such a magnetic field had a magnitude of approximately 6250 G. 79
6.2 AR11967 images by different Stokes parameters and at the wavelength of the second line of the $Fe\ I$. (a) corresponds to Stokes I, which indicates luminous intensity. (b) and (c) correspond to linear polarizations that indicate the intensity of the magnetic field parallel to the plane (ie the component parallel to the plane) and are the maps of Q (to (b)) and U (to (c)). While (d) indicates how perpendicular the field is to the plane, that is, the perpendicular component, in addition to corresponding to the Stokes V. 80
6.3 AR11967 with four points highlighted in red: (1) in a lightbridge, (2) in the sunspot, (3) and (4) in the quiet-Sun region. The white lines serve to indicate that the points (1) and (2) are collinear as are the points (3) and (4). 81
6.4 Full Stokes Spectra. The red lines correspond to the highlighted points. . 82
6.5 Here we have the observed profiles of Stokes at the height of 28.53 arcsec and passing and that correspond to the point (1) in 6.4. Note that in (a) we have several valleys of luminosity, the last three valleys that occur in a neighborhood of $6302,500$ Å, are a consequence of the division of the line responding to the Zeeman effect. In (b) and (c), we have the Stokes Q and U respectively, and in (d) the Stokes V. 83
6.6 Pixel profiles (2). In (a) the Stokes I, in (b) the Stokes Q, in (c) the Stokes U, and in (d) the Stokes V. The intense magnetic activity is observed in (a) and (d). The (2) pixel is a region of the sunspot umbra. 84

6.7 The following image illustrates the full Stokes spectra for the region where the second white line is located. As already mentioned, this region is an example of the quiet-Sun, which is a region characterized by low magnetic activity. Note that the lines remain well behaved. 84
6.8 In the following Stokes profiles, we have the spectra at the height of 28.53 arcsec in the blue color line and the spectra at the height of 47.55 arcsec, where in (a) we have the Stokes I, (b) the Stokes Q, (c) the Stokes U, and (d) the Stokes V. Note also that the behavior of the profiles observed are very similar. 85
6.9 Image of the continuum ad AR11967. The continuum image was obtained by averaging matrices of the spectral range from 6302.88 Å to 6303.10 Å. And the colorbar shows the intensity. 86
6.10 The following image shows $\mathbf{S}_{i,\lambda}$ for each of the $i \in \{I, Q, UV\}$ and for $\lambda = 6302,500$ Å. (a) $\mathbf{S}_{I,6302,500\text{ Å}}$. (b) $\mathbf{S}_{Q,6302,500\text{ Å}}$. (c) $\mathbf{S}_{U,6302,500\text{ Å}}$. (d) $\mathbf{S}_{V,6302,500\text{ Å}}$. 87
6.11 Below is the full Stokes spectra of the four Stokes parameters and indicating the location of the points (1), (2), (3) and (4) on the four red lines. The four full Stoke spectra of the first line show a region with strong magnetic activities. The four full Stokes spectra of the second row show a quiet-Sun region. 88
6.12 Stokes profiles for each of the points in Figure 6.3. Each Stokes parameter has four profiles. In (a) the Stokes I profiles. In (b) the Stokes Q profiles. In U the profiles of Stokes (U). In (d) the Stokes V profiles. In blue, we have the profiles of point (1). In yellow, the profiles of point (2). The green color represents the point profiles (3). And the profiles of point (4), are in red. 89
6.13 Synthetic lines with the parameter B varying and obtained with the initial guess atmosphere $\mathbf{x} = [0, \pi/4, 0.0, 0.0, 0.02, 30, 0.1, 0.2, 0.8]$. 91
6.14 Synthetic lines with the parameter θ varying and obtained with the initial guess atmosphere $\mathbf{x} = [2500, \pi/4, 0.0, 0.0, 0.02, 30.0, 0.1, 0.2, 0.8]$. 92
6.15 Synthetic lines with the parameter φ varying and obtained with the initial guess atmosphere $\mathbf{x} = [2500, \pi/2, \pi/8, 0.0, 0.02, 30.0, 0.1, 0.2, 0.8]$. 93
6.16 Synthetic lines with parameter υ_{LOS} varying and obtained with the initial guess atmosphere $\mathbf{x} = [2500, \pi/2, \pi/8, 0.1, 0.02, 30, 0.1, 0.2, 0.8]$. 94

6.17 Intensity of the continuum from Hinode/SOT observations of AR11967 showing the location of pixels that will be inverted through the inversion process. Four distinct points were selected to study different behaviors of different regions of the Sun. The (1) pixel is a region that resembles a lightbridge, the (2) pixel is an umbra region, the (3) pixel is a penumbra, and the (4) pixel is a quiet-Sun region. 97
6.18 Below, the comparison of the observed Stokes profiles (Obs) and the synthetic profiles (Fit). In *first column*, it is possible to observe the profiles at point (1), in *second column*, profiles at point (2), profiles at point (3) can be observed in *third column*, and those of point (4) in *fourth column*. 98

7.1 In the Figure on the left, we have the magnetic field module and highlight the sunspot umbra. On the right side, the function χ^2 limited between the values of 0 and 1000, which was limited to highlight that the largest errors occur in regions of intense magnetic field such as umbras and in the region that resembles to a lightbridge. 101
7.2 In the figures on the right we can see the modules of the magnetic field. And on the left side, the images of the merit function can be visualized. In the first row and column on the left, the magnetic field map has been restricted, while in the second row and first column, the magnetic field map across the entire AR is presented. In the two lines of the second column, two maps of χ^2 are presented, in the first line the map has a limiter and in the second line the map is without the limiter. With the limiter in the first row and second column, it serves to highlight that very large error values can be reached. Also in the second row and column, note that it is difficult to identify the error values. As stated in Figure 7.1, the regions where the electric field is more intense are where the highest values (errors) of the merit function χ^2 occur. 102
7.3 In *first line* we have $v_{LOS,pyMilne}$, in *second line*, $v_{LOS,MERLIN}$ and in *third line*, $v_{LOS,pyMilne} - v_{LOS,MERLIN}$. Teste 104
7.4 Images illustrating the strengths of magnetic fields and the difference between them. *First line*: magnetic field strength due to pyMilne. *Second line*: magnetic field strength due to MERLIN. *Third line*: difference between the magnetic field intensity maps ($B_{pyMilne} - B_{MERLIN}$). 107
7.5 Difference between magnetic field strengths, restricted between -1000 G and 1000 G. 108

7.6 Image illustrating the magnetic field vector inclinations and difference of inclinations. In *first line*: inclination due to pyMilne. *Second line*: inclination due to MERLIN. And *third line*: $\theta_{pyMilne} - \theta_{MERLIN}$. 111
7.7 On *left*, we have the magnitude of the magnetic field. And the *right*, the inclination map. Note that the strongest magnetic field has an inclination of approximately 90°. 112
7.8 Illustration of azimuth (with ambiguity) and the difference between azimuth. In *first line* the azimuth due to pyMilne, in *second line* the azimuth due to MERLIN, and in *third line* the difference between the azimuths ($\varphi_{pyMilne} - \varphi_{MERLIN}$). 115
7.9 Image highlighting the sunspot region (*left*) and the difference between maps $\varphi_{pyMilne} - \varphi_{MERLIN}$ (*right*). Note that a qualitative analysis shows that the maps of $\varphi_{pyMilne}$ and φ_{MERLIN} have small relative differences. . 116
7.10 Scatterplots of pyMilne results (vertical) and MERLIN results (horizontal). The red line represents one-to-one correspondence, and R^2 represents how accurate the statistical measure. 117
7.11 Histograms. In the *first line*, the results related to B. In *second line*, results related to θ, in *third line*, results related to φ and in *fourth line*, results related to v_{LOS}. Also, in *first column*, you are asked to see results from pyMilne, in *second column*, those from MERLIN, and the differences can be seen in *third* and *fourth* column, with a range constraint on the histograms of B, θ, and v_{LOS}. 119

LIST OF TABLES

Page

3.1 Types of Zeeman effects. 39

4.1 Hinode instrument characteristics. 59
4.2 Hinode telescopes. 60
4.3 Classification of polarimeter components. 65
4.4 Tolerance of polarization properties for each component. 65
4.5 Tolerance of polarization properties for each component. 67

6.1 In the table, we have the main characteristics and properties of $Fe\ I$, such as the central wavelengths λ_0, the excitation potential of the lower level χ_{low}, the electron configurations of the lower and upper levels, α is the value of the temperature exponent, σ is the value of the exponent of the cross section, and $\log(gf)$ is the strength of the line oscillator. 95

7.1 Avarage, median and kurtosis of the maps of $v_{LOS,pyMilne}$ and $v_{LOS,MERLIN}$. 103
7.2 Avarage, median and kurtosis table of magnetic field intensity maps. . . . 105
7.3 Avarage, median and kurtosis for maps $\theta_{pyMilne}$ and θ_{MERLIN}. 109
7.4 Avarage, median and kurtosis of pyMilne and MERLIN results for azimuth. 114

LIST OF ABBREVIATIONS

ACL	–	Astigmatism Correcting Lens
AR	–	Active Region
BFI	–	Broadband Filter Imager
CLU	–	Collimator lens unit
CME	–	Coronal mass ejaction
CSAC	–	Community Spectropolarimetric Analysis Center
CT	–	Correlation Tracker
CTM	–	Tip-tilt fold Mirror
DARTS	–	Data ARchive and Transmission System
DC	–	Direct Currents
EIS	–	EUV imaging spectrometer
EUV	–	extreme ultraviolet
FFP	–	Focal Plane Package
FG	–	Filtergraph
FITS	–	Flexible Image Transport System
GSST	–	Galileo Solar Space Telescope
INPE	–	Instituto Nacional de Pesquisas Espaciais
LOS	–	line-of-sight
LTE	–	Local Thermodynamic Equilibrium
ME	–	Milne-Eddington
MERLIN	–	Milne-Eddington gRid Linear Inversion Network
MHD	–	Magnetohydrodynamics
NFI	–	Narrowband Filter Imager
OSO	–	Orbiting Solar Observatory
OTA	–	Optical Telescope Assembly
PMU	–	Polarization Modulator Unit
pp	–	proton-proton
RTE	–	Radiative Transfer Equation
SOT	–	Solar Optical Telescope
SP	–	SpectroPolarimeter
XRT	–	X-Ray Telescope

LIST OF SYMBOLS

c	–	speed of light in vacuum
E	–	Energy
γ	–	gamma ray
ν_e	–	neutrino
p or ^1H	–	proton
e^+	–	positron
e^-	–	antiproton
r_b	–	base of convection zone
r_t	–	location of the tachocline shifts upward
$R_\odot$	–	Solar radius
ϵ	–	dielectric permittivity
μ	–	magnetic permeability
σ	–	conductivity
ρ	–	charge density
$\mathbf{J}$	–	electric current density
$\mathbf{E}$	–	electric field
$\mathbf{r}$	–	position vector
$\hat{\mathbf{s}}$	–	propagation direction vector
ω	–	angular frequency
$\mathbf{k}$	–	wave vector
C	–	polarization tensor or coherence matrix
$\mathbf{p}$	–	polarization vector
p	–	degree of polarization of the beam
$\mathbf{I}_{in}$	–	incident Stokes vector
$\mathbf{I}_{out}$	–	output Stokes vector
$\mathbf{M}$	–	Müeller matrix
$\mathbf{I}$	–	Stokes Vector
$\mathbf{I}^{Syn}$	–	Synthetic Stokes Vector
$\mathbf{I}^{Obs}$	–	Observed Stokes Vector
$\mathbf{I}_d$	–	Identity Matrix
I	–	Stokes I
Q	–	Stokes Q
U	–	Stokes U
V	–	Stokes V
$\mathbf{R}_M$	–	Müeller rotation matrix
ν_L	–	Lamor frequency
σ_b	–	σ blue component
σ_r	–	σ red component
π	–	π component
g_L	–	Landé factor
M	–	magnetic quantum number
g_{eff}	–	effective Landé factor
$\mathbf{K}$	–	propagation matrix

B_ν	–	Plank function
$\mathbf{S}$	–	Source function
χ_{cont}	–	continuum absorption coefficient
χ_{lin}	–	linear absorption coefficient
η_0	–	line-to-continuum absorption coefficient ratio
τ_c	–	continuum optical depth
$\mathcal{H}$	–	Voigt function
$\phi_{-1,0,+1}$	–	absorption profile
$\psi_{-1,0,+1}$	–	dispersion profile
$\mathbf{O}$	–	evolution operator
$\hbar$	–	reduced Planck constant
λ	–	wavelength
$\mathbf{X}$	–	response matrix
χ^2	–	Merit Function
σ_i	–	uncertainty in the measurement of the Stokes parameter i in merit function
ω_i	–	weights in merit function
$\mathbf{I}_{cont}$	–	continuum image
$\mathbf{S}_{i,\lambda}$	–	continuum images from $\mathbf{I}_{cont}$
$\mathbf{M}_{i,\lambda}$	–	image matrix of Stokes parameters generated at wavelength λ
$\mathbf{x}$	–	model atmosphere
B	–	intensity of magnetic field
θ	–	inclination of the magnetic field
φ	–	azimuth of the magnetic field
υ_{Dopp}	–	line-of-sight velocity
$\Delta\lambda$	–	Doppler width
a	–	damping
$\mathbf{B}$	–	Magnetic field vector

CONTENTS

Page

1 INTRODUCTION 1
1.1 Motivation 1
1.2 Overview 2

2 THE STRUCTURE OF THE SUN 3
2.1 The interior of the Sun 4
2.1.1 Solar Core 4
2.1.1.1 The production of energy inside the Sun 5
2.1.2 Radiative zone 9
2.1.3 Tachocline 9
2.1.4 Convective zone 10
2.2 Solar Atmosphere 11
2.2.1 Photosphere 11
2.2.1.1 Sunspots 11
2.2.1.2 Active Region 13
2.2.2 Chromosphere 14
2.2.3 Solar Corona 14
2.2.3.1 Coronal heating problem and Hinode Mission 16

3 SPECTROPOLARIMETRY AND POLARIZED LIGHT 19
3.1 Description of polarized light by Stokes parameters 19
3.2 Mueller matrices 26
3.3 Spectral line $Fe\ I$ 30
3.4 Zeeman effect 31
3.4.1 Classical case 34
3.4.2 Anomalous (or Quantum) case 36
3.5 Radiative Transfer Equation 41
3.5.1 Introduction and Local Thermodynamic Equilibrium (LTE) 41
3.5.2 Relationship between spectral line formation and RTE 44
3.5.3 Solution of the RTE 48
3.6 Milne-Eddington approximation 51

4 METHODOLOGY, DATA AND HINODE MISSION 53

4.1 Hinode Mission . . . 53
4.2 SpectroPolarimeter (SP) . . . 57
4.3 Polarization calibration of the SOT . . . 61
4.4 Data description . . . 66

5 INVERSION METHODS . . . 71
5.1 The inverse problem . . . 71
5.2 Levenberg-Marquardt algorithm . . . 73
5.3 The Milne-Eddington gRid Linear Inversion Network: MERLIN . . . 76
5.4 pyMilne . . . 77

6 RESULTS AND COMPARISONS . . . 79
6.1 The Hinode Mission observations . . . 79
6.2 Continuum . . . 86
6.3 Synthetic lines . . . 90
6.4 Inversion results: pyMilne . . . 95

7 RESULTS: pyMilne vs. MERLIN . . . 101
7.1 The merit function . . . 101
7.2 Line-of-sight velocity . . . 103
7.3 The magnetic field . . . 105
7.3.1 The intensity . . . 105
7.3.2 Inclination . . . 109
7.3.3 Azimuth . . . 113
7.4 Other comparison methods . . . 117

8 SUMMARY AND CONCLUSIONS . . . 121

REFERENCES . . . 125

1 INTRODUCTION

The objective of this work is to make an accurate inference of the photospheric solar magnetic field in the Active Region (AR) 11967, observed by the Hinode Mission (KOSUGI et al., 2007) on February 4, 2014, around 19:00 UT in addition to comparing the results of our inversion with the results obtained by the MERLIN inversion code. Therefore, we will study, analyze and discuss the magnetic field, as well as other elements of the atmospheric model considered may also be studied throughout the work. Theoretical topics such as Spectropolarimetry, Zeeman Effect, Radiative Transfer Equation and Inversion, spectral line $Fe\ I$ are addressed throughout the dissertation to give theoretical basis to the work.

To obtain the results, we chose to proceed assuming a Milne-Eddington approximation/atmosphere, as well as the code that will be used, which is also Milne-Eddington (pyMilne). This choice was due to the great utility of Milne-Eddington inversion codes for the study of solar magnetic fields in the atmospheric layers of the Sun.

The choice of AR11967 observed on February 4, 2014, was due to the abundance of research and observations that can be made in the region. For example, in this region we can observe quiet-Sun, sunspots, and their components such as umbra and penumbra, and we can also observe a region that resembles a light bridge, a region that is a subject of debate.

1.1 Motivation

The motivation is the inference of the photospheric magnetic field in AR11967. But the study of this work will be with an inversion code different from the MERLIN (LITES et al., 2007) which is the code used in the Hinode Mission. The inversion code chosen was pyMilne (RODRÍGUEZ, 2019), together with the data from the Hinode Mission.

Among the applications that can be highlighted, we can mention the construction of images of magnetic structures in the photosphere of the Sun, inference of atmospheric parameters, applications in stellar analysis (which is more general than solar analysis), the implications and extrapolations that can be made to from the results. Which will be discussed here, application to space weather, applications to the study of the Earth-Sun system and the environment in that system, and so on.

Another motivation for developing this work is the Galileo Solar Space Telescope (GSST) project, which is being developed by the Instituto Nacional de Pesquisas

Espaciais (INPE). This project aims to accurately measure the magnetic field of the solar photosphere and other atmospheric layers, in addition to providing Brazil with solar observation capabilities.

1.2 Overview

In Chapter 2, is dedicated to the study of the Sun, as well as its properties, behavior, structures and characteristics. In addition all layers will be detailed.

In Chapter 3, it is be our theoretical basis for building our results. In this chapter, we are dedicated to studying Spectropolarimetry in general, where it is carefully detailed. We will start from the initial formalization where an expression for the electric and magnetic fields is found, until we reach the solution of the Radiative Transfer Equation.

Chapter 4 is dedicated to presenting the Hinode Mission, the details of the Hinode Mission instruments and the details of the data used by the mission.

In Chapter 6, results obtained and information contained in plots, histograms, scatter plots, interpretations and so on will be presented. Furthermore, we will present the plots of the active region studied at a given wavelength, the *continuum* (map and profiles), spectral line map of Stokes parameters, synthetic profiles (compared to the observed).

In Chapter 7, is a chapter dedicated to presenting our main results, and comparing our results with the results of the MERLIN inversion code. Module of the magnetic field, line-of-sight velocity, azimuth, magnetic field inclination will be present in this Chapter. Furthermore, the outputs obtained with the pyMilne code will be compared with the outputs obtained by the MERLIN Code from the Hinode mission. And finally, a discussion of a recent scientific debate involving Lightbridges.

In Chapter 8, we present the conclusions and concluding remarks, in addition to a short summary of the work.

2 THE STRUCTURE OF THE SUN

The structures of the Sun are: core, radiation zone, convection zone and the solar atmosphere. The solar core, the radiation (or radiative) zone and the convection (or convective) zone make up the so-called solar interior; and the photosphere, chromosphere and solar corona make up the solar atmosphere. Each structure is detailed in Figure 2.1, where we have the structure of the Sun and other phenomena that can be observed.

Figure 2.1 - Image detailing solar structures and other phenomena on the Sun.

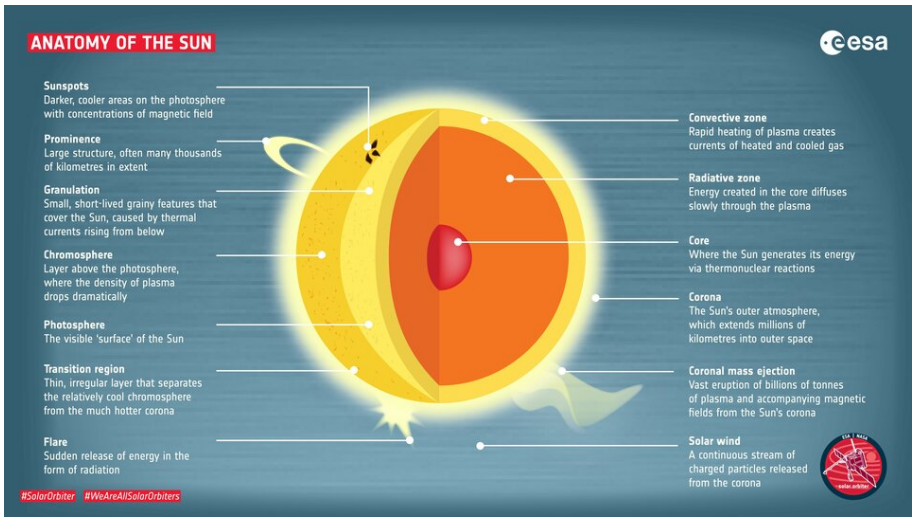

SOURCE: European Space Aagency (ESA) (2020).

The Sun is in the G2V spectral class, where G2 means that the Sun has a temperature of approximately 5780K making its color white (yellow dwarf) and V (5 in Romans) indicates that the Sun is part of the so-called Main Sequence (band of stars in the Hertzsprung-Russell diagram that relates luminosity and temperature on the surface of stars, as we can see in Figure 2.2).

The Sun has spectral lines of ionized and neutral metals such as $Fe\ I$, which will be our object of investigation and will be used.

Figure 2.2 - The Hertzsprung-Russell diagram.

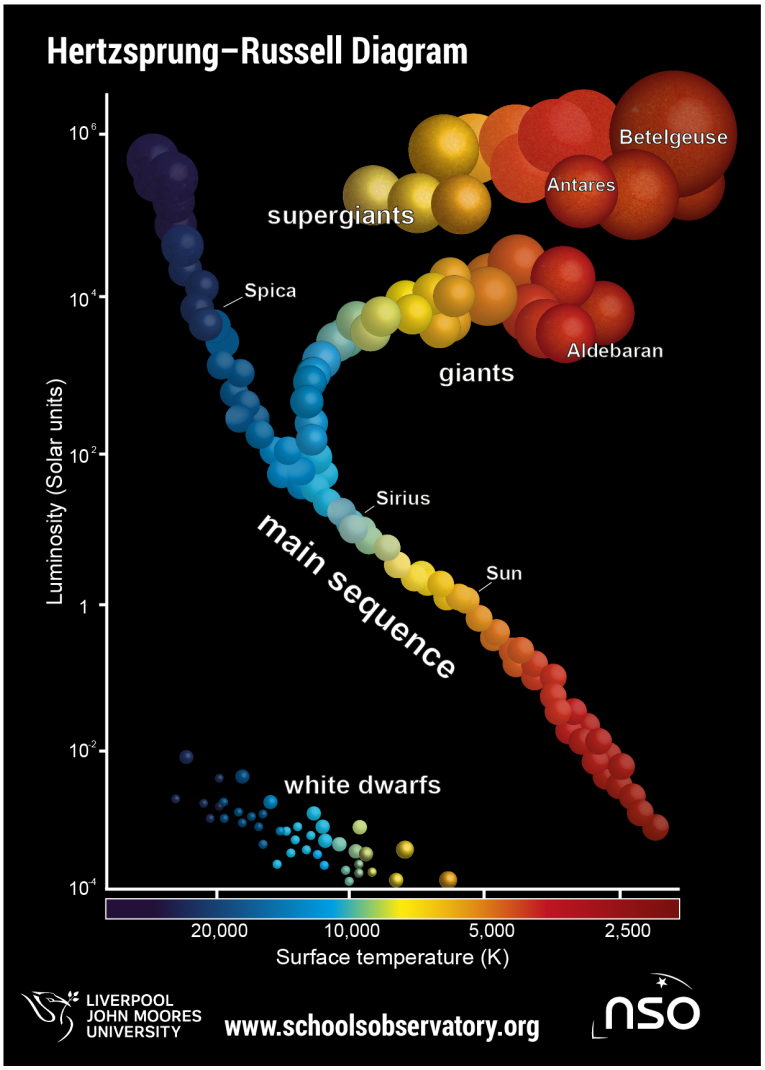

SOURCE: National Schools' Observatory (NSO) (2022).

2.1 The interior of the Sun

Physical laws such as conservation of mass, conservation of momentum, description of equilibrium, and energy transport must be obeyed by the model that governs the internal structure of the Sun (FRANZ, 2011).

2.1.1 Solar Core

The *solar core* is the central part of the Sun, comprising 10% of the solar mass and the region where nuclear fusion takes place that converts hydrogen into helium

(see 2.1.1.1) in addition to being the hottest region of the Solar System with temperatures that can reach $1.45 \cdot 10^7$ $^{\circ}C$ ($1.450027315 \cdot 10^7$ K) (NARAYANAN, 2013). The core is very dense due to the enormous gravitational compression of the other solar layers. The core is the most unknown part of the Sun as it cannot be directly observed. Therefore, to study the solar core, we need the help of Helioseismology, which through the study of solar oscillations, can study the behavior of the solar interior (BASU; ANTIA, 2007).

The solar core is mainly composed of hydrogen ($\approx$ 70%) and helium ($\approx$ 25%). However, and with much smaller amounts of heavier elements, including oxygen, carbon, neon, and iron (BASU; ANTIA, 2007). As the Sun ages, the amount of helium increases, and the amount of hydrogen decreases due to nuclear fusions that convert hydrogen into helium (AGOSTINI et al., 2020). The core produces almost all of the Sun's heat. The energy produced by core fusion travels through many successive layers to the solar photosphere before escaping into space as sunlight, kinetic, or thermal energy from massive particles.

2.1.1.1 The production of energy inside the Sun

With regard to energy production within the Sun, it is known that energy will be produced in the solar core. More precisely, the solar core is the source of energy, since nuclear fusion reactions that convert hydrogen to helium take place in the core, and therefore, a lot of energy is being released, such a mechanism of fusion of hydrogen into helium is the mechanism that generates solar energy (SEVERINO, 2017). In the case of the Sun, according to Severino (2017), there are two nuclear fusion reactions that generate energy: proton-proton cycle (pp) and CNO cycle (CNO). Furthermore, according to Degl'Innocenti (2007), there are three chains of pp reactions: ppI, ppII, ppIII. Let m_p be the mass of the proton, m the mass of the electron and m_α the mass of the particle α (or helium nucleus) and, knowing that the final result is the fusion of four protons and two electrons with the production of energy, according to Einstein (1905),

$$E = \Delta m c^2 = (4m_p + 2m - m_\alpha)c^2$$

and substituting the constant values,

$$\frac{\Delta m}{4m_p} = 0.00712$$
$$E = 26.73\text{MeV} = 4.28262000309 \cdot 10^{-12}\ \text{J}$$

The first step of the ppI cycle is the fusion of two protons (denoted by p or ^1H) in a deuterium nucleus with the formation of a neutrino and a positron, and producing 0.250 MeV energy (which will be taken with the neutrino because they interact very weakly with matter and will not be disturbed in the other layers of the Sun) and 1.192 MeV energy (which will not be taken by the neutrino). Therefore, the energy equation is written as follows

$$^1H + {}^1H \rightarrow {}^2H + e^+ + \nu_e + 1.442\text{MeV}\ (1.192\ \text{MeV} + 0.25\ \text{MeV}) \tag{2.1}$$

Furthermore, the energy release on the right side of the Equation 2.1 includes the average energies of the resulting particles and the photons emitted in the reaction. With this, the positrons and electrons annihilate each other releasing two γ rays,

$$e^+ + e^- \rightarrow 2\gamma$$

The deuterium (^2H) from the Equation 2.1, fuses with another proton generating a nucleus of ^3H, in addition to rays γ and 5.494 MeV of energy, as follows

$$^2H + {}^1H \rightarrow {}^3He + \gamma + 5.494\ \text{MeV} \tag{2.2}$$

From this point on, one can also obtain the reaction chains ppII and ppIII, which are other possibilities to obtain ^4He. It should be noted that at the end there will be three chains: ppI, ppII and ppIII.

To complete the ppI chain, two nuclei of ^3He will result in a nucleus ^4He (which is the final result) plus two protons and 12.86 MeV of energy,

$$^3He + {}^3He \rightarrow {}^4He + {}^1H + {}^1H + 12.86\ \text{MeV} \tag{2.3}$$

And taking the Equations 2.1, 2.2 and 2.3, we have the cycle ppI:

$$
\begin{aligned}
&{}^1H + {}^1H \rightarrow {}^2H + e^+ + \nu_e + 1.442\text{MeV } (1.192 \text{ MeV} + 0.25 \text{ MeV}) \\
&{}^2H + {}^1H \rightarrow {}^3He + \gamma + 5.494 \text{ MeV} \\
&{}^3He + {}^3He \rightarrow {}^4He + {}^1H + {}^1H + 12.86 \text{ MeV}.
\end{aligned}
$$

With the resulting ^3He from the Equation 2.2, the cycles ppII and ppIII can be obtained. In the ppII cycle, the ^3He fused with ^4He thus generating a nucleus ^7Be, rays γ and 1.588 MeV of energy, as in the following equation

$$
{}^3He + {}^4He \rightarrow {}^7Be + \gamma + 1.588 \text{ MeV} \tag{2.4}
$$

the nucleus ^7Be generated in the Equation 2.4 fused with a positron giving a nucleus ^7Li, rays γ and 0.862 MeV of energy,

$$
{}^7Be + e^- \rightarrow {}^7Li + \nu_e + \gamma + 0.049 \text{ MeV} + 0.813 \text{ MeV}. \tag{2.5}
$$

When the nucleus ^7Li generated in the Equation 2.5 fused with a proton, the last equation of the ppII cycle is obtained

$$
{}^7Li + {}^1H \rightarrow {}^4He + {}^4He + 17.346 \text{ MeV}. \tag{2.6}
$$

With the Equations 2.1, 2.2, 2.4, 2.5 and 2.6, the ppII cycle is written below

$$
\begin{aligned}
&{}^1H + {}^1H \rightarrow {}^2H + e^+ + \nu_e + 1.442 \text{ MeV } (1.192 \text{ MeV} + 0.25 \text{ MeV}) \\
&{}^2H + {}^1H \rightarrow {}^3He + \gamma + 5.494 \text{ MeV} \\
&{}^3He + {}^4He \rightarrow {}^7Be + \gamma + 1.588 \text{ MeV} \\
&{}^7Be + e^- \rightarrow {}^7Li + \nu_e + \gamma + 0.049 \text{ MeV} + 0.813 \text{ MeV} \\
&{}^7Li + {}^1H \rightarrow {}^4He + {}^4He + 17.346 \text{ MeV}.
\end{aligned}
$$

Once you have the nucleus ^{7}Be that was generated in the Equation 2.4, the fusion of ^{7}Be with a proton, results in a nucleus ^{8}B, rays γ plus 0.137 MeV energy. The core ^{8}B in turn decays into $^{8}Be^{*}$, depositon, ν_e and 15.1 MeV of energy. See the equations below:

$$^{7}Be +^{1} H \rightarrow^{8} B + \gamma + 0.137 \text{ MeV} \tag{2.7}$$

$$^{8}B \rightarrow ^{8}Be^{*} + e^{+} + \nu_e + 7.9 \text{ MeV} + 7.2 \text{ MeV} \tag{2.8}$$

where * means unstable kernel. The unstable core $^{8}Be^{*}$ decays into two cores of ^{4}He in addition to 2.995 MeV of energy, as in the following equation

$$^{8}Be \rightarrow ^{4}He +^{4} He + 2,995 \text{ MeV}. \tag{2.9}$$

And with the Equations 2.1, 2.2, 2.4, 2.5, 2.7, 2.8 and 2.9 the ppIII cycle follows

$$^{1}H + ^{1}H \rightarrow ^{2}H + e^{+} + \nu_e + 1.442 \text{ MeV } (1.192 \text{ MeV} + 0.25 \text{ MeV})$$
$$^{2}H + ^{1}H \rightarrow ^{3}He + \gamma + 5.494 \text{ MeV}$$
$$^{3}He +^{4} He \rightarrow ^{7}Be + \gamma + 1.588 \text{ MeV}$$
$$^{7}Be +^{1} H \rightarrow^{8} B + \gamma + 0.137 \text{ MeV}$$
$$^{8}B \rightarrow ^{8}Be^{*} + e^{+} + \nu_e + 7.9 \text{ MeV} + 7.2 \text{ MeV}$$
$$^{8}Be^{*} \rightarrow ^{4}He +^{4} He + 2.995 \text{ MeV}.$$

In addition to the proton-proton cycle, there is also the CNO cycle, which consists of another cycle of nuclear fusions that generate ^{4}He. This cycle is also called the Bethe-Weizsäcker cycle. The CNO cycle is equated below

$$
\begin{aligned}
&^{12}C + ^{1}H \rightarrow ^{13}N + \gamma + 1.944 \text{ MeV} \\
&^{13}N \rightarrow ^{13}C + e^{+} + \nu_e + 1.510 \text{ MeV} + 0.071 \text{ MeV} \\
&^{13}C + ^{1}H \rightarrow ^{14}N + \gamma + 7.551 \text{ MeV} \\
&^{14}N + ^{1}H \rightarrow ^{15}O + \gamma + 7.297 \text{ MeV} \\
&^{15}O \rightarrow ^{15}N + e^{+} + \nu_e + 1.752 \text{ MeV} + 1.00 \text{ MeV} \\
&^{15}N \rightarrow ^{4}He + ^{12}C + 4.966 \text{ MeV}.
\end{aligned}
$$

It is important to note (and it can also be noted in the set of equations for the CNO cycle) that the isotopes C, N, and O act as catalysts, and the cycle reactions do not affect their numerical densities and furthermore, the CNO cycle only contributes 1.2 % in total solar energy (SEVERINO, 2017). However, it seems that the CNO cycle tends to replace the proton-proton cycle as the Sun ages (AGOSTINI et al., 2020).

Depending on the temperature, chemical abundances, and density, the three cycles have different efficiencies, ie different contributions, with the ppI cycle being the most efficient, contributing 86 %. The ppII cycle contributes 14 % and the ppIII cycle contributes 0.11 % (DEGL'INNOCENTI, 2007).

2.1.2 Radiative zone

The *radiation zone* is the layer of the Sun that transports energy through radiation, which gives the layer its name. In this region, one can also observe transport of energy (in the form of radiation) from warmer regions to colder regions, a behavior that is also observed in the solar core. The energy generated in the nucleus is transported by photons that jump between particles in the radiative zone, such behavior of jumping between particles is called *random walk*. Although photons travel at the speed of light, the dense material in the radiation zone causes photons to take a long time to leave this solar layer. Estimates made show that assuming a random path, the travel time is $1.7 \cdot 10^5$ years (MITALAS; SILLS, 1992).

2.1.3 Tachocline

Between the radiative zone and the convective zone, there is a region that separates the two zones and has a mass of approximately 0.3 solar masses, the *tachocline*. The tachocline is the region that marks the transition between the radiation zone, where the rotational movement is analogous to that of a rigid body, and the convection

zone, where the rotational movement is differential, that is, it behaves like a fluid. Furthermore, the tachocline can be defined through its rotation behavior where, as already mentioned, the tachocline marks the transition between a uniform rotation and a differential rotation. Such a property results in a large shear between the two regions (successive horizontal layers slide over each other), for more information Tobias (2005) can be consulted.

According to Miesch (2005), estimates made by Charbonneau et al. (1999) and Basu and Antia (2003), show that the tacholine is centered $r_t \sim 0.693 \pm 0.003 R_\odot$ in the neighborhood of the equator, implying that the tachocline would be below the base of the convection zone $r_b = 0.713 \pm 0.003 R_\odot$. The tachocline shifts upwards at higher latitudes, where it reaches $r_t \sim 0.717 \pm 0.003 R_\odot$ (MIESCH, 2005).

For Charbonneau et al. (1999), the transition can be characterized by the following error function

$$f(r; r_t, \Delta_t) = \frac{1}{2}\left(1 + erf\left[\frac{2(r - r_t)}{\Delta_t}\right]\right),$$

and then estimating the best fit parameters using various inversion techniques.

The tachocline is believed to play a key role in solar dynamo and maintenance of magnetic activity (TOBIAS; WEISS, 2007).

2.1.4 Convective zone

The *convective zone* is the region where energy transport takes place by convection. The results of nuclear fusion reactions that take place in the solar core are transported by fluid movements. The convective zone is the outermost layer of the solar interior and extends to a depth of approximately 200000 km to the solar photosphere. The temperature at the base of the convection zone is approximately $2.00027315 \cdot 10^6$ K, and at the top (near the solar photosphere) is approximately $5.97315 \cdot 10^3$ K. It can also be noted that in the convection zone the energy transport occurs much faster than in the radiation zone.

Convection plays a very important role in the dynamics and evolution of the Sun and other stars. Convection is nothing more than the process of energy transport that takes place through mass movements (fluids). More formally, in an eddy, a part of the fluid mass that is locally hot rises towards the surface (because it is lighter

than the medium surrounding the fluid) and then cools. Once cooled, this fluid mass sinks as it becomes heavier (locally). The process described above occurs again upon reaching the bottom due to the heating of the fluid material. Such a process, which occurs continuously, tends to reduce the temperature gradient, that is, to homogenize the temperature throughout the layer. The entropy gradient is fundamental to describing and characterizing the convective behaviors in the strongly stratified convective layer. Stratification is close to adiabatic when convection is very efficient. The convective motions observed in the Sun have triggered near the system boundary in the so-called thermal (can be hot or cold) boundary layers from which plumes of intense vorticity detach opposite boundary is reached (BRUN; REMPEL, 2009).

2.2 Solar Atmosphere

The *solar atmosphere* is composed of the photosphere, chromosphere and solar corona. Much of the light we receive from the Sun is generated and emitted by the solar photosphere and passes through the chromosphere and corona. Most solar physics studies focus on the solar atmosphere, since spectropolarimetric analyzes are performed in the three regions using different spectral lines. In particular, this work will also focus on the solar atmosphere, more specifically on the structure called the solar photosphere.

2.2.1 Photosphere

The *Solar Photosphere* is the region of the Sun where light is radiated. It corresponds to the visible part of the Sun that is approximately 500 km thick, a temperature of approximately 5840 K that emits a continuous spectrum (NARAYANAN, 2013). It is the first layer of the solar atmosphere.

2.2.1.1 Sunspots

Sunspots are magnetic structures that appear dark on the solar surface (SOLANKI, 2003). Sunspots are characterized by *umbra* (dark and central region in the sunspotand where the magnetic field vector is vertical) and *penumbra* (less dark region of the sunspot that surrounds the umbra and where the magnetic field vector is horizontal).

The magnetic field was proposed to be the cause of sunspots in 1908 due to the work of George Ellery Hale, as he was the first to measure magnetic fields in sunspots (HALE, 1908).

Although details of sunspot formation are a research topic, as the formation process is still not well understood, it is widely accepted that sunspots result from visible manifestations of magnetic flux tubes in the Sun's convective zone that emerge in the photosphere within the active regions (SOLANKI, 2003). A sufficiently strong emerging magnetic field will cause an inhibition of convection and, as a consequence, the characteristic darkening of the sunspot. In addition, the energy flux from the interior of the Sun will decrease and therefore there will be a drop in temperature at the surface (photosphere), causing the temperature in the sunspot to be lower than in the sorrounding photosphere. Before they become sunspots, the spots appear as *pores* (small, dark, non-dark spots), and over time, the pores increase in size and move towards other pores. This process continues until they are big enough that the penumbra starts to form (SOLANKI, 2003).

According to Kubo (2018), three capabilities are needed in an instrument to understand the process of sunspot formation, they are:

1. spatial resolution to observe magnetoconvection, as magnetoconvection are essential for the formation of fine-scale structures within sunspots;

2. wide field of view to cover sunspot growth;

3. continuous observations to observe the evolution of magnetic elements;

It is believed that the Hinode Mission SOT 4.2 satisfies the three conditions listed above, however, it is currently impossible to predict where the sunspot will rise, and therefore, the SOT still cannot perfectly capture the evolution of sunspots in the quiet sun (KUBO, 2018).

The *butterfly diagram* of sunspots (see Figure 2.3) is very useful to study the decay behavior of sunspots as it shows the cyclic polarity exchange. In addition, the butterfly diagram has the following characteristics that can be highlighted (CHARBONNEAU, 2020):

1. Sunspots are restricted to latitudinal bands about 30 m wide, symmetrical about the equator;

2. Over the cycle, sunspots appear closer and closer to the equator, where peak coverage is reached at about 15 ° latitude;

3. The spatiotemporal variations of sunspot coverage are well synchronized in the two solar hemispheres.

According to Parker (1955) and Parker (1975), sunspot formation occurs when toroidal flux cords emerge through the convective envelope and emerge in the photosphere. Suppose such flux cords rise radially and are formed where the magnetic field is strongest, then the butterfly diagram provides an interpretation of a space-time map of the internal toroidal magnetic field component. It is worth remembering that in research on sunspots, such an interpretation is not unique.

Figure 2.3 - Representation of the so-called *Butterfly Diagram* of sunspots. The image shows the fractional coverage of sunspots as a function of time and solar latitude.

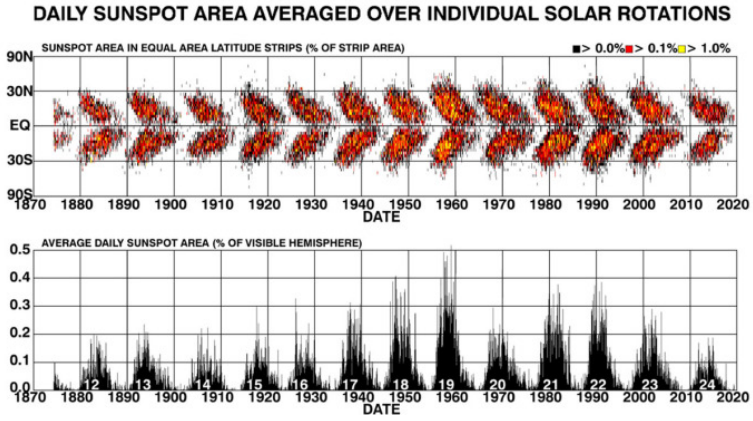

SOURCE: Charbonneau (2020).

2.2.1.2 Active Region

An *active region in the solar atmosphere* or simply *active region* (AR) is a region in the solar atmosphere characterized by being temporary and having a very strong and complex magnetic field. In the solar photosphere, active regions are associated with sunspots (see 2.2.1.1).

In particular, this study will focus on AR11967 around 19 UT on 2014 February 4. In this active region on that date, one of the strongest magnetic fields was observed (see Durán et al. (2020) and Okamoto and Sakurai (2018)).

The Hinode Mission observed AR11967 using the Spectropolarimeter (SP) which is an instrument of the Solar Optical Telescope (SOT) (see 4.2). Using the Milne-

Eddington MERLIN inversion code (see 5.3), magnetic field, fill factor, Doppler velocity, and so on, were obtained from AR11967 (OKAMOTO; SAKURAI, 2018).

2.2.2 Chromosphere

The *chromosphere* or *solar chromosphere* is a thin, irregular layer above the photosphere and below the transition region where the temperature increases with height. Temperatures in this region of the Sun range from $6.27315 \cdot 10^3$ K to $2.027315 \cdot 10^4$ K. At these temperatures, the hydrogen will emit a red color, which gives the name to the solar chromosphere. On the solar chromosphere, phenomena such as changes in polar solar flares, prominences and eruption of filaments and post-flares loop material flow have already been observed. In the chromosphere it is also possible to observe the chromospheric networks, which is caused by the magnetic field beams in the supergranules (NARAYANAN, 2013).

In the chromosphere, an anti-intuitive behavior can also be observed: the increase in temperature with height. And that suggests the existence of an alternative heating source. The researchers believe that this heating source deals with magnetohydrodynamics (MHD) wave motions. Such waves are created when a magnetic field line is shifted, and the field line will begin to oscillate when it returns to its original shape. The oscillations create waves that release energy as they move through the plasma, and this behavior would cause the temperature to rise (NARAYANAN, 2013).

The *transition region* is the region between the solar chromosphere and the solar corona. In this region the temperature increases from approximately 10^4 K to approximately 1 MK and the solar wind is accelerated, reaching hundreds of Mm in height. This region is very narrow and separates the diluted coronal plasma (with numerical densities of $n \lesssim 10^{12}$ m^{-3}) to the dense chromosphere ($n \gtrsim 10^{16}$ m^{-3}) (WIEGELMANN et al., 2014).

2.2.3 Solar Corona

The *solar corona* is the outermost layer of the solar atmosphere. The corona can be seen during a total solar eclipse. The solar corona is composed of plasma and the corona is located above the solar chromosphere and and the transition region, and extends for kilometers in space, such expansion occurs continuously in interplanetary space and in this form is called *solar wind*. The solar corona is a very interesting layer, because there you can observe a behavior that is one of the greatest mysteries of Solar Physics, it is the so-called *coronal heating mechanism* or *coronal heating problem*.

To give you an idea, the temperature of the corona is greater than $1.00027315 \cdot 10^6$ K, while the visible surface (solar photosphere) temperature is about $6.27315 \cdot 10^3$ K (NARAYANAN, 2013). We'll talk more about the coronal heating mechanism in the subsubsection 2.2.3.1.

In the solar corona, at sufficiently high temperatures, collisions of atoms with enough energy to remove electrons from the atomic layers occur, such a process fits the definition of *ionization*. To give you an idea, at very high temperatures, atoms such as iron (F_e) can have from 9 to 13 ejected electrons (temperatures of $\approx 1.3\ 10^6$ K eject nine atoms and temperatures of $\approx 2.3 \cdot 10^6$ K eject 13 electrons). Like the solar chromosphere, the solar corona can only be seen with the naked eye during a solar eclipse, as this is the only time the photosphere's light is blocked so they can be seen (NARAYANAN, 2013).

The solar corona is almost entirely trapped near the Sun by loops of magnetic field lines, so-called *coronal loops*. Some magnetic field lines are not facing the Sun and will appear dark in X-rays. Such places are called *coronal holes*. It is possible to observe *serpentines* in the solar corona that usually emerge from sunspots/active regions. These streamers trap material above the Sun's surface and bind that material to sunspots. Furthermore, above the coronal holes, it is possible to observe dark regions in the corona. Such regions are often found at the solar poles and are associated with open magnetic field lines. (NARAYANAN, 2013).

Most solar winds are generated in these regions. Coronal holes can be seen through X-ray telescopes, as X-rays make it possible to see high temperatures (NARAYANAN, 2013).

Another phenomenon observed in the corona are *coronal mass ejection (CME)* which is a significant release of plasma and magnetic field that accompanies the Sun's corona to the solar wind. CMEs are formed as follows: Flux ropes are a probable initial magnetic configuration of a CME (the emergent flux model (Shibata and Chen (2000) considers the situation where a small-scale emergent flux, which appears at the foot of magnetic arcades, traps a helical twisted magnetic flux tube, i.e. flux ropes (HARRA, 2018)) filling the entire volume of a dark coronal cavity that is seen so often in coronagraph data. When and where flux ropes are formed has been a subject of debate for many years. According to Harra (2018), there are two possibilities:

- Flux rope is formed during eruption: this can happen if there is a shear arch, which can lead to formation of a flow cord through the reconnection

process during eruption;

- Flux rope is formed before eruption: this can happen through reconnection in the lower atmosphere, creating a flux rope that may contain filament material.

The CMEs produce disturbances in the solar winds. Generally, the speeds observed for CME are $\approx$ 500 km.s^{-1}, but speeds of the order of 2000 km.s^{-1} have been observed or more. CMEs originate in closed-field regions in the corona, and field lines within CMEs will be less initially connected to the Sun at both ends (NARAYANAN, 2013).

2.2.3.1 Coronal heating problem and Hinode Mission

Many theories have been proposed to explain the coronal heating problem, which is a problem that has been open for a long time. One can cite, for example, the model that proposes that heating occurs by an acoustic shock wave, on what knew that sound waves are generated by turbulent convection and propagate upward, forming a shock wave and energy used for heating. However, in the 1970, it was proved observationally and theoretically that the wave energy flux needed for coronal heating could not reach the corona altitude by the shock waves due to their short damping scale. Therefore, this model had to be discarded. It is now widely accepted that coronal heating occurs through the transport of energy by magnetic fields that extends from the photosphere to the corona. Properties of coronal structures observed in X-rays allowed us to establish this concept. Research has shown the following correspondence: the stronger the magnetic field, the brighter the corona is. However, to generate the corona the existence of a magnetic field and its strength are insufficient, as the photospheric convections that force the (magnetic) field lines to move are also necessary because a bright corona is not observed above a sunspot known (a region of strong magnetic field), where the convective movement of the photosphere is contained by the presence of magnetic fields (HARA, 2018).

Over time, several space missions have studied the solar corona, and it has been discovered that:

1. The corona is magnetically heated;

2. Coronal holes is where the high-speed solar wind originates;

3. The corona is mainly covered by loop-shaped structures, which we call *coronal loops*, which connect the positive and negative magnetic polarities in the photosphere.

In particular, these results are due to the Orbiting Solar Observatory (OSO) missions and the Skylab station, both from The United States. We can also cite the Parker heating mechanism model ("nanoflares") which is explained below (for more information, see Parker (1972) and Parker (1988)). As the coronal loop resembles the structure of the coronal magnetic field which is calculated from the surface magnetic fields, we have that,

I. The dissipation of the electric currents DC generated in the magnetic structure and...

II. The dissipation of Alfvén waves that propagate along the magnetic field

are strong candidates for the mechanism. These are generated when the magnetic field lines extending towards the corona are translated, twisted or twisted by convective surface movements and due to the difference in the time scales of the movement of the magnetic fields there are two different responses: it appears as a current electricity DC or as an alternating current (Alfvén wave). In the DC heating model, continuous excursions driven by convective motions at the base points of the magnetic fluxes that constitute the coronal loops generate several locations where oppositely directional magnetic fields face each other in the corona. Restructuring of the magnetic field configuration by magnetic reconnection occurs at locations of high current density, and the plasmas within the magnetic loops are heated to coronal temperature (HARA, 2018).

Great efforts have been made to detect the flux tube (at the scale of 0.2 arcsec in the photosphere) in terrestrial laboratories since the 1970. However, the existence was inferred from Spectropolarimeter (see 4.2), where multiple spectral absorption lines with different responses to the magnetic field of the solar photosphere were analyzed. Sometimes it is observed in images, a small object, which with good atmospheric viewing conditions, cannot be found in the magnetogram as an isolated magnetic element due to the optical turbulence of the Earth's atmosphere. This is where the Hinode Mission (see 3) comes in, where the following topics were wanted to understand the formation of the solar corona:

a) Clarify the property of fine-scale magnetic fields and their movement in the photosphere;

b) To explore the variability and velocity structures of thin coronal features in response to the motion of magnetic field structures.

According to Hara (2018), in terms of coronal heating, Hinode was proposed such that the following three points were tackled for the deep understanding:

1. Are Alfvén waves or *DC* electric currents sufficiently generated to heat the corona on the photosphere?
2. Do the waves transfer through the chromosphere toward the corona?
3. Where and how is the energy that is transferred from the lower atmosphere dissipated in the corona?

In the Hinode program, these question were going to be answered by the high-resolution observations of the photospheric vector magnetic field and velocity field for the first 1., by imaging observations of the chromosphere for the second 2., and by the imaging and spectroscopic observations of the corona for the third 3.

3 SPECTROPOLARIMETRY AND POLARIZED LIGHT

The following are theoretical tools that are used to measure physical parameters of the Sun using light. The main tool is spectropolarimetry, which analyzes light as a function of wavelength (spectroscopy) and polarization state (polarimetry), which are the two most important characteristics of light (INIESTA, 2003).

3.1 Description of polarized light by Stokes parameters

First, suppose a region free of currents ($\mathbf{J} = 0$) and charges ($\rho = 0$) and in an isotropic medium (that is, the behavior of the medium under the influence of the electromagnetic field is characterized by equations material with coefficients ϵ (dielectric permittivity), μ (magnetic permeability) and σ (conductivity), which are independent of the direction of propagation of the field) and homogeneous (isotropic medium such that $\nabla\, ln(\epsilon) = 0 = \nabla \ln(\mu)$), and by Maxwell's Equations,

$$\nabla^2\mathbf{E} - \frac{1}{v^2}\frac{\partial^2\mathbf{E}}{\partial t^2} = 0, \tag{3.1}$$

$$\nabla^2\mathbf{H} - \frac{1}{v^2}\frac{\partial^2\mathbf{H}}{\partial t^2} = 0, \tag{3.2}$$

$$v = \frac{c}{\sqrt{\epsilon\mu}} \stackrel{\text{def}}{=} \frac{c}{n}. \tag{3.3}$$

where n is the index of refraction of the medium, v is the wave propagation velocity (of Equation 3.1 and 3.2), $\mathbf{H}$ is the magnetic field, $\mathbf{r}$ is the position vector, and $\mathbf{E}$ is the electric field.

Equations 3.1 and 3.2 have the following simplest solutions,

$$\mathbf{E}(\mathbf{r}, \hat{\mathbf{s}}, t) = \mathbf{E}(\mathbf{r}\cdot\hat{\mathbf{s}} - vt), \tag{3.4}$$

$$\mathbf{H}(\mathbf{r}, \hat{\mathbf{s}}, t) = \mathbf{H}(\mathbf{r}\cdot\hat{\mathbf{s}} - vt), \tag{3.5}$$

$$\mathbf{u} \stackrel{\text{def}}{=} u\hat{\mathbf{s}}, \tag{3.6}$$

$$u \stackrel{\text{def}}{=} \mathbf{r}\cdot\hat{\mathbf{s}} - vt = v\left(\frac{\mathbf{r}\cdot\hat{\mathbf{s}}}{v} - t\right) \stackrel{\text{def}}{=} v\left(\frac{\mathbf{k}\cdot\mathbf{r}}{\omega} - t\right) = \frac{1}{k}\left(\mathbf{k}\cdot\mathbf{r} - \omega t\right), \tag{3.7}$$

where $\hat{\mathbf{s}}$ is the propagation direction vector, $\omega \stackrel{\text{def}}{=} 2\pi\nu$ is the angular frequency, and

$\mathbf{k} \stackrel{\text{def}}{=} k\hat{\mathbf{s}} \stackrel{\text{def}}{=} \left(\frac{2\pi}{\lambda}\right)\hat{\mathbf{s}}$ is the wave vector.

Notice that,

$$\frac{\partial \mathbf{E}}{\partial t} = -v\frac{d\mathbf{E}}{du}, \tag{3.8}$$

$$(\nabla \times \mathbf{E})_x = \frac{\partial E_z}{\partial y} - \frac{\partial E_y}{\partial z} = \frac{dE_z}{dt}s_y - \frac{dE_y}{dt}s_y = \left(\hat{\mathbf{s}} \times \frac{d\mathbf{E}}{dt}\right)_x. \tag{3.9}$$

And replacing 3.8 and 3.9 in the equations:

$$\mathbf{D} = \epsilon\mathbf{E}, \tag{3.10}$$

$$\nabla \times \mathbf{E} + \frac{1}{c}\frac{\partial \mathbf{B}}{\partial t} = 0, \tag{3.11}$$

$$\mathbf{B} = \mu\mathbf{H}, \tag{3.12}$$

$$\nabla \times \mathbf{H} - \frac{1}{c}\frac{\partial \mathbf{D}}{\partial t} = 0. \tag{3.13}$$

And so, it follows that

$$\hat{\mathbf{s}} \times \frac{d\mathbf{H}}{dt} + \frac{\epsilon\mu}{c}\frac{d\mathbf{E}}{du} = 0, \tag{3.14}$$

$$\hat{\mathbf{s}} \times \frac{d\mathbf{E}}{du} - \frac{\epsilon\mu}{c}\frac{d\mathbf{H}}{du} = 0, \tag{3.15}$$

and neglecting the constant of integration,

$$\mathbf{E} = -\sqrt{\frac{\mu}{\epsilon}}\hat{\mathbf{s}} \times \mathbf{H} = -\frac{\mu}{n}\hat{\mathbf{s}} \times \mathbf{H}, \tag{3.16}$$

$$\mathbf{H} = \sqrt{\frac{\epsilon}{\mu}}\hat{\mathbf{s}} \times \mathbf{E} = \frac{\epsilon}{n}\hat{\mathbf{s}} \times \mathbf{E}. \tag{3.17}$$

It is possible to observe that if $\mathbf{E}$ is known, then $\mathbf{H}$ is also known and vice versa. Therefore, Equation 3.2 (as well as its solution given by Equation 3.17) can be

neglected and the analysis can be done only by working with Equation 3.1 (whose solution is given by Equation 3.16). Furthermore, the set $\{\mathbf{E}, \mathbf{H}, \hat{\mathbf{s}}\}$ is an orthonormal set.

Given $j \in \{x, y\}$, the coordinate j of the solution of Equation 3.1, is given by:

$$E_j(t) = a_j \exp[i(ku + \delta_j)]. \tag{3.18}$$

Where, in Equation 3.18, a_j is the real amplitude, δ_j is the phase constant and k is the wave number. Note that the set of the equation 3.18 is given for $E_j^*(t) = a_j \exp[-i(ku + \delta_j)]$. So that physical interpretations can be obtained, it is necessary to manipulate the Equation 3.18 so that a complex amplitude appears, see below

$$u = \mathbf{r} \cdot \hat{\mathbf{s}} - vt \stackrel{\text{def}}{=} \frac{1}{k}(\mathbf{k} \cdot \mathbf{r} - \omega t), \tag{3.19}$$

$$\mathbf{k} \stackrel{\text{def}}{=} k\hat{\mathbf{k}} \stackrel{\text{def}}{=} \left(\frac{2\pi}{\lambda}\right)\hat{\mathbf{s}}, \tag{3.20}$$

$$\omega \stackrel{\text{def}}{=} 2\pi\nu. \tag{3.21}$$

Where λ is the wavelength. And so, the *complex amplitude* A_j will be given by

$$A_j = a_j \exp(-i\mathbf{k} \cdot \mathbf{r})). \tag{3.22}$$

And therefore, assuming that light propagates along the z axis, Equation 3.18 is rewritten as follows

$$E_j(t) = A_j \exp[-i(\omega t - \delta_j)], \ j \in \{x, y\}. \tag{3.23}$$

Given the theoretical introduction, the *polarization tensor* (it is common for the polarization tensor to also appear with the name of *coherence matrix*), can be defined:

$$C \stackrel{\text{def}}{=} \begin{pmatrix} E_x E_x^* & E_x E_y^* \\ E_y E_x^* & E_y E_y^* \end{pmatrix} = \begin{pmatrix} a_x^2 & a_x a_y \exp(i\delta) \\ a_x a_y \exp(-i\delta) & a_y^2 \end{pmatrix}, \tag{3.24}$$

$$\delta \stackrel{\text{def}}{=} \delta_x - \delta_y, \tag{3.25}$$

and by means of the polarization tensor 3.24, the Stokes parameters can be defined.

An important observation that must be made for the above procedure is that it is the simplest case, that is, the monochromatic plane wave however, it is a procedure that can be reproduced so that, in an analogous way, the Stokes parameters can be obtained for more general cases. Because, as will be seen below, the Stokes parameters can be defined through the Polarization Tensor.

For a complete and consistent description of polarized radiation, in particular the partial one, we have the four parameters of Stokes, which is a system widely used in optics (applied to astrophysics) and stellar/solar astronomy. Such a system was consolidated as a standard due to the advantage of being measurable by devices, since the four parameters are real and have the same physical dimensions. As mentioned before, the formalization adopted to obtain the definition of Stokes' parameters will be their derivation through the Polarization Tensor.

First, writing the Polarization Tensor as follows:

$$C \stackrel{\text{def}}{=} \begin{pmatrix} C_{11} & C_{12} \\ C_{21} & C_{22} \end{pmatrix}. \tag{3.26}$$

Once this is done, the following relations are said *Stokes parameters*:

$$I \stackrel{\text{def}}{=} \kappa(C_{11} + C_{22}), \tag{3.27}$$

$$Q \stackrel{\text{def}}{=} \kappa(C_{11} - C_{22}), \tag{3.28}$$

$$U \stackrel{\text{def}}{=} \kappa(C_{12} + C_{21}), \tag{3.29}$$

$$V \stackrel{\text{def}}{=} i\kappa(C_{21} - C_{12}). \tag{3.30}$$

And above, Equations 3.27, 3.28, 3.29 and 3.30 are the most general form, as the

Stokes parameters can always be obtained using the definition given above. Note that the Polarization Tensor can be rewritten as follows:

$$C = \frac{1}{2\kappa}\begin{pmatrix} I+Q & U+iV \\ U-iV & I-Q \end{pmatrix}. \tag{3.31}$$

Now applying what has been described above, suppose that the electric field vector of a quasi-monochromatic light beam is propagating along the z axis. Therefore, given $j \in \{x, y\}$, we have that the solution is given by Iniesta (2003)

$$E_j(t) = [\mathcal{E}_j(t)\exp(i\phi_j(t))]\exp(-2\pi i\nu_0 t) = \mathcal{E}_j(t)\exp[i(\phi_j(t) - 2\pi\nu_0 t)] \tag{3.32}$$

It is easy to see that for given $j \in \{x, y\}$,

$$\mathcal{E}_j(t) = \sqrt{E_j(t)E_j^*(t)} \tag{3.33}$$

$$\phi_j(t) = 2\pi\nu_0 t + \tan^{-1}\left(\frac{\operatorname{Im} E_j(t)}{\operatorname{Re} E_j(t)}\right). \tag{3.34}$$

And its polarization tensor:

$$C = \begin{pmatrix} \langle E_x(t)E_x^*(t)\rangle & \langle E_x(t)E_y^*(t)\rangle \\ \langle E_y(t)E_x^*(t)\rangle & \langle E_y(t)E_y^*(t))\rangle \end{pmatrix} = \begin{pmatrix} \langle \mathcal{E}_x^2(t)\rangle & \langle \mathcal{E}_x(t)\mathcal{E}_y(t)\exp(i\phi(t))\rangle \\ \langle \mathcal{E}_x(t)\mathcal{E}_y(t)\exp(-i\phi(t))\rangle & \langle \mathcal{E}_y^2(t)\rangle \end{pmatrix}, \tag{3.35}$$

$$\phi \stackrel{\text{def}}{=} \phi_x(t) - \phi_y(t). \tag{3.36}$$

Where $\langle\rangle$ is the time average.

And by the definition presented of Stokes parameters (Equations 3.27, 3.28, 3.29 and 3.30), in this situation the Stokes parameters are given by

$$I = \kappa(C_{11} + C_{22}) = \kappa(\langle \mathcal{E}_x^2 \rangle + \langle \mathcal{E}_y^2 \rangle), \tag{3.37}$$

$$Q = \kappa(C_{11} - C_{22}) = \kappa(\langle \mathcal{E}_x^2 \rangle - \langle \mathcal{E}_y^2 \rangle), \tag{3.38}$$

$$U = \kappa(C_{12} + C_{21}) = 2\kappa\langle \mathcal{E}_x \mathcal{E}_y \cos(\phi(t)) \rangle, \tag{3.39}$$

$$V = i\kappa(C_{21} - C_{12}) = 2\kappa\langle \mathcal{E}_x \mathcal{E}_y \sin(\phi(t)) \rangle. \tag{3.40}$$

Which describe the polarization state of light. The Stokes parameter I represents the total intensity. The Stokes parameter Q represents the difference between vertical and horizontal polarization. Stokes parameter U represents the difference between polarization at $45°$ and $-45°$ and Stokes parameter V is the difference between clockwise circularly polarized light and light polarized counterclockwise (STEKEL, 2019).

Note that the polarization tensor C can be rewritten as a function of Stokes parameters, and thus,

$$C = \begin{pmatrix} \langle E_x(t)E_x^*(t) \rangle & \langle E_x(t)E_y^*(t) \rangle \\ \langle E_y(t)E_x^*(t) \rangle & \langle E_y(t)E_y^*(t)) \rangle \end{pmatrix} = \frac{1}{2\kappa} \begin{pmatrix} I + Q & U + iV \\ U - iV & I - Q \end{pmatrix}. \tag{3.41}$$

So notice that

$$I = \kappa \operatorname{tr}(C), \tag{3.42}$$

$$\det(C) = C_{11}C_{22} - C_{12}C_{21}, \tag{3.43}$$

how, for $i \neq j$

$$C_{ij} \leq \sqrt{C_{ii}C_{jj}}, \tag{3.44}$$

and therefore,

$$\det(C) = I^2 + Q^2 + U^2 + V^2 \geq 0, \tag{3.45}$$
$$I^2 - Q^2 - U^2 - V^2 \geq 0 \Rightarrow I^2 \geq Q^2 + U^2 + V^2. \tag{3.46}$$

For the following proposition, the following definition will be used:

$$\langle E_i(t)E_j^*(t)\rangle \stackrel{\text{def}}{=} \lim_{\tau_m\to\infty} \int_{-\frac{\tau_m}{2}}^{\frac{\tau_m}{2}} E_{i,\tau_m}(t)E_{j,\tau_m}^*(t)dt,$$
$$E_{i,\tau_m}(t) \stackrel{\text{def}}{=} E_i(t)\Pi_{\tau_m}(t),$$
$$\Pi_{\tau_m}(t) \stackrel{\text{def}}{=} \begin{cases} 1, & t \in [\frac{-\tau_m}{2}, \frac{\tau_m}{2}] \\ 0, & t \in \mathbb{R} - [-\frac{\tau_m}{2}, \frac{\tau_m}{2}] \end{cases}.$$

Prop.(3.1): Be a beam of light.

Suppose for given t, we have $\frac{\mathcal{E}_y(t)}{\mathcal{E}_x(t)}$ and $\phi(t)$ constants. So $I^2 = Q^2 + U^2 + V^2$

Proof. Suppose that for given t, $\frac{\mathcal{E}_y(t)}{E_x(t)}$ and $\phi(t)$ are constants. Let $c_1, c_2 \in \mathbb{R}$ be such that given t, $\frac{\mathcal{E}_y(t)}{\mathcal{E}_x(t)} = c_1$ and $\phi(t) = c_2$. From the Polarization Tensor 3.35 and Equation 3.41,

$$\mathcal{E}_y(t) = c_1\mathcal{E}_x(t) \Rightarrow$$
$$0 \leq \det(C) = I^2 - Q^2 - U^2 - V^2 =$$
$$\langle\mathcal{E}_x^2(t)\rangle\langle\mathcal{E}_y^2(t)\rangle - \langle\mathcal{E}_x(t)\mathcal{E}_y(t)\exp(i\phi(t))\rangle\langle\mathcal{E}_y(t)\mathcal{E}_x(t)\exp(-i\phi(t))\rangle$$
$$= c_1^2(\langle\mathcal{E}_x^2(t)\rangle^2 - \langle\mathcal{E}_x^2(t)\exp(-\phi(t))\rangle\langle\mathcal{E}_x^2(t)\exp(-i\phi(t))\rangle)$$

But since $\phi(t)$ is constant, then $\exp(i\phi(t))$ and $\exp(-i\phi(t))$ are constant and complex conjugates, so they leave the average time $\langle\rangle$ and in addition, $\exp(i\phi(t))\exp(-i\phi(t)) = 1$. And therefore,

$$\det(C) = c_1^2(\langle \mathcal{E}_x^2(t)\rangle - \langle \mathcal{E}_x^2(t)\rangle = c_1(0)) = 0 \Rightarrow$$
$$\det(C) = I^2 - Q^2 - U^2 - V^2 = 0 \Rightarrow$$
$$I^2 = Q^2 + U^2 + V^2$$

as wanted. □

Next, some definitions will be introduced. The light beam is said to be *totally polarized* and *cannot be distinguished from polarized light*, if it satisfies the conditions of the previous proposition. The light beam is said to be *natural* or *completely unpolarized* if $Q = U = V = 0$. is said to be *partially polarized*, if $Q \neq 0$ or $U \neq 0$ or $V \neq 0$

Once you have the four Stokes parameters, the following definitions can be made: Let I, Q, U and V be Stokes parameters. (i) If $I \neq 0$, the vector $\mathbf{p} \stackrel{\text{def}}{=} \left(\frac{Q}{I}, \frac{U}{I}, \frac{V}{I}\right) \in \mathbb{R}^3$ is said to be a *polarization vector*. (ii) $p \stackrel{\text{def}}{=} |\mathbf{p}|$ is said to be the *degree of polarization of the beam*. (iii) The vector $\mathbf{I} \stackrel{\text{def}}{=} (I, Q, U, V) \in \mathbb{R}^4$ is called the *Stokes vector*.

To address polarization, the application of the Stokes vector helps a lot. Assuming that a light beam passes through optical components, the incident Stokes vector $\mathbf{I}_{in}$ will change, so there will be the output Stokes vector $\mathbf{I}_{out}$. This transformation is described by multiplying Müeller's matrix $\mathbf{M}$ and details will be seen below in Section 3.2.

3.2 Mueller matrices

Polarization properties such as diattenuation, retardance, and depolarization can be represented by the *Müeller matrix*, which by definition is the matrix 4×4 that associates the incident Stokes parameters $\mathbf{I}_{in}$ and the output parameters $\mathbf{I}_{out}$. In other words, let $\mathbf{I}_{in} = (I, Q, U, V)^{\mathrm{t}}$ be the incident Stokes vector, $\mathbf{I}_{out} = (I', Q', U', V')$ the output Stokes vector and $\mathbf{M}$ the Müeller matrix

$$\begin{pmatrix} M_{00} & M_{01} & M_{02} & M_{03} \\ M_{10} & M_{11} & M_{12} & M_{13} \\ M_{20} & M_{21} & M_{22} & M_{23} \\ M_{30} & M_{31} & M_{32} & M_{33} \end{pmatrix} \begin{pmatrix} I \\ Q \\ U \\ V \end{pmatrix} = \mathbf{M}\mathbf{I}_{in} = \mathbf{I}_{out} = \begin{pmatrix} I' \\ Q' \\ U' \\ V' \end{pmatrix}, \tag{3.47}$$

where $\mathbf{I}_{out}$ is given by

$$\mathbf{I}_{out} = \begin{pmatrix} I' \\ Q' \\ U' \\ V' \end{pmatrix} = \begin{pmatrix} M_{00}I + M_{01}Q + M_{02}U + M_{03}V \\ M_{10}I + M_{11}Q + M_{12}U + M_{13}V \\ M_{20}I + M_{21}Q + M_{22}U + M_{23}V \\ M_{30}I + M_{31}Q + M_{32}U + M_{33}V \end{pmatrix} \tag{3.48}$$

If there is a need to describe the effect of a series of polarization elements, the description is done by multiplying individual Müeller matrices, given by $\mathbf{M}_q$, where the index q describes the order in which the elements were observed. That is, the first element observed is found on the right side of the matrix sequence, while the matrix $\mathbf{M}_Q$ represents the final element observed and is found further to the left in the matrix product, that is It is,

$$\mathbf{M} = \mathbf{M}_Q\mathbf{M}_{Q-1}...\mathbf{M}_2\mathbf{M}_1 = \prod_{q=1}^{Q} \mathbf{M}_{Q-q+1}. \tag{3.49}$$

An optical element is said to be *non-polarizing optical element*, if such element does not change the polarization state of the incident polarization $\mathbf{I}_{in} = (I, Q, U, V)^{\mathrm{t}}$. In this case, the Müeller matrix for a given sample (*non-polarizing* and *non-absorbing*) is given by

$$\mathbf{I}_d \stackrel{\text{def}}{=} \begin{pmatrix} 1 & 0 & 0 & 1 \\ 0 & 1 & 0 & 1 \\ 0 & 0 & 1 & 1 \\ 0 & 0 & 0 & 1 \end{pmatrix} \tag{3.50}$$

Once the polarization element whose Müeller matrix is $\mathbf{M}$ is rotated around the light beam by an angle θ, the angle of incidence will remain unchanged. Let $\mathbf{R}_M(\theta)$ be the *Müeller rotation matrix*, given by,

$$\mathbf{R}_M(\theta) \stackrel{\text{def}}{=} \begin{pmatrix} 1 & 0 & 0p & 0 \\ 0 & \cos(2\theta) & -\sin(2\theta) & 0 \\ 0 & \sin(2\theta) & \cos(2\theta) & 0 \\ 0 & 0 & 0 & 1 \end{pmatrix}, \tag{3.51}$$

a beam of normal incidence that passes through an element that is rotating around its normal, so the Müeller matrix will be given by,

$$\mathbf{M}(\theta) = \mathbf{R}_M(\theta)\mathbf{M}\mathbf{R}_M(-\theta), \tag{3.52}$$

whose result will be

$$\begin{pmatrix} 1 & 0 & 0 & 0 \\ 0 & \cos(2\theta) & -\sin(2\theta) & 0 \\ 0 & \sin(2\theta) & \cos(2\theta) & 0 \\ 0 & 0 & 0 & 1 \end{pmatrix} \begin{pmatrix} M_{00} & M_{01} & M_{02} & M_{03} \\ M_{10} & M_{11} & M_{12} & M_{13} \\ M_{20} & M_{21} & M_{22} & M_{23} \\ M_{30} & M_{31} & M_{32} & M_{33} \end{pmatrix} \begin{pmatrix} 1 & 0 & 0 & 0 \\ 0 & \cos(2\theta) & \sin(2\theta) & 0 \\ 0 & -\sin(2\theta) & \cos(2\theta) & 0 \\ 0 & 0 & 0 & 1 \end{pmatrix}. \tag{3.53}$$

The base rotational change for vectors is given by the left multiplication of the rotation matrix, and therefore, for Stokes parameters, the relationship to rotation is given by:

$$\mathbf{S}(\theta) \stackrel{\text{def}}{=} \mathbf{R}_M(\theta)\mathbf{I} = \begin{pmatrix} 1 & 0 & 0 & 0 \\ 0 & \cos(2\theta) & -\sin(2\theta) & 0 \\ 0 & \sin(2\theta) & \cos(2\theta) & 0 \\ 0 & 0 & 0 & 1 \end{pmatrix} \begin{pmatrix} I \\ Q \\ U \\ V \end{pmatrix} = \begin{pmatrix} I \\ Q\cos(2\theta) - U\sin(2\theta) \\ Q\sin(2\theta) + U\cos(2\theta) \\ V \end{pmatrix} \tag{3.54}$$

As the parameters Q and U are separated by 45°, then the angle 2θ arises as a consequence. Stokes parameters return to their original state after a rotation of 180°, that is, $\mathrm{R}_M(180°) = \mathbf{I}_d$. θ is set to positive counterclockwise.

Polarization elements that have two polarization states that are transmitted in the incident polarization state (eigenpolarizations), but with different optical path lengths (phases) are called *retarders* (CHIPMAN et al., 2018). For the following considerations, it will be assumed that the two eigenpolarizations are transmitted losslessly and the element has no diattenuation.

Birefringent retarders are optical elements that divide incident light into two modes with orthogonal polarization states and distinct refractive indices. As propagation delays one mode relative to another, the consequence is two optical path lengths in

addition to *retardance*, ie the optical path difference.

To specify a retarder, you need the optical path difference between the eigenpolarizations, i.e. the retardance δ, in addition to the eigenpolarization states, i.e. the *fast axis* which is the state with the shortest length light path, and the *slow axis*, which is the eigenpolarization state with the longest light path length.

The retarders are given by matrices of the form:

$$\mathbf{M}_{Retarder} = \begin{pmatrix} 1 & \mathbf{0}^{\mathrm{t}} \\ \mathbf{0} & \mathbf{R}_{3\times 3} \end{pmatrix}. \tag{3.55}$$

Where $\mathbf{0} = (0,0,0)^{\mathrm{t}}$ and $\mathbf{R}_{3\times 3}$ is a rotation matrix 3×3.

Note that $\mathbf{M}_{Ratarder} \in O(4,\mathbb{C}) \stackrel{\mathrm{def}}{=} \{\mathbf{A} \in \mathbb{C}^{4\times 4} | (\mathbf{A}^{\mathrm{t}})^* \mathbf{A} = \mathbf{I}_d\}$. In particular, $\mathbf{M}_{Retarder}$ $\in O(4,\mathbb{R}) \stackrel{\mathrm{def}}{=} \{\mathbf{A} \in \mathbb{R}^{4\times 4} | (\mathbf{A}^{\mathrm{t}})\mathbf{A} = \mathbf{I}_d\}$

The matrices $\mathbf{M} \in O(4,\mathbb{R})$ are said to be *pure retarder*. The lower right 3×3 elements form a rotation matrix and thus the retarders mathematically rotate the *Poincaré sphere*, which is defined as follows: $\mathbb{P} \stackrel{\mathrm{def}}{=} \{\mathbf{p} \stackrel{\mathrm{def}}{=} (\frac{Q}{I}, \frac{U}{I}, \frac{V}{I}) \in \mathbb{R}^3 | \frac{\sqrt{Q^2+U^2+V^2}}{I} \leq 1\}$. The *retardance* is given by

$$\delta \stackrel{\mathrm{def}}{=} \arccos\left(\frac{M_{00}+M_{11}+M_{22}+M_{33}}{2} - 1\right) = \arccos\left(\frac{\mathrm{tr}(\mathbf{M})}{2} - 1\right) \tag{3.56}$$

A horizontal linear delay with delay, δ, has the following Mueller matrix,

$$\mathbf{LD}(\delta,0) \stackrel{\mathrm{def}}{=} \begin{pmatrix} 1 & 0 & 0 & 0 \\ 0 & 1 & 0 & 0 \\ 0 & 0 & \cos(\delta) & \sin(\delta) \\ 0 & 0 & -\sin(\delta) & \cos(\delta) \end{pmatrix} \tag{3.57}$$

When the matrix $\mathbf{LR}(\delta,0)$ operates on a Stokes vector, the parameters I and Q will remain unchanged. This is because I and Q are non-zero elements in both eigenpolarizations, horizontally and vertically polarized light. A linear retarder, with its fast axis oriented at an angle θ, can be obtained using the rotation operation, and has a Müeller matrix given by (CHIPMAN et al., 2018)

$$\mathbf{LD}(\delta,\theta) \stackrel{\text{def}}{=} \begin{pmatrix} 1 & 0 & 0 & 0 \\ 0 & \cos^2(2\theta)+\cos(\delta)\sin^2(2\theta) & (1-\cos(\delta))\cos(2\theta)\sin(2\theta) & -\sin(\delta)\cos(2\theta) \\ 0 & (1-\cos(\delta))\cos(2\theta)\sin(2\theta) & \cos(\delta)\cos^2(2\theta)+\sin^2(2\theta) & \cos(2\theta)\sin(\delta) \\ 0 & \sin(\delta)\sin(2\theta) & -\cos(2\theta)\sin(\delta) & \cos(\delta) \end{pmatrix} \tag{3.58}$$

Equation 3.58, also known as general linear retarder, is used to do the plate calculations.

3.3 Spectral line $Fe\ I$

The solar abundance of iron (Fe) is of fundamental importance in the studies of Astronomy/Solar Astrophysics, as iron is a standard reference element for the metallicity of stars and galaxies (NORDLUND et al., 2009). The $Fe\ I$ spectral line was chosen because the Hinode Mission Spectropolarimeter operates a fixed band of wavelengths, all centered on the spectral lines $Fe\ I$ (LITES et al., 2013) (this topic will be discussed in more detail depth in 4.2). It is worth mentioning that the spectral line $Fe\ I$ (in the wavelengths 630.15 nm and 630.25 nm) is used to make the radioactive diagnoses that will be presented in the results (see 6).

The importance of observing spectral lines is to try to infer the magnetic field. In particular, in the iron atom, 5000 multiplets can be observed in addition to approximately 300 identified terms, and as a consequence there are a large number of visible, infrared and ultraviolet spectral lines associated with the iron element (SHELYAG, 2004).

Another noteworthy property observed in the visible lines of $Fe\ I$ at the wavelengths 630.15 nm and 630.25 nm is the advantage of the lines being less sensitive to temperature (SHELYAG, 2004).

Works such as Suárez et al. (2010) explored the pair of spectral lines $Fe\ I$, where through the synthesis of realistic Stokes profiles for the lines $Fe\ I$ in 630.15 nm and 630.25 nm, simulations were used with an MHD code for compressible plasmas. The Stokes spectra of the two lines of the MHD models were generated using the SIR code (COBO; INIESTA, 1992). After following the previous process, the iron lines were inverted separately with the MILOS Inversion Code (SUÁREZ; INIESTA, 2007).

In the Suárez et al. (2010) research, it was also observed that discrepancies between

thermodynamic parameters do not affect the magnetic field and velocity inferences, since the results of the inversions of the lines are very similar.

3.4 Zeeman effect

The Zeeman effect can be summarized as follows: in the presence of a relatively strong magnetic field, spectral lines of some elements split into several components whose characteristics depend on polarization and intensity.

In 1896, physicist Pieter Zeeman performed an experiment as follows:

1. When the radiation from a lamp discharge was immersed in a magnetic field, the spectral line was separated into several components. In the simplest case (Classic, see 3.4.1) the spectral line breaks down into three components.

   Let ν_0 be the frequency of the undisturbed line, and ν_L be the *Lamor frequency*, the three components are located at the frequencies $\nu_0 - \nu_L$, ν_0 and $\nu_0 + \nu_L$. The Lamor frequency is defined as follows:

$$\nu_L \stackrel{\text{def}}{=} \frac{e_0 B}{4\pi m c} \ [\mathrm{s}^{-1}] \tag{3.59}$$

2. Parallel to the magnetic field, the central component was not seen, while circularly polarized components were observed, where one component was polarized to the right and the other to the left. This is the so-called *longitudinal Zeeman effect* and can be seen in Figure 3.2.

3. In a direction perpendicular to the magnetic field, three linearly polarized components were observed. The central component π is seen polarized parallel to the magnetic field, and the components σ are polarized perpendicular to the magnetic field. This is the so-called *transversal Zeeman effect* and can be seen in Figure 3.1.

In Figure 3.3 we have a more general representation of the Zeeman effect. In 1897, these results were published by Zeeman (1897).

Figure 3.1 - Transversal Zeeman effect. When the magnetic field is perpendicular to the line-of-sight (LOS). The observer can visualize the π component, the σ_b component and the σ_r component and they are all linearly polarized.

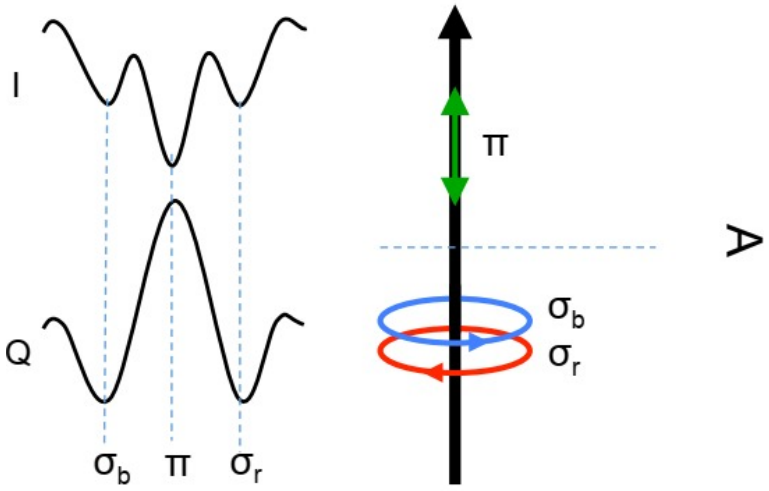

SOURCE: Stekel (2019).

Figure 3.2 - Longitudinal Zeeman effect. In this case, the LOS is parallel to the magnetic field and the observer can visualize only the σ_r and σ_b components, both circularly polarized and in opposite directions.

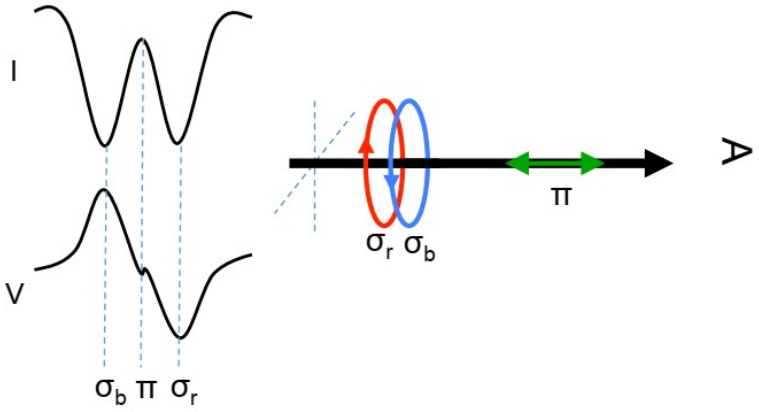

SOURCE: Stekel (2019).

Figure 3.3 - Here there is a more general view, where the polarization of the different Zeeman components is shown (which depend on the type of component and the angle between the observation direction and the magnetic field vector).

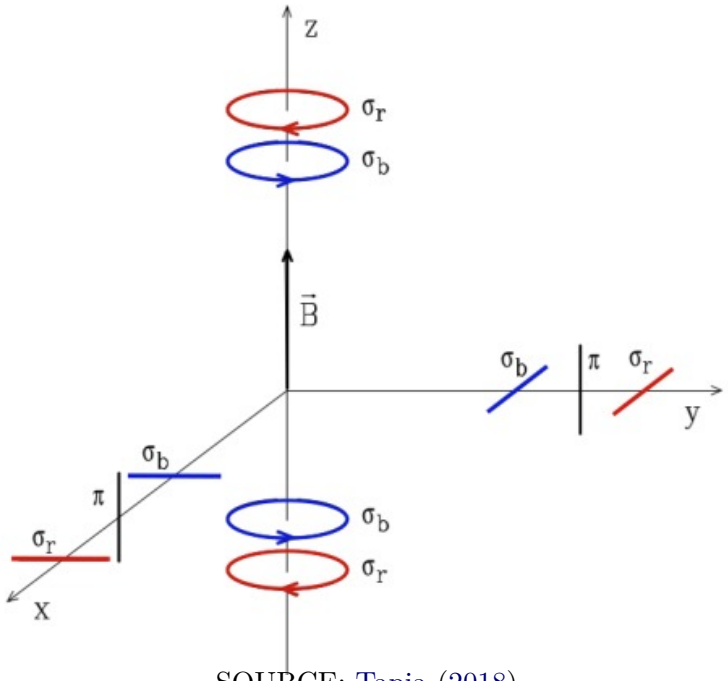

SOURCE: Tapia (2018).

3.4.1 Classical case

At that time, Quantum mechanics did not yet exist, so Zeeman and Lorentz resorted to the theory of Classical Mechanics. According to the formalism of classical mechanics, atoms are assumed to be classical oscillators that move under the action of a restoring force, and that have a charge. Let $\mathbf{x}$ be the position of the charge, in the presence of a magnetic field $\mathbf{B}$, with charge e_0, mass m the position of the electron is described by the following equation:

$$\frac{d^2\mathbf{x}}{dt^2} = -4\pi^2\nu_0^2\mathbf{x} - \frac{e_0}{mc}\frac{d\mathbf{x}}{dt} \times \mathbf{B} - \gamma\frac{d\mathbf{x}}{dt} \tag{3.60}$$

where γ is the damping constant of the particle whose charge e_0. In a situation without damping, the equation (in a presence of a magnetic field $\mathbf{B}$) takes the following form:

$$\frac{d^2\mathbf{x}}{dt^2} = -4\pi^2\nu_0\mathbf{x} - \frac{e_0}{mc}\frac{d\mathbf{x}}{dt} \times \mathbf{B} \tag{3.61}$$

Let $\hat{\mathbf{u}}_0 \in \mathbb{R}^3$ be a unit vector parallel to the vector $\mathbf{B}$, and $\hat{\mathbf{u}}_r$ and $\hat{\mathbf{u}}_s \in \mathbb{R}^3$ two unit vectors that belong to a plane perpendicular to $\mathbf{B}$ such that $\{\hat{\mathbf{u}}_r, \hat{\mathbf{u}}_s, \hat{\mathbf{u}}_0\}$ form a basis for $\mathbb{R}^3$. After that, from $\hat{\mathbf{u}}_r$ and $\hat{\mathbf{u}}_s$, it is possible to define the unit vectors $\hat{\mathbf{u}}_{+1}$ and $\hat{\mathbf{u}}_{-1}$ as follows:

$$\hat{\mathbf{u}}_{+1} \stackrel{\text{def}}{=} \frac{1}{\sqrt{2}}(-\hat{\mathbf{u}}_r + i\hat{\mathbf{u}}_s) \tag{3.62}$$

$$\hat{\mathbf{u}}_{-1} \stackrel{\text{def}}{=} \frac{1}{\sqrt{2}}(\hat{\mathbf{u}}_r + i\hat{\mathbf{u}}_s) \tag{3.63}$$

Assume the following equality holds:

$$\mathbf{x} = \sum_{\alpha} x_\alpha \hat{\mathbf{u}}_\alpha, \alpha \in \{-1, 0, +1\}$$

it is possible to verify that

$$\hat{\mathbf{u}}_\alpha \times \hat{\mathbf{u}}_0 = -i\alpha\hat{\mathbf{u}}_\alpha, \alpha \in \{-1, 0, +1\} \tag{3.64}$$

Therefore, for given $\alpha \in \{-1, 0, +1\}$, the following equation can be obtained (considering the case with γ damping, the case of Equation 3.61 is a particular case):

$$\frac{d^2x_\alpha}{dt^2} = -4\pi^2\nu_0^2 x_\alpha + 4\pi i\alpha\nu_L \frac{dx_\alpha}{dt} - \gamma\frac{dx_\alpha}{dt} \ . \tag{3.65}$$

Suppose the solution to the Equation 3.65 has the following form:

$$x_\alpha(t) = A_\alpha \exp(-2\pi i\nu_\alpha t), \alpha \in \{-1, 0, +1\}. \tag{3.66}$$

Generally ν_L, $\gamma \ll \nu_0$ and therefore for $\alpha \in 1, 0, +1$, in terms of ν_L and γ, the solution has the following form:

$$x_\alpha(t) = A_\alpha \exp(-2\pi i(\nu_0 - \alpha\nu_L)t) \exp\left(-\frac{\gamma}{2}t\right), \tag{3.67}$$

where A_α is a constant determined by initial conditions (DEGL'IINNOCENTI; LANDOLFI, 2004).

In the case where damping is not involved, the Equation 3.65 reduces to the following equation

$$\frac{d^2x_\alpha}{dt^2} = -4\pi^2\nu_0^2 x_\alpha + 4\pi i\alpha\nu_L \frac{dx_\alpha}{dt} \ . \tag{3.68}$$

And since the solution is given by Equation 3.66, it is possible to imply that

$$\nu_\alpha^2 + 2\alpha\nu_L - \nu_0 = 0, \tag{3.69}$$

and therefore

$$\nu_\alpha = -\alpha\nu_L + \sqrt{\alpha^2\nu_L + \nu_0} \ \alpha \in \{-1, 0, 1\}. \tag{3.70}$$

According to Degl'Innocenti (2014), the magnetic field in the laboratory conditions is such that $B < 10^5$ G and thus $\nu_0 \gg \nu_L$, and therefore

$$\nu_\alpha = \nu_0 - \alpha\nu_L. \tag{3.71}$$

That is, there are three distinct oscillators with frequencies $\nu_0 - \nu_L$, ν_0 and $\nu_0 + \nu_L$. As Zeeman observed (DEGL'INNOCENTI, 2014).

3.4.2 Anomalous (or Quantum) case

To explain the anomalous case, it is necessary to introduce new definitions and tools from Quantum Mechanics. In addition, the behavior observed in the classic case of the Zeeman effect 3.4.1, can be explained by these new tools from Quantum Mechanics, as it's be seen next.

Initially, suppose an atom with n electrons where the ith electron has an orbital angular momentum $\mathbf{l}_i$ and a spin angular momentum $\mathbf{s}_i$. In such a system three interactions stand out, they are:

a) the Coulomb repulsion;

b) the spin-spin interaction between individual electrons;

c) and the spin-orbit interaction.

Assuming that the Coulomb interaction is the most important, the total orbital momentum, the total spin angular momentum and the total angular momentum are defined respectively by:

$$\mathbf{L} \stackrel{\text{def}}{=} \sum_{i=1}^{n} \mathbf{l}_i \tag{3.72}$$

$$\mathbf{S} \stackrel{\text{def}}{=} \sum_{i=1}^{n} \mathbf{s}_i \tag{3.73}$$

$$\mathbf{J} \stackrel{\text{def}}{=} \mathbf{L} + \mathbf{S} \tag{3.74}$$

With coupling conditions close to LS (RUSSELL; SAUNDERS, 1925), then the two operators $\mathbf{L}^2$, $\mathbf{S}^2$, $\mathbf{J}^2$ and $\mathbf{J}_z$ form a complete set of commutation operators and associated with these operators, the quantum numbers L, S, J and M will appear, and $|LSJM\rangle$ is the eigenvector of the four operators.

$$\mathbf{L}^2|LSMJ\rangle = \frac{h^2}{4\pi^2}L(L+1)|LSMJ\rangle$$
$$\mathbf{S}^2|LSMJ\rangle = \frac{h^2}{4\pi^2}S(S+1)|LSMJ\rangle$$
$$\mathbf{J}^2|LSMJ\rangle = \frac{h^2}{4\pi^2}M(M+1)|LSMJ\rangle$$
$$\mathbf{J}_z|LSMJ\rangle = \frac{h}{2\pi}|LSMJ\rangle$$

Let the quantum numbers be L, S, and J. L is the orbital angular momentum, S is the spin angular momentum, and J is the total angular momentum. Such numbers are used to describe the state of energy in Quantum Mechanics. And so, there is the motivation to introduce the following notation to represent a Quantum number: ${}^{2S+1}L_J$[1].

Let e be the elementary charge, m_e the mass of the charge $\hbar \stackrel{\text{def}}{=} h/2\pi$, g_L the Landé factor, M the magnetic quantum number, B the magnitude of the magnetic field and E_j the atomic level energy in the absence of the magnetic field, the atomic level energy is given by:

$$E_{J,M} = E_J + \frac{\hbar e}{2m_e c}g_L MB. \tag{3.75}$$

And the Landé factor g_L, is defined as follows:

$$g_L \stackrel{\text{def}}{=} \frac{3}{2} + \frac{S(S+1) - L(L+1)}{2J(J+1)}. \tag{3.76}$$

The magnetic field splits the energy level (L,S,J) into $2J+1$ sublevels of different energies, described by $M \in \{-J, -J+1, ..., J-1, J\}$.

Initially, suppose $J \neq 0$. In such a situation, the magnetic quantum number is defined as follows:

$$\Delta M \stackrel{\text{def}}{=} M_u - M_l \in \{-1, 0, +1\}, \tag{3.77}$$

[1]This form provides information about the quantum numbers L, S and J, where the letters S, P, D, F, ... signify an orbital angular momentum corresponding to $L = 0, 1, 2, 3, ...$ For example ${}^7D_1$ implies that $L = 2$, $S = 3$ and $J = 1$.

where M_u denotes the quantum magnetic number at the upper energy level and M_l denotes the quantum magnetic number at the lower energy level. The transitions $\Delta M = 0$ are said *transitions* π, the transitions where $\Delta M \in \{-1, +1\}$ are said *transitions* σ. And further, if $\Delta M = -1$ $(+1)$ the transition σ is called σ red (blue) and denoted by σ_r (σ_b).

Figure 3.4 - Anomalous Zeeman effect. Note the transition between energy levels for the absence and presence of the magnetic field. At both levels $J = 2$, then the upper and lower energy level split in the presence of a magnetic field.

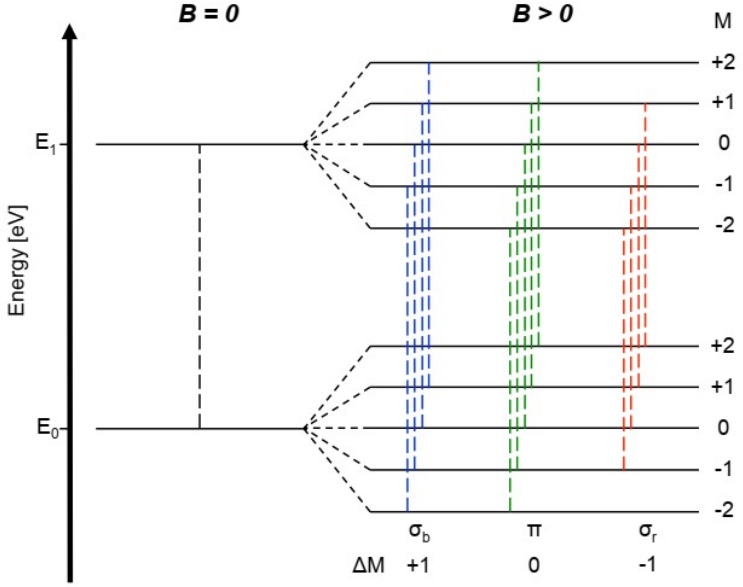

SOURCE: Stekel (2019).

In Figure 3.4, there is a representation of the so-called anomalous Zeeman effect (also called the quantum Zeeman effect). Note it is possible to observe the transition between energy levels in the presence and absence of a magnetic field, also note that $J = 2$ and with different Landé factors.

Line splitting is determined as the wavelength shift of the σ components (λ_σ) to the reference wavelength of the unmagnetized case (λ_0). this is:

$$|\Delta\lambda| = |\lambda_\sigma - \lambda_0| = \frac{eB\lambda_0^2}{4\pi m_e c} g_{eff}. \tag{3.78}$$

Above, in Equation 3.78, g_{eff} is the *effective Landé factor*, which is intended to show the sensitivity of the spectral line in response to the Zeeman effect, and according

to Shenstone and Blair (1929), the g_{eff} is defined by:

$$g_{eff} \stackrel{\text{def}}{=} \frac{1}{2}(g_u + g_l) + \frac{1}{4}(g_u - g_l)[J_u(J_u + 1) - J_l(J_l + 1)] \tag{3.79}$$

In particular, as mentioned before, through the tools of Quantum Mechanics and the definitions used in the anomalous Zeeman effect, the classical Zeeman effect can be explained/formalized, and the behavior of the classical case can be represented (Figure 3.5).

If $J = 0$, and using the definition given by Equation 3.77, because when $J = 0$, lower energy level does not split in the presence of a magnetic field. Therefore, when $J = 1$ implies that $2J+1 = 2.1+1 = 3$, which means that the upper energy level will split into three sub-levels, i.e. the magnetic quantum numbers, will be such that, $M \in \{-1, 0, +1\}$. And therefore, the definition given for the transitions can be applied, i.e. $\Delta M \in \{-1, 0, 1\}$ (and furthermore $\Delta M = 0$, component π and $\Delta M = -1(+1)$, σ_r (σ_b)). In other words, the classic case of the Zeeman effect is obtained.

In Table 3.1, the Zeeman effects are described and in Figure 3.6 the Zeeman effect can be observed in the active region where this work is concentrated, note the separation of spectral lines in the sunspot region.

Table 3.1 - Types of Zeeman effects.

Type	$\mathbf{J_l}$ **and** $\mathbf{J_u}$
Classic	$J_l = 0$ and $J_u = 1$
Anomalous/Quantic	$J_l \neq 0$

SOURCE: Author.

Figure 3.5 - Normal Zeeman effect. Transition between energy levels for the absence and presence of the magnetic field. Due to $J_l = 0$, the lowest energy level does not split in the presence of a magnetic field. When $J_u = 1$, the upper energy level splits into three different sublevels with the magnetic quantum numbers $M \in \{-1, 0, +1\}$. At the bottom, the spectral aspect for both cases.

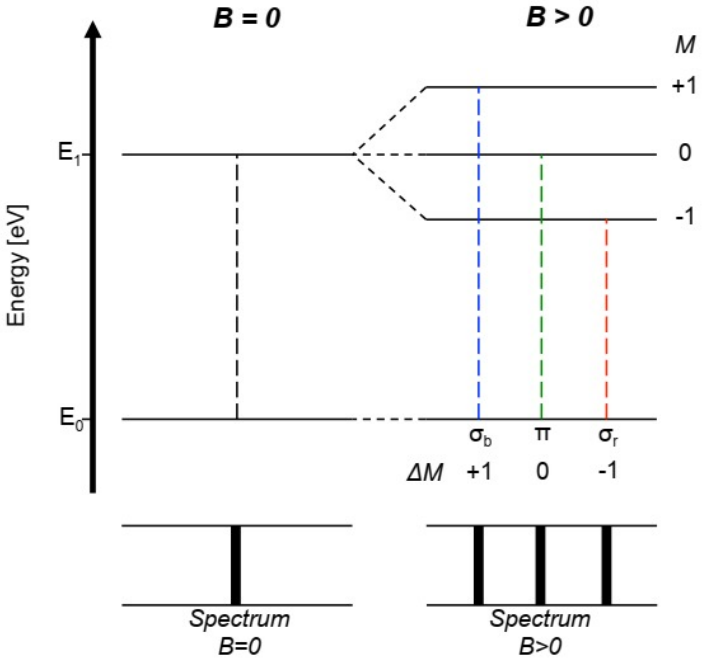

SOURCE: Stekel (2019).

Figure 3.6 - The Zeeman effect and line separation on the Stokes I map in AR11967 (region where this work focuses).

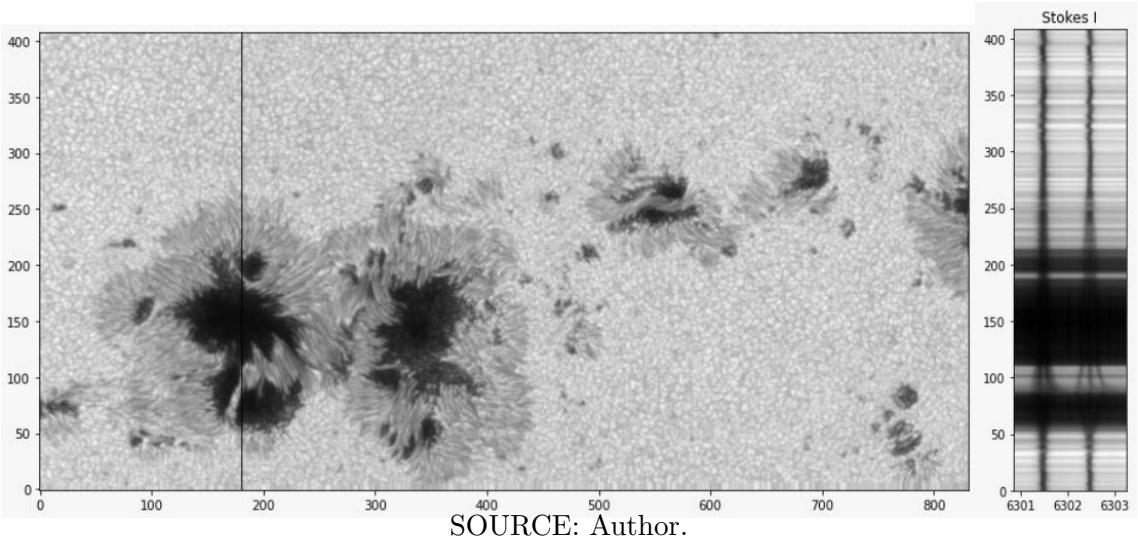

SOURCE: Author.

3.5 Radiative Transfer Equation

3.5.1 Introduction and Local Thermodynamic Equilibrium (LTE)

The *radiative transfer equation* (RTE), is responsible for describing the transfer of a polarized light beam taking into account the changes in its polarization state due to the present magnetic field. Such a description is valid for a magnetized atmosphere, such as the solar photosphere, which is the subject of study in this work.

The variations of the Stokes vector $\mathbf{I} = (I, Q, U, V)^{\mathrm{t}}$ along the ray path (of the light beam), are explained by the following version of the RTE:

$$\frac{d\mathbf{I}}{dz} = -\mathbf{K}\mathbf{I} + \mathbf{j}, \tag{3.80}$$

where $\mathbf{j}$ is the term representing the emissive properties of the medium, and $\mathbf{K}$ is the so-called *propagation matrix*. The term $\mathbf{j}$ is defined as follows:

$$\mathbf{j} \stackrel{\text{def}}{=} \begin{pmatrix} j_I \\ j_Q \\ j_U \\ j_V \end{pmatrix}. \tag{3.81}$$

And the $\mathbf{K}$ propagation matrix is defined as follows:

$$\mathbf{K} \stackrel{\text{def}}{=} \begin{pmatrix} \eta_I & \eta_Q & \eta_U & \eta_V \\ \eta_Q & \eta_I & \rho_V & -\rho_U \\ \eta_U & -\rho_V & \eta_I & \rho_Q \\ \eta_V & \rho_U & -\rho_Q & \eta_I \end{pmatrix}. \tag{3.82}$$

An important observation that should be introduced is that the assumption assumed is that the ray is propagating along the axis Z, and therefore, the derivative on the left side of Equation 3.80 is with respect to z. Furthermore, when the emission term $\mathbf{j}$ is not involved (process without emission), Equation 3.80, reduces to the following form of RTE (INIESTA, 2003):

$$\frac{d\mathbf{I}}{dz} = -\mathbf{K}\mathbf{I}.$$

According to Iniesta (2003), in the propagation matrix $\mathbf{K}$, birefringence (dichroism), absorption and dispersion terms appear. First define the following matrices,

$$\mathbf{K}_1 \stackrel{\text{def}}{=} \begin{pmatrix} \eta_I & 0 & 0 & 0 \\ 0 & \eta_I & 0 & 0 \\ 0 & 0 & \eta_I & 0 \\ 0 & 0 & 0 & \eta_I \end{pmatrix}, \tag{3.83}$$

$$\mathbf{K}_2 \stackrel{\text{def}}{=} \begin{pmatrix} 0 & \eta_Q & \eta_U & \eta_V \\ \eta_Q & 0 & 0 & 0 \\ \eta_U & 0 & 0 & 0 \\ \eta_V & 0 & 0 & 0 \end{pmatrix}, \tag{3.84}$$

$$\mathbf{K}_3 \stackrel{\text{def}}{=} \begin{pmatrix} 0 & 0 & 0 & 0 \\ 0 & 0 & \rho_V & -\rho_U \\ 0 & -\rho_V & 0 & \rho_Q \\ 0 & \rho_U & \rho_Q & 0 \end{pmatrix}, \tag{3.85}$$

and then note that $\mathbf{K} = \mathbf{K}_1 + \mathbf{K}_2 + \mathbf{K}_3$, i.e. $\mathbf{K}$ can be decomposed into three matrices. The matrix of Equation 3.83 is diagonal, symmetric and corresponds to the absorption phenomena. The matrix of Equation 3.84 is symmetric, and corresponds to dichroism, where some polarized components of the light beam are extinguished more than others because the elements of the matrix are generally different. The matrix of Equation 3.85 is antisymmetric and corresponds to dispersion.

The absorption processes themselves include the processes of supplying energy to the thermal reservoir of matter at the expense of electromagnetic energy, as the dispersion will influence the energy balance by deflecting the photons from their original trajectory after collision with material particles. Attention should be drawn to the fact that in these processes the direction of light can change, as well as the frequency of the photons (although, in the kinetic energy, only a small influence will be effected). Note that there are differences in the phenomena. Some observations are dependent on the value that the thermodynamic variables of the material assume locally, such as absorption and dispersion. Other observations, such as scattering, may depend on the radiation field. And therefore, it can be implied that the *general radiative transfer problem* is such that, the sought equation must explain the evolution of the solution vector $\mathbf{I} = (I, Q, U, V)^{\mathrm{t}}$, where the behavior of the materials is known. As the state of matter depends on the characteristics of the radiation

field, it will be necessary to formulate statistical equilibrium equations and, therefore, the simultaneous solution of the radiative transfer equation and the statistical equilibrium equations will be mandatory (INIESTA, 2003).

For this work, it will not be necessary to consider this general radiative transfer problem. The simplest case will be introduced and assumed, such a case is called *local thermodynamic equilibrium* (LTE) approximation.

The LTE hypothesis implies that a single temperature value T is enough to describe the thermodynamic state of a volume with a radius smaller than the thermalization length (FRANZ, 2011). Which in turn implies that the velocity of the particles along the line-of-sight (LOS) follows a Maxwell distribution.

More elaborately, in the LTE hypothesis it is assumed that only radiation can undergo a deviation from a situation of thermodynamic equilibrium because of transport, excluding matter. The local distribution of velocities is Maxwellian, since the thermodynamic equilibrium equations govern the thermodynamic properties of matter, but in the local values of temperature, T and density, ρ. Therefore, the local number of absorbers and emitters in the quantum states is described by the Boltzmann and Saha equations, in addition, Kirchhoff's law is verified:

$$\mathbf{j} = B_\nu(T) \begin{pmatrix} \eta_I \\ \eta_Q \\ \eta_U \\ \eta_V \end{pmatrix}, \tag{3.86}$$

where, according to Solanki (1987), $B_\nu(T)$ is given by

$$B_\nu(T) = S(T) \stackrel{\text{def}}{=} \frac{2hc^2}{\lambda^5} \frac{1}{\frac{\beta_l}{\beta_u} \exp\left(\frac{hc}{\kappa T \lambda}\right) - 1}. \tag{3.87}$$

In other words, assuming the LTE hypothesis and the light beam is full redistribution, the light beam is described by the following RTE:

$$\frac{d\mathbf{I}}{dz} = \frac{d}{dz}\begin{pmatrix} I \\ Q \\ U \\ V \end{pmatrix} = -\begin{pmatrix} \eta_I & \eta_Q & \eta_U & \eta_V \\ \eta_Q & \eta_I & \rho_V & -\rho_U \\ \eta_U & -\rho_V & \eta_I & \rho_Q \\ \eta_V & \rho_U & -\rho_Q & \eta_I \end{pmatrix}\begin{pmatrix} I \\ Q \\ U \\ V \end{pmatrix} + B_{nu}(T)\begin{pmatrix} \eta_I \\ \eta_Q \\ \eta_U \\ \eta_V \end{pmatrix} = -\mathbf{K}\mathbf{I} + \mathbf{j}, \tag{3.88}$$

which matches the Equation 3.80. Defined a *Source Function* $\mathbf{S}$, which is a vector function as follows:

$$\mathbf{S} \stackrel{\text{def}}{=} \begin{pmatrix} B_\nu(T) \\ 0 \\ 0 \\ 0 \end{pmatrix}, \tag{3.89}$$

The Equation 3.88, can be written as follows:

$$\frac{d\mathbf{I}}{dz} = \frac{d}{dz}\begin{pmatrix} I \\ Q \\ U \\ V \end{pmatrix} = -\begin{pmatrix} \eta_I & \eta_Q & \eta_U & \eta_V \\ \eta_Q & \eta_I & \rho_V & -\rho_U \\ \eta_U & -\rho_V & \eta_I & \rho_Q \\ \eta_V & \rho_U & -\rho_Q & \eta_V \end{pmatrix}\begin{pmatrix} I - B_\nu(T) \\ Q \\ U \\ V \end{pmatrix} = -\mathbf{K}(\mathbf{I} - \mathbf{S}) \tag{3.90}$$

3.5.2 Relationship between spectral line formation and RTE

The following theory was motivated by the need to obtain a version of the RTE that can describe the behavior of formation of spectral lines in the anisotropic medium. Let $\mathbf{K}$ be the propagation matrix, according to Iniesta (2003), the matrix $\mathbf{K}$ has a term associated with the continuum-forming process which will be given by $\mathbf{K}_{cont}$, and a term associated with the line-forming process which will be given by $\mathbf{K}_{lin}$. Therefore

$$\mathbf{K} \stackrel{\text{def}}{=} \mathbf{K}_{cont} + \mathbf{K}_{lim} = \chi_{cont}\mathbf{I}_d + \frac{N\pi e_0^2 f}{mc}\mathbf{\Phi}. \tag{3.91}$$

Where the continuum-forming and line-forming matrix are given, respectively, by

$$\mathbf{K}_{cont} \stackrel{\text{def}}{=} \chi_{cont}\mathbf{I}_d, \tag{3.92}$$

$$\mathbf{K}_{lin} \stackrel{\text{def}}{=} \chi_{lin}\mathbf{\Phi}, \tag{3.93}$$

and χ_{lin} is given by

$$\chi_{lin} \stackrel{\text{def}}{=} \frac{N\pi e_0^2 f}{mc}, \tag{3.94}$$

in addiction, χ_{cont} is the continuum absorption coefficient, and $\mathbf{\Phi}$ includes the absorption and dispersion profiles.

With the introduction of the *line-to-continuum absorption coefficient ratio*,

$$\eta_0 \stackrel{\text{def}}{=} \frac{\chi_{lin}}{\chi_{cont}} = \frac{N\pi e_0^2 f}{mc\chi_{cont}}, \tag{3.95}$$

where f is the *oscillator strength*, N is the number volume density of dipoles, e_0 is the charge of the electro and c is thespeed of light in vacuum. The Equation 3.91 can be rewritten as

$$\mathbf{K} = \chi_{cont}(\mathbf{I}_d + \eta_0\mathbf{\Phi}). \tag{3.96}$$

Now, the *continuum optical depth*, can be introduced. It is defined by:

$$\tau_c \stackrel{\text{def}}{=} \int_z^{z_0} \chi_{cont} dz = -\int_{z_0}^{z} \chi_{cont} dz \tag{3.97}$$

Equation 3.99 is the number of mean free paths of continuum photons between z_0 and z. Also, τ_c is dimensionless. Note that,

$$d\tau_c = -\chi_{cont} dz, \tag{3.98}$$

and Equation 3.98, implies that Equation 3.90, can be rewritten as follows:

$$\frac{d\mathbf{I}}{d\tau_c} = \frac{\mathbf{K}}{\chi_{cont}}(\mathbf{I} - \mathbf{S}). \tag{3.99}$$

further, $\frac{\mathbf{K}}{\chi_{cont}}$ is given by

$$\frac{\mathbf{K}}{\chi_{cont}} = \mathbf{I}_d + \eta_0 \mathbf{\Phi}. \tag{3.100}$$

Without loss of generality, the matrix $\mathbf{K}\chi_{cont}$ can simply be called $\mathbf{K}$ and the elements of $\frac{\mathbf{K}}{\chi_{cont}}$ can be seen as in the Equation 3.82. This is,

$$\mathbf{K} = \mathbf{I}_d + \eta_0 \mathbf{\Phi} = \begin{pmatrix} \eta_I & \eta_Q & \eta_U & \eta_V \\ \eta_Q & \eta_I & \rho_V & -\rho_U \\ \eta_U & -\rho_V & \eta_I & \rho_Q \\ \eta_V & \rho_U & -\rho_Q & \eta_I \end{pmatrix}, \tag{3.101}$$

and in this way, the most useful form of the RTE is obtained, which is given by:

$$\frac{d\mathbf{I}}{d\tau_c} = \mathbf{K}(\mathbf{I} - \mathbf{S}), \tag{3.102}$$

which will be very useful for the inversion code and for the Chapter 3.5.3 to follow.

According to Iniesta (2003), the entries of the matrix given by Equation 3.101 are given by

$$\eta_I \stackrel{\text{def}}{=} 1 + \frac{\eta_0}{2}\left(\phi_0 \sin^2(\theta) + \frac{1}{2}(\phi_{+1} + \phi_{-1})(1 + \cos^2(\theta))\right), \tag{3.103}$$

$$\eta_Q \stackrel{\text{def}}{=} \frac{\eta_0}{2}\left(\phi_0 - \frac{1}{2}(\phi_{+1} + \phi_{-1})\right)\sin^2(\theta)\cos(2\varphi), \tag{3.104}$$

$$\eta_U \stackrel{\text{def}}{=} \frac{\eta_0}{2}\left(\phi_0 - \frac{1}{2}(\phi_{+1} + \phi_{-1})\right)\sin^2(\theta)\sin(2\varphi), \tag{3.105}$$

$$\eta_V \stackrel{\text{def}}{=} \frac{\eta_0}{2}(\phi_{-1} - \phi_{+1})\cos(\theta), \tag{3.106}$$

$$\rho_Q \stackrel{\text{def}}{=} \frac{\eta_0}{2}\left(\psi_0 - \frac{1}{2}(\psi_{+1} + \psi_{-1})\right)\sin^2(\theta)\cos(2\varphi), \tag{3.107}$$

$$\rho_U \stackrel{\text{def}}{=} \frac{\eta_0}{2}\left(\psi_0 - \frac{1}{2}(\psi_{+1} - \psi_{-1})\right)\sin^2(\theta)\sin(2\varphi), \tag{3.108}$$

$$\rho_V \stackrel{\text{def}}{=} \frac{\eta_0}{2}(\psi_{-1} - \psi_{+1})\cos(\theta). \tag{3.109}$$

Where, from Equation 3.103 to Equation 3.109, θ is the angle of inclination of the magnetic field and φ is the angle of azimuth.

An important note to make is that the index -1 can be replaced by r which refers to "red" (the right-handed circular component), the index $+1$ can be replaced by b referring to "blue" (left-handed circular component), and the index 0 can be replaced by p referring to "principal" (linearly polarized component).

According to Stekel (2019) and taking into account the (classical) Lorentz theory, the scatter profiles (ψ_{-1}, ψ_0 and ψ_{+1}) and absorption (ϕ_{-1}, ϕ_0 and ϕ_{+1}), are given by the following equations:

$$\phi_j = \sum_{i_j=1}^{N_j} s_{i_j}\mathcal{H}(a, \nu + \nu_D + \upsilon_{i_j}),\ j \in \{-1, 0, +1\}, \tag{3.110}$$

$$\psi_j = 2\sum_{i_j=1}^{N_j} s_{i_j}\mathcal{H}(a, \nu + \nu_D + \upsilon_{i_j}),\ j \in \{-1, 0, +1\}. \tag{3.111}$$

In Equations 3.110 and 3.111, s_{i_j} is the normalized strenth of the Zeeman components.

In addiction the Voigt function $\mathcal{H}$ is defined by

$$\mathcal{H}(a,\nu') \stackrel{\text{def}}{=} \frac{a}{\pi}\int_{-\infty}^{+\infty}\frac{\exp(-y^2)}{(\nu'-y)^2+a^2} \tag{3.112}$$

3.5.3 Solution of the RTE

For the RTE solution, according to Iniesta (2003) and Iniesta and Cobo (2016), note that the solution can be approached by looking at the *homogeneous* part and the *inhomogeneous* part. The homogeneous part of the RTE (Equation 3.102) corresponds to

$$\frac{d\mathbf{I}}{d\tau_c} = \mathbf{KI}, \tag{3.113}$$

where $\mathbf{I}$ is the solution of the homogeneous equation, that is, of the Equation 3.113. The inhomogeneous part of Equation 3.102 corresponds to the term $-\mathbf{KS}$. The inhomogeneous part of Equation 3.102 corresponds to the term $-\mathbf{KS}$, causing Equation 3.102 to be classified as inhomogeneous or *non-homogeneous*.

Let $\mathbf{I}$ be the solution of Equation 3.113, then $\mathbf{I}$ must satisfy,

$$\frac{d\mathbf{I}}{d\tau_c} = \mathbf{KI},$$

and therefore, it is necessary and useful to define a *linear morphism* (linear transformation and linear operator are names that often appear), to help describe the behavior of Equation 3.113. Let $\mathbf{O}(\tau_c,\tau_c')$ be the morphism (believe it) with the following properties,

$$\begin{aligned}\mathbf{O}(\tau_c,\tau_c'') &= \mathbf{O}(\tau_c,\tau_c')\mathbf{O}(\tau_c',\tau_c'')\\ \mathbf{O}(\tau_c,\tau_c) &= \mathbf{I}_d.\end{aligned}$$

Furthermore, suppose also that the operator $\mathbf{O}$ is able to satisfy the following property: $\mathbf{O}(\tau_c,\tau_c')$ provides the transformation of the solution $\mathbf{I}$ from 3.113 into τ_c and into τ_c', that is

$$\mathbf{I}(\tau_c) = \mathbf{O}(\tau_c, \tau_c')\mathbf{I}(\tau_c'). \tag{3.114}$$

Note now that Equation 3.114 implies that

$$\frac{d\mathbf{I}}{d\tau_c} = \frac{d\mathbf{O}(\tau_c, \tau_c')}{d\tau_c}\mathbf{I}(\tau_c'). \tag{3.115}$$

From Equations 3.113 and 3.114, it can be concluded that

$$\frac{d\mathbf{I}}{d\tau_c} = \mathbf{K}\mathbf{I} = \mathbf{K}(\tau_c)\mathbf{O}(\tau_c, \tau_c')\mathbf{I}(\tau_c) \Rightarrow \tag{3.116}$$

$$\frac{d\mathbf{I}(\tau_c)}{d\tau_c} = \mathbf{K}(\tau_c)\mathbf{O}(\tau_c, \tau_c')\mathbf{I}(\tau_c'). \tag{3.117}$$

Also, note that by Equations 3.115 and 3.117 the following relationship can be implied

$$\frac{d\mathbf{I}}{d\tau_c} = \frac{d\mathbf{O}(\tau_c, \tau_c')}{d\tau_c}\mathbf{I}(\tau_c') = \mathbf{K}(\tau_c)\mathbf{O}(\tau_c, \tau_c')\mathbf{I}(\tau_c') \Rightarrow \tag{3.118}$$

$$\frac{d\mathbf{O}(\tau_c, \tau_c')}{d\tau_c} = \mathbf{K}(\tau_c)\mathbf{O}(\tau_c, \tau_c'). \tag{3.119}$$

According to Iniesta (2003), if $\mathbf{I}(\tau_c)$ is independent of τ_c, we can proceed similarly to what was done to obtain 3.119, and so get:

$$\frac{d\mathbf{O}(\tau_c, \tau_c')}{d\tau_c'} = -\mathbf{O}(\tau_c, \tau_c')\mathbf{K}(\tau_c') \tag{3.120}$$

Look again at Equation 3.102, and proceed by multiplying by $\mathbf{O}(\tau_c, \tau_c')$, and note that

$$\mathbf{O}(\tau_c, \tau_c')\frac{d\mathbf{I}}{d\tau_c} = \mathbf{O}(\tau_c, \tau_c')\mathbf{K}(\mathbf{I} - \mathbf{S}) = \frac{d}{d\tau_c}[\mathbf{O}(\tau_c, \tau_c')\mathbf{I}] - \frac{d\mathbf{O}(\tau_c, \tau_c')}{d\tau_c}\mathbf{I}(\tau_c). \tag{3.121}$$

But note that

$$\frac{d}{d\tau_c}[\mathbf{O}(\tau_c, \tau_c')] = -\mathbf{O}(\tau_c', \tau_c)\mathbf{K}(\tau_c)\mathbf{S}(\tau_c), \tag{3.122}$$

Integrating the Equation 3.102 with respect to the optical depth between the bottom and top of the atmosphere, τ_0 and τ_1 , respectively, gives

$$\mathbf{I}(\tau_1) = \mathbf{O}(\tau_0, \tau_1)\mathbf{I}(\tau_0) - \int_{\tau)0}^{\tau_1} \mathbf{O}(\tau_1, \tau_c)\mathbf{K}(\tau_c)\mathbf{S}(\tau_c)d\tau_c. \tag{3.123}$$

Note that in Equation 3.123, the first term on the right side means that the Stokes parameters flow through the medium between τ_0 and τ_1 as if the medium had the behavior of not emitting light, which is the homogeneous solution of 3.102. While the second term of Equation 3.123 describes the contribution of emission to the final Stokes parameters.

Suppose now that the observer is located at the depth $\tau_1 = 0$, in that case, if the inner point is chosen so that it is deep enough, in other words, $\tau_0 \to 0$, then the atmosphere is sufficiently and optically thick, that no radiation emitted in τ_0 can reach the observer, that is,

$$\lim_{\tau_0 \to \infty} \mathbf{O}(0, \tau_0)\mathbf{I}(\tau_0) = 0 \tag{3.124}$$

With Equations 3.123 and 3.124, one can obtain the so-called *formal solution* of RTE, which is given by:

$$\mathbf{I}(0) = \int_0^{\infty} \mathbf{O}(0, \tau_c)\mathbf{K}(\tau_c)\mathbf{S}(\tau_c)d\tau_c \tag{3.125}$$

According to Stekel (2019), the solution of the evolution operator cannot be obtained analytically for a general atmosphere, and must be calculated by numerical methods.

From the Equation 3.119, the evolution operator can be derived, where will be given by (INIESTA; COBO, 2016)

$$\mathbf{O}(0, \tau_c) = \exp\left(-\int_0^{\tau_c} \mathbf{K}(t)dt\right) \tag{3.126}$$

3.6 Milne-Eddington approximation

For the previously obtained Equation given by 3.126, there are few exceptions regarding the solution of 3.119. A well-known case consists of a one-dimensional case where no polarization is considered, that is, $Q = U = V = 0$. Although the situation becomes more difficult to study in the presence of a magnetic field, the matrix $\mathbf{K}(\tau_c)$, according to Santiago (2004), can be written as follows:

$$\mathbf{K}(\tau_c) = \mathbf{K}_0 f(\tau_c), \tag{3.127}$$

where $\mathbf{K}_0$ is a constant matrix that does not depend on optical depth and f is a non-vector-valued function that varies as a function of τ_c. Equation 3.126 can be rewritten as

$$\mathbf{O}(0, \tau_0) = \exp\left(-\mathbf{K}_0 \int_0^{\tau_c} f(\tau_c) d\tau_c\right). \tag{3.128}$$

The simplest case, and a more useful one, consists of assuming that $f(\tau_c) = 1$, and in this case, the relation 3.127 reduces to the following equation:

$$\mathbf{K}(\tau_c) = \mathbf{K}_0, \tag{3.129}$$

The equality relation 3.129, is called the *Milne-Eddington approximation*, and requires that the matrix $\mathbf{K}(\tau_c) = \mathbf{K}_0$ be a constant matrix throughout the atmosphere. Furthermore, it can be said that Equation 3.129 has other implications such as: the damping parameter a, the line-of-sight velocity v_{LOS}, the magnitude of the magnetic field B, the tilt angle θ and the azimuth angle φ (the θ and the φ from Equation 3.103 to Equation 3.109) must be constant with respect to the optical depth τ_c. Furthermore, the line-continuous absorption coefficient η_0 must also be constant with the optical depth (SANTIAGO, 2004). Note also that the parameters mentioned above enter into the Equations 3.109 and 3.110. In the case where the 3.129 Equation is assumed, the evolution operator is as follows:

$$\mathbf{O}(0, \tau_c) = \exp\left(-\mathbf{K}_0 \tau_c\right). \tag{3.130}$$

In the Milne-Eddington case, there is an additional assumption where the source function varies linearly with optical depth, as follows

$$\mathbf{S}(\tau_c) \stackrel{\text{def}}{=} \mathbf{S}_0 + \mathbf{S}_1\tau_c = (S_0 + S_1\tau_c)(1,0,0,0)^{\text{t}} = (S_0 + S_1\tau_c, 0, 0, 0)^{\text{t}}. \tag{3.131}$$

A medium satisfying Equations 3.129 and 3.131 is said to *Milne-Eddington atmosphere*, and in this atmosphere, the formal solution of RTE given by Equation 3.125, reduces to the following equation

$$\mathbf{I} = \int_0^\infty \exp\left(-\mathbf{K}_0\tau_c\right)\mathbf{K}_0(\mathbf{S}_0 + \mathbf{S}_1\tau_c)d\tau_c. \tag{3.132}$$

Equation 3.132 can be solved analytically in parts, and therefore:

$$\mathbf{I}(0) = \mathbf{S}_0 + \mathbf{K}_0^{-1}\mathbf{S}_1. \tag{3.133}$$

The only non-zero element of $\mathbf{S}_0$ and $\mathbf{S}_1$ is the first one, so only the first column of the matrix $\mathbf{K}_0^{-1}$ must be calculated. Let Δ be the determinant of the propagation matrix $\mathbf{K}_0$ and Π defined

$$\Pi \stackrel{\text{def}}{=} \eta_Q\rho_Q + \eta_U\rho_U + \eta_V\rho_V, \tag{3.134}$$

$$\Delta \stackrel{\text{def}}{=} \eta_I^2(\eta_I^2 - \eta_Q^2 - \eta_U^2 - \eta_V^2 + \rho_Q^2 + \rho_U^2 + \rho_V^2) - \Pi^2. \tag{3.135}$$

And therefore, the entries of the vector $\mathbf{I}(0)$ (the Stokes parameters in 0), are given by

$$I(0) = S_0 + \frac{\eta_I}{\Delta}(\eta_I^2 + \rho_Q^2 + \rho_U^2 + \rho_V^2)S_1, \tag{3.136}$$

$$Q(0) = -\frac{S_1}{\Delta}[\eta_I^2\eta_Q + \eta_I(\eta_V\rho_U - \eta_U\rho_V) + \rho_Q\Pi], \tag{3.137}$$

$$U(0) = -\frac{S_1}{\Delta}[\eta_I^2\eta_U + \eta_I(\eta_Q\rho_V - \eta_V\rho_Q) + \eta_U\Pi], \tag{3.138}$$

$$V(0) = -\frac{S_1}{\Delta}[\eta I^2\eta_V + \eta_I(\eta_U\rho_Q - \eta_Q\rho_U) + \eta_V\Pi]. \tag{3.139}$$

4 METHODOLOGY, DATA AND HINODE MISSION

In this chapter, instruments, mission and data will be presented, as well as an overview of the inversion codes that will be used to achieve the general objective of the master's dissertation.

Spectropolarimeter (SP) observations will be used as a database for Stokes parameters. In addition, the mission (Hinode) is recent and has achieved great advances in the field of Solar Physics (Heliophysics), such as: High resolution observation of the Sun at visible wavelengths, discovery of multiple waves and corona heating, outflows from the active region and the solar wind and so on (SAKURAI, 2018).

An overview of the Hinode Mission will be given, delving deeper into the Spectropolarimeter (Hinode instrument), detailing the data and images that will be used and that will be about the active region AR1967, inversion methods for studying, understanding and construction of the inversion code and, finally, the main inversion codes used today.

4.1 Hinode Mission

We will use data from the Hinode Mission in the active region AR11967. The Hinode mission, is an international space observatory carrying advanced instrumentation for solar observations that was developed by JAXA (Japan), NASA (USA) and PPARC (UK), and which was launched on September 22, 2006 at 21:36 (GMT). Hinode is the successor to the Yohkoh mission (also known as Solar-A). According to Kosugi et al. (2006), the overall objective of the mission is to understand the physical links between magnetic fields near the photosphere and their energetic and dynamic consequences in the outer solar atmosphere (solar corona). And more specifically, the objectives, according to Kosugi et al. (2007) are:

a) Understand the processes of generation and transport of the magnetic field, in addition to the magnetic modulation of solar luminosity;

b) Inquire about the processes responsible for the energy transfer from the photosphere to the corona and for the heating and structuring of the chromosphere and the corona;

c) Determination of the mechanisms that are responsible for the eruptive phenomena (flares and coronal mass ejections), in addition to understanding such phenomena in the context of the Earth-Sun system space weather.

In Figure 4.1 an artist's conception of the satellite can be seen.

Figure 4.1 - Artist's conception of the Hinode satellite. The cylinder in the center (door open) is the SOT. The black box at the top is the EIS. Below the SOT we have the XRT (also with the port open).

SOURCE: Aschwanden (2018).

The word Hinode means "sunrise". The satellite has an inclination of 98.1° between the earth plane of the equator and the orbit of the satellite, which orbits around the Earth at a rate of 1° per day, which implies a continuous observation of the Sun for nine months a year (FRANZ, 2011). The satellite has three telescopes:

- The *Solar Optical Telescope* (SOT): The SOT is a solar telescope, is composed of Optical Telescopy Assembly (OTA) and its Focal Plane Package (FFP). The OTA telescope is an aplanatic Gregorian telescope that has a 50 cm clear aperture and $f/9$ design. An image of the SOT can be seen in Figure 4.2. And in Figure 4.3 we can see the polarimeter schematic. The OTA is also diffraction limited (0.2 - 0.3 arcsec) between 3,880 and 6,700 Å. In order to maintain thermal stability, the primary mirror is made of ULE and supported by titanium frameworks. At the focus of the primary mirror and at the Gregorian focus, field stops and heat rejection mirrors are located. The secondary field stop limits the field of view to 361" × 197". It can also be noted that the OTA has a collimator lens unit (CLU), the polarization modulator unit (PMU) and, behind the primary mirror, a Tip-tilt fold Mirror (CTM). The PMU is a continuous rotating wave

plate optimized for linear and circular polarization at 5173 and 6302 Å. With the CLU and CTM, the OTA will provide a stabilized parallel beam pointing to the FPP. The FPP has four optical paths. Are they:

- *Narrowband Filter Imager* (NFI): The NFI provides intensity, Doppler and vector-polarimetric images with spectral resolution of approximately ≈ 10 pm in nine spectral lines (TSUNETA et al., 2008). In addition, the NFI records filter diagrams, Dopplergrams as well as longitudinal and vector magnetograms in the spectral range of 5170 to 6570 Å and to perform this task, the NFI uses an adjustable Lyot birefringent filter (KOSUGI et al., 2007).
- *Broadband Filter Imager* (BFI):The BFI has interference filters to create images of the photosphere (CN 388.3 nm and CH 430.5 nm) and low chromosphere (Ca II H 396.9 nm) and to make blue (450.5 nm), green (555.1 nm) and red (668.4 nm) continuous measurements for irradiance studies (TSUNETA et al., 2008). An important observation to make is that the BFI and the NFI share a CCD detector and constitute the Filtergraph (FG) (KOSUGI et al., 2007).
- *SpectroPolarimeter* (SP): The SpectroPolarimeter (SP) is an off-axis Littrow echelle spectrograph that records dual-line, dual-beam polarization spectra of the F_e I 6302.5 Å and 6301.5 Å spectral lines for high-precision Stokes polarimetry (TSUNETA et al., 2008).
- *Correlation Tracker* (CT): The correlation tracker (CT) consists of a high-speed CCD camera with a real-time correlation algorithm on the FPP computer (FPP-E) that produces error signals by estimating the displacement of the bead patterns seen in the field of view. The CT camera is contained in the Focal Plane Package (FPP). The beam splitter at the inlet of the FPP optical bench feeds a small amount of light into the CT optical path. A wedge wheel is placed in front of the CCD to provide an offset of the tracking area (SHIMIZU et al., 2007).

- The *X-Ray Telescope* (XRT): The XRT consists of a Wolter I project grazing telescope that is made of Zerodur. The aperture and focal length of the mirror are, respectively, 30 cm and 2.7 m (KOSUGI et al., 2007). XRT uses grazing incidence optics for the purpose of imaging the hottest components of the solar corona (whose temperatures range from 0.5 - 10 MK) with an angular resolution that is twice the CCD of the size of 1 *pixel*, over any field of view of 34 arcmin (this is slightly larger than the solar diameter,

in addition it is possible to capture an image of the Sun when pointed towards the center of the Sun) (ASCHWANDEN, 2018). The XRT stands out for having the widest coverage of any coronal imager to date and an unprecedented combination of field of view and spatial resolution (GOLUB et al., 2007). A heated debate was held in the initial phase of the Hinode Mission (1994 - 1996) about which optics the mission should use: normal incidence optics or grazing incidence optics. While grazing incidence optics are sensitive to all temperatures, normal incidence optics can provide better resolution. A balanced approach was chosen in relation to the scientific interests of resolution, temperature range and field of view. The grazing incidence optics was chosen (KANO et al., 2007).

- The *Extreme-Ultraviolet Imaging Spectrometer* (EIS): The EIS is a normal incidence spectrometer in the extreme ultraviolet (EUV) wavelength range and produces spatially resolved spectra in the two wavelength ranges 17.0 - 21.2 nm and 24.6 - 29.2 nm. The EIS has a spatial resolution of approximately 2" and a field of view of 560" × 521" (ASCHWANDEN, 2018). The EIS is designed to observe and analyze plasmas in the temperature range of 0.1 MK (upper transition), to 10 Mk (lower corona). Furthermore, the EIS is an off-axis paraboloid telescope with a diameter of 15 cm and a focal length of 1.9 m. Regarding the spacecraft pointer, the primary mirror has a mechanism that can be used to compensate for the EIS field of view in the E - W direction. The mirror illuminates several slits that are placed at the focus of two multi-layer toroidal grids that spread the spectrum across two rear-illuminated CCD detectors (KOSUGI et al., 2007). For Doppler speeds the velocity resolution is 3 km.s^{-1}. With the spacecraft's higher sensitivity and higher telemetry rate, the EIS can achieve a time cadence of 0.5 s in flares and ≈ 10 s in active regions. The EIS has a control system designed to optimize the use of telemetry allocation, and which provides the flexibility to select the combination of spectral lines, image regions, and time cadence of an observation to match specific scientific objectives (KOSUGI et al., 2007). And therefore, the EIS contribution to mission objectives involves measuring line intensities, Doppler velocities, line widths, temperatures, and densities for the plasma in the Sun's atmosphere. From these measurements, the EIS will investigate the physical processes that prevail at very different size scales on the Sun (CULHANE et al., 2007).

Figure 4.2 - Optical layout of the SOT including the OTA and the FPP.

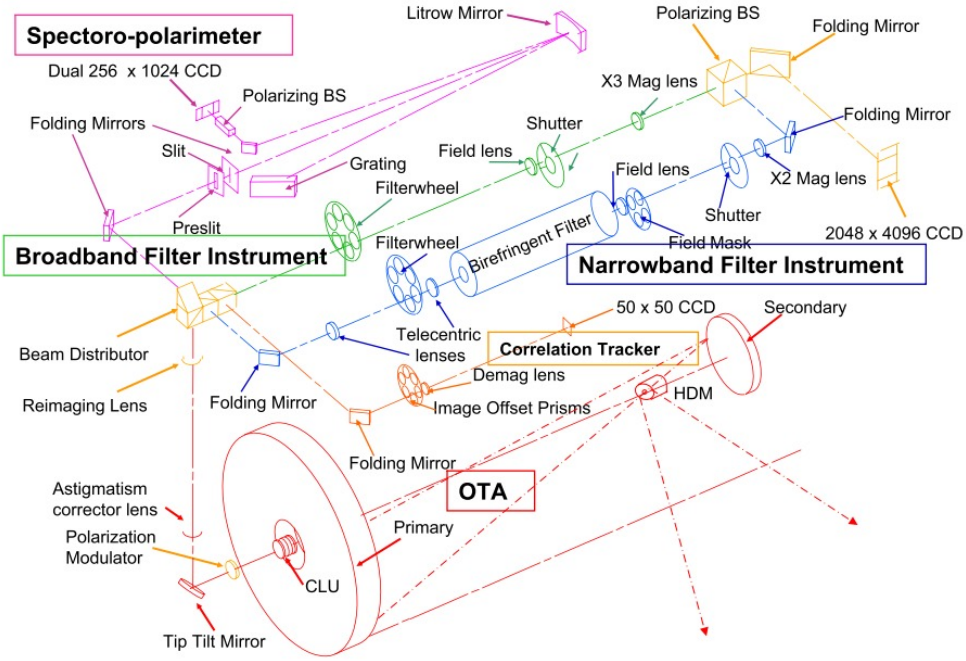

SOURCE: Tsuneta et al. (2008).

4.2 SpectroPolarimeter (SP)

The Hinode Mission's SpectroPolarimeter (SP) is the first high-precision instrument for high-resolution solar observations in space. As far as the ground-based spectropolarimetric instruments previously developed from the Hinode Mission are concerned, it can be said that they were advanced equipment capable of accurately measuring the magnetic field vector, magnetic field variations, other properties of the plasma along the line of sight and etc. And this precision that such equipment had is due to the high information content of the lines profiles recorded in their full polarization state (that is, recorded in the four Stokes parameters). The Hinode SP has a limitation of being able to register only a one-dimensional slice of the solar surface at a time. However, this limitation does not make the SP less advantageous than the ground-based spectropolarimetric equipment used before the Hinode Mission, since the limitation of recording only a one-dimensional slice of the surface at a time is compensated for by the simultaneous polarimetric measurements of the NFI instrument.And the joint action of these instruments can provide a more complete picture of the magnetic and dynamic state within the solar atmosphere than ground-based equipment (LITES et al., 2013).

Figure 4.3 - Representation of the SOT.

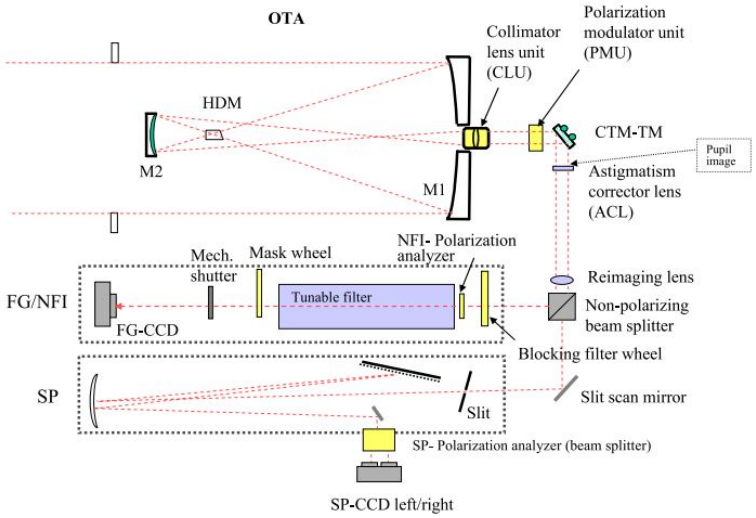

SOURCE: Ichimoto et al. (2008).

The SP operates in a fixed band of wavelengths, which are all centered on the spectral lines $Fe\ I$ and which respond to the Zeeman effect at a wavelength of 6302 Å. According to Lites et al. (2013), the $Fe\ I$ lines were chosen for the following reasons:

a) The properties of forming the pair of closely spaced lines of the same multiplet (the multiplet 816) are similar, however, the response in terms of sensitivity to the Zeeman effect is different. This in turn allows a more accurate determination of field strength, field orientation to lines-of-sight (LOS) relative to a single line and magnetic filling factors;

b) Low temperature sensitivity compared to other lines (whose wavelengths are not even close to 5250 Å) due to high excitation. Therefore, a good line for the Milne-Eddington atmospheric model to be applied;

c) These are lines with a well-known behavior, since they were already used as diagnostics of the magnetic field of ground-based instruments. And that makes the techniques well known;

d) Along the LOS, two lines subjected to the same analysis can be distinguished, as they allow some distinction in the variation of atmospheric properties. Such a property is due to the lines differing by a factor of 2.6 in oscillator strength;

e) They are separated into just 1 Å reducing spectral coverage;

f) The lines are in the red part of visible spectrum, so CCD detectors generally have their highest quantum efficiency.

Below, in the 4.1, we can see some instrumental characteristics of the Hinode Mission. And in the Table 4.2 can see characteristics and details of the Hinode Mission telescopes.

Table 4.1 - Hinode instrument characteristics.

Parameter	**Characteristics**
Mass	900 kg (wet), 770 kg (dry)
Power	1100 W
Size	4,0 × 1,6 × 1,6 m
Data rate	Up to 2 Mbps
Telemetry rate	32 kbps (S-band), 4 Mbps (X-band)
On-board storage	8 Gb
Orbit altitude	680 km (circular, Sun-synchronous, polar orbit)
Orbit inclination	98.1°
Orbit period	98 min
Attitude control	Three-axis stabilized
Absolute pointing	20”
Pointing determination	$\frac{X}{Y}$axes: 0.1″
Launch date	September 22, 2006
Instruments	SOT XRT EIS
Angular resolution	SOT: 0.2”, XRT: 2”, EIS: 2”
Field of view	SOT: 328” × 164”, XRT: 34’, EIS: $\leq$ 560
Temporal resolution	SOT: 3.4 s XRT: 2 s EIS: scanning 1” em 0.7s
Spectral range	SOT: 3800 – 7000 Å EIS: 170 – 212 Å,246 – 292 Å XRT: 6 – 60 Å

SOURCE: Aschwanden (2018).

Table 4.2 - Hinode telescopes.

Properties of the Hinode optical telescopes	
Solar Optical Telescope (SOT)	
Optical Telescope Assembly (OTA)	
Optics	Aplanatic Gregorian with aperture of 50 cm
Focal Plane Package (FPP)	
Wavelength and lines	Broadband Filter Instrument (BFI)
	CN (3883.0), $Ca\ II\ H$ (3968.5), CH (4305.0) Blue (4504.5), Green (5550.5), Red (6684.0)
	Narrowband Filter Instrument (NFI)
	$M_g\ I_b$ (5172.7), $Fe\ I$ (5250.2, 5247.1, 5250.6), $Fe\ I$ (5576.1), $Na\ I$ (5895.9), $Fe\ I$ (6302.5, 6301.5), $H\ I$ (6562.8)
	Spectro Polarimeter (SP)
	$Fe\ I$ (6302.5 Å, 6301.5 Å)
Sensitivity to magnetic fields	longitudinal: 1 - 5 G transverse: 30 - 50 G
Typical time cadence	Ranges from tens of seconds for photospheric images and vector magnetographs in particular lines to ≈ 1 hr for the full Stokes profiles
EUV Imaging Spectrometer (EIS)	
Optics	Off-axis paraboloid with multilayer-coated mirror and concave grating with aperture of 15 cm
Wavelength	170 - 210 Å with spectral resolution of ≈ 4000
	250 - 290 Å with spectral resolution of ≈ 4600
Velocity resolution	3 km.s^{-1} for Doppler velocity, 20 km.s^{-1} for line width
Exposure time	Milliseconds in flares tens of seconds in active regions
X-Ray Telescope (XRT)	
Optics	Modified Wolter type I grazing incidence mirror and co-aligned optical telescope
Wavelength	X-ray: 2 - 200 Å Optica: G-band (4305 Å)
Temperature discrimination	$\Delta \log T$: 0.2 (isothermal plasma)
Exposure time	4 ms - 10 s

SOURCE: Adapted from Kosugi et al. (2007).

4.3 Polarization calibration of the SOT

The optical system of the SOT can be seen in Figure 4.3, which reproduces the behavior of the components in the SOT/Hinode. The Optical Telescopy Assembly (OTA) is a Gregorian telescope that has a 50 cm aperture and contains the primary mirror, secondary mirror, Collimator Lens Unit (CLU), Polarization Modulator Unit (PMU) , tip-tilt folding mirror (CTM-TM) and the Astigmatism Correcting Lens (ACL), and these elements can act in the polarization state of incident light.

- Primary and secondary mirrors: they have ellipsoidal figures and protected silver coatings (ICHIMOTO et al., 2008);
- CLU: is an achromatic lens unit consisting of six elements of different types of optical glasses. In addition, the CLU provides the collimated beam to the FFP and creates a 30-mm ϕ pupil image between the CTM-TM and the ACL (ICHIMOTO et al., 2008);
- ACL: nearly flat parallel silica plate with a thickness of 10 mm. After assembly and testing of the Gregorian telescope, the ACL plate was installed to eliminate the small built-in astigmatism of the (TSUNETA et al., 2008) telescope and was tilted 1.5° with respect to the optical axis to avoid a reflection ghost of the collimated beam;
- PMU: bicrystalline athermic wave plate that rotates at a constant rate of 1/1.6 H_z (frequency). The delay is optimized for circular and linear polarization measurements at 630.2 and 517.2 nm (ICHIMOTO et al., 2008).

On the path between the FG and the SP the beam is split by an unpolarized beam splitter. The polarizer on the front of the adjustable filter and a polarization beam-splitter on the front of the SP-CCD provide the polarization analysis for FG/NFI and SP respectively (ICHIMOTO et al., 2008).

According to Ichimoto et al. (2008), to optimize the SOT as a polarimeter, the main features are:

1. Asymmetric configuration up to the polarization modulator (PMU): asymmetric configuration is an advantage to minimize crosstalk between Stokes $I\ Q\ U\ V$;

2. Simple rotation plate for the polarization modulator: rotating plate causes the Stokes Q, U and V to be modulated to be modulated at different frequencies and phases, the crosstalk between them is not sensitive to the absolute delay of the wave plate;

3. Rotating wave plate near the pupil image: Defects or non-conformity of the wave plate will not produce spurious intensity modulation in the detector;

4. Simultaneous measurements of both orthogonally polarized beams on the SP-CCD: spacecraft residual guidance errors will produce an intensity modulation. The crosstalk term I to QUV can be reduced by combining observables taken simultaneously in the two orthogonal polarizations.

First, let's start by defining the *polarimeter response matrix* $\mathbf{X}$,

$$\mathbf{S}' = \mathbf{X}\mathbf{S} \tag{4.1}$$

where $\mathbf{S}$ is the Stokes vector incident on the telescope and $\mathbf{S}'$ is the product of the SOT data. Determining the SP and FG/NFI $\mathbf{X}$ matrix is the purpose of SOT polarization calibration. A dummy signal produced by an incorrect evaluation of the matrix $\mathbf{X}$, and such a signal, is required to be less than the statistical noise (photon noise). Let $\mathbf{X}_r$ be the response matrix of the polarimeter used in data reduction, the error in the reduced Stokes vector can be written as,

$$\Delta\mathbf{S} = \mathbf{S}'' - \mathbf{S} = \mathbf{X}_r^{-1}\mathbf{S}' - \mathbf{S} = (\mathbf{X}_r^{-1}\mathbf{X} - \mathbf{I}_d)\mathbf{S} \tag{4.2}$$

where $\mathbf{S}''$ is the reduced Stokes vector, $\mathbf{X}$ is the response matrix of the real polarimeter, but this matrix is unknown. $\mathbf{I}_d$ is the identity matrix. Note that the matrix $\mathbf{X}_r$ has an inverse. Let $\boldsymbol{\varepsilon}$ be the four-element column vector, where the elements are ε, the error of the reduced Stokes vector of statistical noise, ε, according Ichimoto et al. (2008), is given by,

$$\delta\mathbf{S} = \mathbf{X}_r^{-1}\delta\mathbf{S}' = \mathbf{X}_r^{-1}\boldsymbol{\varepsilon} \tag{4.3}$$

In Figure 4.4, the definition of the polarization response matrix, the error in the polarization measurements and the demodulated intensity are shown.

Figure 4.4 - Definition of polarization response matrix and error in polarization measurements.

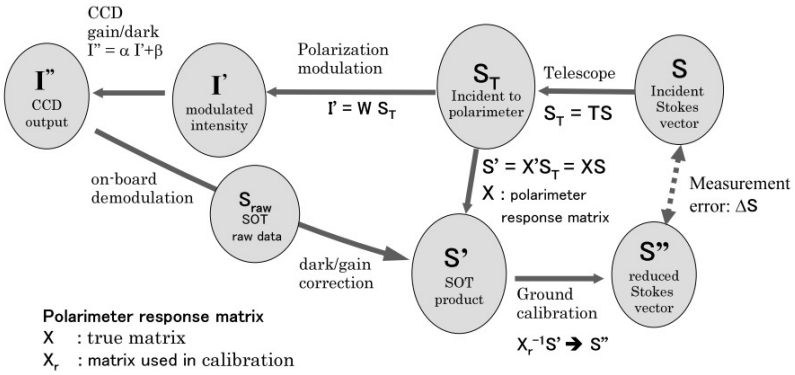

SOURCE: Ichimoto et al. (2008).

If it is required that

$$\Delta \mathbf{S} < \delta \mathbf{S} \tag{4.4}$$

by the Equation 4.4, it is possible to conclude that

$$\Delta \mathbf{X}\mathbf{S} < \boldsymbol{\varepsilon} \tag{4.5}$$

where $\Delta \mathbf{X} \stackrel{\text{def}}{=} (\mathbf{X} - \mathbf{X}_r)$ is the so-called *required accuracy for* $\mathbf{X}$.

The Inequation 4.5 says that let p_1 be the *maximum linear polarization* and p_c the *maximum circular polarization* on realistic spectral lines of the Sun. Applying $\Delta \mathbf{X}$ to the Stokes vectors representing the maximum anticipated polarization ($\mathbf{S} \in \{(1, p_1, 0, 0)^{\mathrm{t}}, (1, 0, p_1, 0)^{\mathrm{t}}, (1, 0, 0, p_1)^{\mathrm{t}}\}$ incident to the telescope) the resulting error of each Stokes parameter should be less than ε. In particular, non-diagonal elements of the $\Delta \mathbf{X}$ matrix produce a false signal of a Stokes component even when the component is zero (via the crosstalk from other Stokes components). These errors must be suppressed below the detection limit of the system, that is, ε. However, the so-called scaling error (introduced by the error of diagonal elements or the first row of matrix $\mathbf{X}$) does not produce a false signal of Stokes component if that component is intrinsically zero, but its value changes with a certain factor. One can relax the

requirement on scale errors and set the limit by an *uncertainty factor* a instead of ε, due to the uncertainties in the solar atmospheric models. After normalizing $\mathbf{S}$ by the intensity $I = 1$ and $x_{11} = 1$, the inequality for $\Delta\mathbf{X}$ can be written as follows (ICHIMOTO et al., 2008):

$$|\Delta\mathbf{X}| < \begin{pmatrix} - & \frac{a}{p_1} & \frac{a}{p_1} & \frac{a}{p_v} \\ \varepsilon & a & \frac{\varepsilon}{p_1} & \frac{\varepsilon}{p_v} \\ \varepsilon & \frac{\varepsilon}{p_1} & a & \frac{\varepsilon}{p_v} \\ \varepsilon & \frac{\varepsilon}{p_1} & \frac{\varepsilon}{p_1} & a \end{pmatrix}. \tag{4.6}$$

In case of $SOT/Hinode$, the following values are adopted (ICHIMOTO et al., 2008):

$$\begin{aligned} &\varepsilon = 0.001, \\ &a = 0.05, \\ &P_1 = 0.15 \text{ (max of Q, U)}, \\ &P_c = 0.2 \text{ (max of V)}, \end{aligned}$$

Therefore, the tolerance of $\mathbf{X}$ the Equation 4.6 becomes (ICHIMOTO et al., 2008)

$$|\Delta\mathbf{X}| < \begin{pmatrix} - & 0.333 & 0.333 & 0.250 \\ 0.001 & 0.05 & 0.007 & 0.005 \\ 0.001 & 0.007 & 0.05 & 0.005 \\ 0.001 & 0.007 & 0.007 & 0.050 \end{pmatrix}.$$

The classification of optical components in a polarimeter is given into five groups, based on their location in the optical system in relation to the polarization modulator and the analyzer. Such categories can be seen in Table 4.3. Furthermore, the $\Delta\mathbf{X}$ tolerance matrix can be used to obtain the amount of error in the diattenuation, retardation or depolarization of the elements, and this in turn implies that the error of one of the elements of $\mathbf{X}$ exceeds the tolerance of $\Delta\mathbf{X}$. In Table 4.4 you can see the calculated tolerances (ICHIMOTO et al., 2008).

Table 4.3 - Classification of polarimeter components.

	Definition	SOT components	
M_T	Elements before polarization modulator	Gregorian telescope, CLU	
M_P	Polarization modulator	Rotating waveplate (PMU)	
M_B	Elements between polarization modulator and analyzer	Tip-tilt mirror, reimaging lens, beam splitter	
		(SP) Scanning mirror Blocking filter Slit Field lens spectrograph	(NFI) Folding mirrors
M_A	Polarization analyzer	Polarizing beam splitter	Polarizer
M_F	Elements following the polarization analyzer	CCD	Filters Relay lenses Folding mirror CCD

SOURCE: Ichimoto et al. (2008).

Table 4.4 - Tolerance of polarization properties for each component.

Location	Diattenuation	Retardation (deg)	Orientation (deg)	Depolarization
M_T	0.0010 ($I \rightarrow Q$, U)	0.286 ($V \rightarrow U$)	Does not matter	0.050 (dQ,U,V)
M_P	0.0053 ($V \rightarrow U$)	3.687 (dV)	0.095 (Q - U)	0.050 (dQ,U,V)
M_B	0.0073[1] (Q - U)	0.419[2]	0.100 (U - Q)	0.050 (dQ,U,V)
M_A	Does not matter	Does not matter	0.233 (Q - U)	Does not matter
M_F	Does not matter	Does not matter	2.100 (Q - U)	Does not matter

SOURCE: Ichimoto et al. (2008).

[1]The axis of error is assumed to be 45° to the axis of the polarization analyzer. Off-axis rays from the edge of the FOV entering on the CTM-TM or the BS correspond to an axis rotation of $\approx 0.7°$.

[2]the same of 1

4.4 Data description

In the Hinode Mission, data is generated by the telescopes and their instruments and then telemetry (data) packets are generated in a certain defined format. The generated data is received by the DARTS system (Data ARchive and Transmission System). Hinode's so-called *master file* on DARTS is mirrored in data centers around the world. The data is then distributed over the internet (MATSUZAKI et al., 2007).

According to Matsuzaki et al. (2007), the aim is for the files to be portable, readable, and parsed on any machine. In view of this, the telemetry of the CCSDS packets from the Hinode Mission is reformatted to suit the format. Files fall into the following categories:

1. reformatted scientific data (which are called Level 0 or 1);
2. reformatted status data;
3. calibration data;
4. higher level products (which are called Level 2 data).

The reformatted data from item 1., which corresponds to Levels 0 and 1, according to Matsuzaki et al. (2007) is created from the observation data packages of the mission's science instruments. In addition, there is the classification of processing levels. That is, Level 0 data corresponds to raw and reformatted telemetry data (this data may also be called raw data), while Level 1 data is fully calibrated. In the case of SOT, the data is made available in the form of Flexible Image Transport System (FITS) files, which include an array of data and an array of metadata structures, which are called *FITS header* (BERGER, 2009). The header is built from telemetry data, as an example we can cite observation time, exposure time, CCD coordinates among others (MATSUZAKI et al., 2007).

In the case of SOT data, the QuickLook data is for SOT operations team members to be able to view the images within hours of obtaining the data. Entire images with the complete list of FITS keywords are contained in Level 0 data. Level 1 data is calibrated by fg_prep.pro or sp_prep.pro in addition to having units of numbers instrumental. As for level 2 data, these are processed in physical units. The Table 4.5 from Berger (2009), shows the SOT data in detail.

When it comes to how scientific data is reformatted, in SOT and XRT, uncompressed image data is written as .FITS files of multiple standard images. In the case of SOT,

Table 4.5 - Tolerance of polarization properties for each component.

Level	Pixel values	File format	Purpose
QuickLook	Data Number (DN)	FITS	Operations, Data Verification, QuickLook movies
0	DN	FITS	Basic science
1	DN/sec	FITS	Calibrated images
1.5	Physical units	FITS	SP Stokes component maps
2	Physical units	Any	e.g., vector magnetograms

SOURCE: Berger (2009).

the file unit is the raw CCD image, while for SOT/FG, the file is an observable, that is, a filter image or a set of images to generate a file. In SOT/SP, the file is shaped like a $4D$ data cube - which is the north-south direction, wavelength direction, four Stokes parameters and two light paths - at a slit position (MATSUZAKI et al., 2007). The data file format for SOT and XRT can be seen in Figure 4.5.

To get the Level 1 data from the Level 0 data, it is necessary to use the calibration data, which is made from any available data, including Level 0 data, the spacecraft pointing data, synthesis models appropriate spectrum, and so on. Level 2/Q data is generated from Level 0 and 1 data. Level Q data is generated from Level 0 data for the purpose of facilitating reporting and qualitative analysis and an example of Level Q data is the instant movies observed by XRT. To do quantitative analysis, Level 2 data is made, in addition, Level 2 data is made from Level 1 data (MATSUZAKI et al., 2007). An example of Level 2 data is the Line-of-sight velocity map, the inclination of magnetic field, azimuth and, etc.

According to (HAO) (2022), the Hinode Mission SOT/SP data products can be described as follows:

- Level 1 data: Level 1 data consists of a sequence of three-dimensional ($3D$) calibrated data that are organized into spectral $\times$ spatial $\times$ 4 Stokes parameters. In addition, such data are ready for scientific analysis. The data is then stored as individual .FITS files for each SP integration, and then grouped and stored in directories for each SP operation. The command is given by UT start time labels of this observation (ie 20061110_130011 = yyyymmdd_hhmmss). Each FITS file has a $3D$ matrix composed of

Figure 4.5 - Reformatted scientific data file format for SOT and XRT.

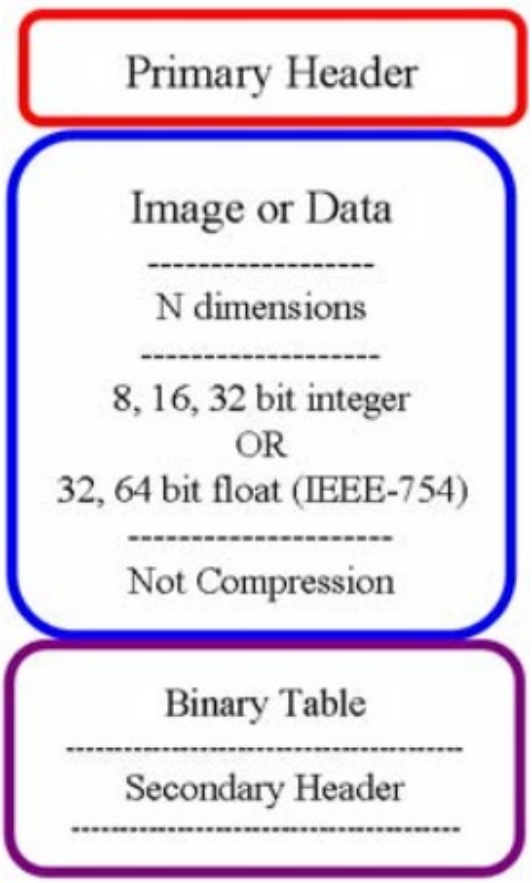

SOURCE: Matsuzaki et al. (2007).

four images, corresponding to the four Stokes parameters as a function of wavelength and position along the slit.

- Level 1.5 Quicklook: These files consist of IDL save files, which have fast analysis of Level 1 data, and as a result, images are produced as the continuum.
- Level 2 data: It can be said that the Leve 2 data is the result of the complete ME inversion of the Level 1 data. The Level 2 data is available as .FITS images, and contains various extensions (output parameters) such as magnetic field, inclination, azimuth, υ_{LOS} and etc.
- Level 2.1 data: These products are the results of the ambiguity correction in the azimuth map. From the Level 2.1 data it is possible to build the

vector map in an active region. The code used to correct the ambiguity is ME0 from Leka et al. (2009), whose source is the *Minimum Energy Algorithm* from Metcalf (1994), and which is the same algorithm used in the SDO/HMI pipeline (HOEKSEMA et al., 2014).

5 INVERSION METHODS

5.1 The inverse problem

To find solutions for the Radiative Transfer Equation, in order to obtain the values of the magnetic field vector, inversion techniques and inverse problems will be adopted for this mission.

First, the numerical solution of RTE, gives the so-called *synthetic Stokes parameters*, which are given by

$$\mathbf{I}^{syn}(\lambda) \stackrel{\text{def}}{=} \begin{pmatrix} I^{syn}(\lambda) \\ Q^{syn}(\lambda) \\ U^{syn}(\lambda) \\ V^{syn}(\lambda) \end{pmatrix}, \tag{5.1}$$

where λ is the wavelength.

In Solar Physics, inverse problems can appear, and when this occurs, it is necessary to know how to deal with the concept/definition of inversion, which is nothing more than the recovery of physical properties of the photosphere from observation data, which were obtained with the help of the spectropolarimeter. Observations provide Stokes parameters for certain wavelength positions within the absorption lines that have been considered. In the case of this study, the lines considered were the pair of lines of $Fe\ I$.

The inversion process will begin when a first estimate of atmospheric parameters is made. Parameters such as temperature, line-of-sight velocity (υ_{LOS}), orientation and magnitude of the magnetic field among others. And by the numerical solutions of the RTE, the synthetic Stokes profiles $\mathbf{I}^{syn}$ can be obtained, and after that, the next step will be to compare the synthetic Stokes profiles with the observed Stokes profiles $\mathbf{I}^{obs}$. For this, it will be necessary to introduce a metric function, which in this case will be called *Merit Function*, which will assume different behaviors and expressions depending on the problem being studied and/or addressed. The usual merit function is given by the following expression:

$$\chi^2 \stackrel{\text{def}}{=} \sum_{i=1}^{4} \sum_{j=1}^{N} \left[\frac{I_i^{syn}(\lambda_j) - I_i^{obs}(\lambda_j)}{\sigma_i} \right]^2 \omega_i, \tag{5.2}$$

where i represents the four Stokes parameters, j represents the wavelength positions, σ_i is the uncertainty in the measurement of the Stokes parameter i and ω_i which represents the weight associated with different Stokes parameters.

It is worth noting that Equation 5.2 is the usual merit function, that is, it is usually used. The ω_i weights can have many applications and one of the most common is to "scale" Stokes profiles. For a better understanding, see Figures 5.1 and 5.2.

Figure 5.1 - Note that in this case the Stokes profiles are out of scale, so it might be useful to add the weight ω_i so that the merit function χ^2 "feel" the others Stokes parameters.

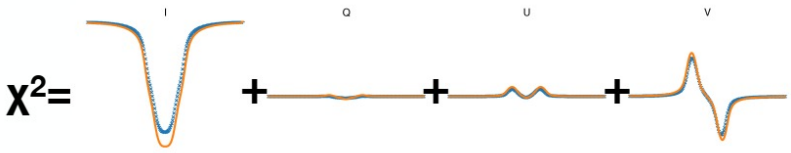

SOURCE: Centeno (2020).

Figure 5.2 - With the ω_i weight multiplied the other Stokes profiles can be "felt" by the merit function which in turn makes them more "influential" in the merit function calculation.

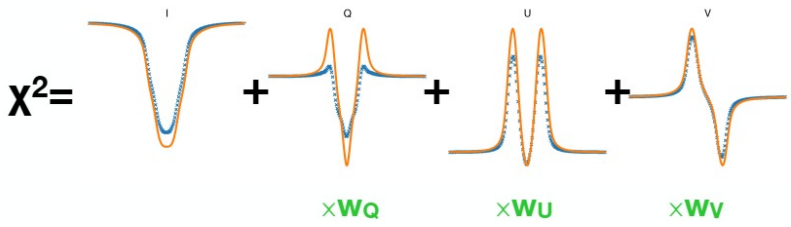

SOURCE: Centeno (2020).

Furthermore, the particular case where the weights are equal to 1 ($\omega_i = 1$, $i \in \{0, 1, 2, 3\}$) can also appear, and in this case,

$$\chi^2 = \sum_{i=1}^{4} \sum_{j=1}^{N} \left[\frac{I_i^{syn}(\lambda_j) - I_i^{obs}(\lambda_j)}{\sigma_i} \right]^2 .$$

The weighted chi-squared method (Equation 5.2) is then applied to each pixel of a one-dimensional or two-dimensional map of the solar surface, that is, the inversion of a pixel is independent of neighboring pixels. Generally, the first-mentioned estimate of atmospheric parameters is obtained via an atmosphere model for the solar surface phenomenon being considered (penumbra, umbra, etc.) or from the result of inverting a neighboring pixel. And the general inverse problem can be seen in Figure 5.3.

Figure 5.3 - The following is a representation of the general inverse problem.

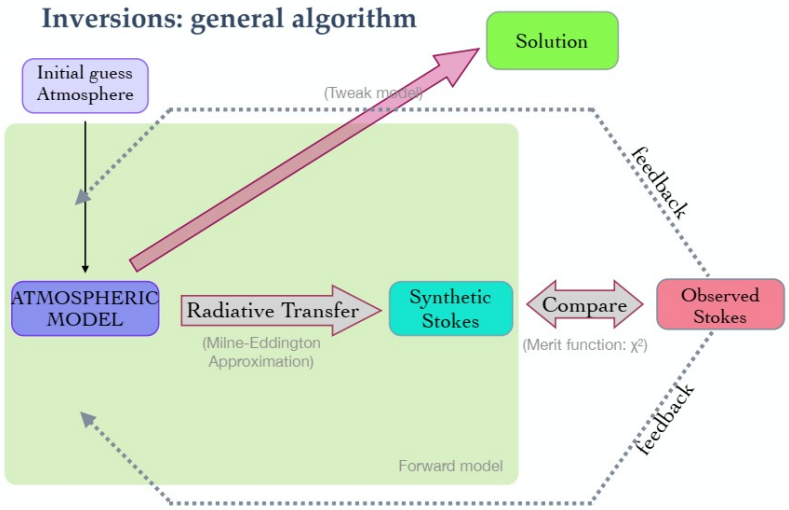

SOURCE: Centeno (2020).

5.2 Levenberg-Marquardt algorithm

The profile fitting process consists of successive and iterative approximations of the synthetic profiles $\mathbf{I}^{syn}$ in relation to the observed profiles $\mathbf{I}^{obs}$, until a minimum distance is reached (INIESTA; COBO, 2016). During the step-by-step process, the atmospheric model will undergo modifications so that the synthetic Stokes vector approaches the observed Stokes vector. And according to Iniesta (2003), when χ^2 is

close to the minimum, an expression describing the parabolic motion can be given by:

$$\chi^2(\mathbf{x}+\delta\mathbf{x}) \simeq \chi^2(\mathbf{x}) + \delta\mathbf{x}^{\mathrm{t}}\left(\nabla\chi^2 + \frac{1}{2}\mathbf{H}'\delta\mathbf{x}\right) \tag{5.3}$$

where, the gradient elements of Equation 5.3, are given by the following equation

$$\frac{\partial\chi^2}{\partial_p} = \frac{2}{\nu}\sum_{s=0}^{3}\sum_{i=1}^{q}[I_s^{syn}(\lambda_i) - I_s^{obs}(\lambda_i;\mathbf{x})]\omega_{s,i}^2 R_{p,s}(\lambda_i). \tag{5.4}$$

Therefore, note that

$$H_{i,j} = \frac{1}{2}\frac{\partial^2\chi^2}{\partial x_i \partial x_j},$$

and, where

$$\frac{\partial^2\chi^2}{\partial x_p \partial x_k} \simeq \frac{2}{\nu}\sum_{s=0}^{3}\sum_{i=1}^{q}\omega_{s,i}^2[R_{p,s}(\lambda_i)R_{k,s}(\lambda_i)]. \tag{5.5}$$

Very close to the minimum of χ^2, so

$$\nabla\chi^2 + \mathbf{H}'\delta\mathbf{x} = 0, \tag{5.6}$$

and therefore

$$\delta\mathbf{x} = -(\mathbf{H}')^{-1}\nabla\chi^2 \tag{5.7}$$

According to Iniesta (2003), the minimum may be far away and the approximation is not good enough. When such a situation happens, the best thing to do is to "go down one degree", and that means

$$\delta\mathbf{x} = a\nabla\chi^2 \tag{5.8}$$

In Equation 5.8, the constant a is required to be small enough so that the descent path is not lost. How to know the value of a? Such a question can be answered with the so-called *Levenberg-Marquardt method*, which consists in realizing that the diagonal elements of $\mathbf{H}'$ give an intuition of the value of a. Note that if $\mathbf{H}'$ were diagonal, then

$$\delta x_i = -\frac{1}{H'_{ii}} \nabla \chi^2. \tag{5.9}$$

As the scale factor in Equation 5.9 can be large, then it may be useful to have a correction factor λ. Therefore, with the gradient approximation maintained, the correct movement in the parameter space is given by

$$\delta \mathbf{x} = -\frac{1}{\lambda H'_{ii}} \nabla \chi^2 \tag{5.10}$$

And combining Equations 5.6 and 5.10, the following equation is obtained

$$\nabla \chi^2 + \mathbf{H} \delta \mathbf{x} = 0 \tag{5.11}$$

and the elements of the $\mathbf{H}$ array are defined as follows

$$H_{ij} \overset{\text{def}}{=} \begin{cases} H'_{ij}(i + \lambda), \text{ if } i = j, \\ H'_{ij}, \text{ if } i \neq j. \end{cases} \tag{5.12}$$

According to Iniesta (2003), the Levenberg-Marquardt Method follows the following algorithm:

1. Calculate the value of $\chi^2(\mathbf{x})$ with an initial guess of model atmosphere $\mathbf{x}$;

2. Adopt the value small enough for λ. It could be $\lambda = 10^{-3}$;

3. Find a solution to Equation 5.11 for $\delta \mathbf{x}$ and then calculate $\chi^2(\mathbf{x} + \delta \mathbf{x})$;

4. If $\chi^2(\mathbf{x} + \delta \mathbf{x}) \geq \chi 2(\mathbf{x})$, then minimum p is far. Therefore, the λ must be significantly increased and one must go back to step 3.;

5. If $\chi^2(\mathbf{x}+\delta\mathbf{x}) \leq \chi^2(\mathbf{x})$, then the minimum is close, and so, it is recommended to decrease λ. Update solution $\mathbf{x} + \delta\mathbf{x} \rightarrow \mathbf{x}$ and then go back to step 3.;

6. For the algorithm to stop, wait until χ^2 has a negligible decrease (between 0.1% and 1%) twice or only once. Never stop when χ^2 increases, as λ readjusts to its optimal value. This is the last step of the algorithm.

5.3 The Milne-Eddington gRid Linear Inversion Network: MERLIN

According to (HAO) (2020), the Milne-Eddington gRid Linear Inversion Network (MERLIN) consists of Milne-Eddington (ME) inversion code specifically designed to run automatically in the Hinode/SP data pipeline. Originally written in $C++$, it has an inversion scheme that is based on the least squares fit of the observed Stokes profiles using the Levenberg-Marquardt algorithm. MERLIN has the ability to make use of one or several spectral lines to recover the magnetic field vector, line-of-sight velocity, Doppler broadening, source function, macroturbulence, stray light factor, etc. Once the Hinode/SP Level 1 spectropolarimetric maps (calibrated) are approved by the quality control system, MERLIN will invert them, generating the Level 2 data.

Inversion is widely used to obtain the magnetic field vectors in the solar atmosphere. For this, it is necessary to derive from the spectral profiles of Stokes. For the inversion, it is required to fit the least squares (in some cases) of the profiles observed with a solar atmosphere model. Using the ME approximation analytical solutions for the RTE, when the lines respond to the magnetic field (Zeeman effect) (LITES et al., 2007).

ME inversions have limitations, however, such approximations provide the most accurate and accurate means for inferring the photospheric magnetic field across entire active regions. According to Lites et al. (2007), the Community Spectropolarimetric Analysis Center (CSAC) was looking for an ME inversion code that was able to satisfy the following requirements:

- robust;
- transportable;
- transparent;
- fast;

- reliable.

To satisfy these requirements, the MERLIN inversion code was chosen. In addition, MERLIN has the following characteristics:

- Written in C; data management functions in $C++$
- Initialization by ASP genetic algorithm (slow) or artificial neural network (fast);
- Built for GRID architecture for parallel computing;
- Client and server machines will communicate over TCP/IP, so data can be local or remote;
- MERLIN will serve as a model for later implementation of more sophisticated inversion techniques.

5.4 pyMilne

The inversion code that was adopted was pyMilne from Rodríguez (2019) and this code introduces some changes. First, the merit function χ^2 is changed and thus a sum of terms is added. Let $\mathbf{x}$ be the model atmosphere, o_d the $d-$th observed data point, s_d the synthetic profile, σ_d the estimate of the noise and α_k, the weight of the regularization function $\Gamma_k(\mathbf{x})$, the merit function χ^2, is given by:

$$\chi^2 = \sum_{d=1}^{N_d} \left(\frac{o_d - s_d(\mathbf{x})}{\sigma_d} \right)^2 + \sum_{k=1}^{N_p} \alpha_k \Gamma_k(\mathbf{x})^2. \tag{5.13}$$

In this modification of the χ^2 function given by 5.13, the term $\sum_{k=1}^{N_p} \alpha_k \Gamma_k(\mathbf{x})^2$ does not depend on the actual data, but depends on $\mathbf{x}$, ie the model parameters, while the term $\sum_{d=1}^{N_d} \left(\frac{o_d - s_d(\mathbf{x})}{\sigma_d} \right)^2$ depends on the data and of o_d. For the method to work, a normalization of $\mathbf{x}$ is required, and so the Levenberg-Marquardt algorithm calculates the corrections by solving the following equation

$$\mathbf{b} \stackrel{\text{def}}{=} \mathbf{J}^{\mathrm{t}}\mathbf{r} - \mathbf{L}^{\mathrm{t}}\boldsymbol{\Gamma} = (\mathbf{A} + \lambda \mathbf{I}_d \mathbf{A})\boldsymbol{\Delta}\mathbf{x} \tag{5.14}$$

In Equation 5.14, $\mathbf{A}$ is the linearized total Hessian matrix, $\mathbf{I}_d$ is the identity, $\boldsymbol{\Delta}\mathbf{x}$ is the correction for the parameters of $\mathbf{x}$, $\mathbf{L}$ is the jacobian of Γ_k, $\mathbf{J}$ is the jacobian of

s_d and λ is a parameter that can be used to solve the system predicts. The array $\mathbf{A}$ is defined by

$$\mathbf{A} \stackrel{\text{def}}{=} \mathbf{J}^{\mathrm{t}}\mathbf{J} + \mathbf{L}^{\mathrm{t}}\mathbf{L} \tag{5.15}$$

Assuming that the matrix $\mathbf{J}^{\mathrm{t}}\mathbf{J}$ is a diagonal matrix with blocks, where each block contains the hessian of a pixel, therefore, a block of the matrix can be treated independently of other blocks, and in this way, it is possible to proceed through pixel-to-pixel inversion (RODRÍGUEZ, 2019).

According to Rodríguez (2019), the purpose of Tikhonov regularization (Γ_k functions in the second term of the Equation 5.13) is to impose a level of smoothness. To ensure that the effect is achieved, we proceed by penalizing very accentuated gradients in the solutions of neighboring pixels. Given a pixel, the following function can be defined:

$$\Gamma^0_{(y,x)} \stackrel{\text{def}}{=} (p_{y,x} - p_{y-1,x}) \tag{5.16}$$

$$\Gamma^1_{(y,x)} \stackrel{\text{def}}{=} (p_{y,x} - p_{y,x-1}) \tag{5.17}$$

As the corresponding matrix $\mathbf{L}^{\mathrm{t}}\mathbf{L}$ would have, a contribution of four diagonally which is due to the cross product of $p_{y,x}$, in each row, so two contributions shifted by $\pm$ n_{par} elements of -1, and other offset contributions of $n_{par} \times n_x$ elements that are due to the cross product of $p_{y-1,x}$. When the matrix $\mathbf{L}^{\mathrm{t}}\mathbf{L}$ was added to the unconstrained Hessian matrix, there was coupling of parameters in different pixels. If $\mathbf{L}$ is known, the regularized contribution on the right is calculated by multiplying $\mathbf{L}$ by $\mathbf{\Gamma}$.

6 RESULTS AND COMPARISONS

6.1 The Hinode Mission observations

We observed and studied AR11967, which occurred on February 4, 2014 around 19:00 UT. Such an observation was made by the Hinode Mission, more specifically by the SOT telescope and the SP instrument of the Hinode Mission. The satellite observed the region from February 1st to February 6th, 2014 (OKAMOTO; SAKURAI, 2018), however the focus of this work is on February 4th, because on this day a very strong magnetic field was observed in the highlighted region of the Figure 6.1 below:

Figure 6.1 - AR11967 seen on the 4th of February 2014 around 19:00 UT. In the square, we highlight the region where a very strong magnetic field was observed. Such a magnetic field had a magnitude of approximately 6250 G.

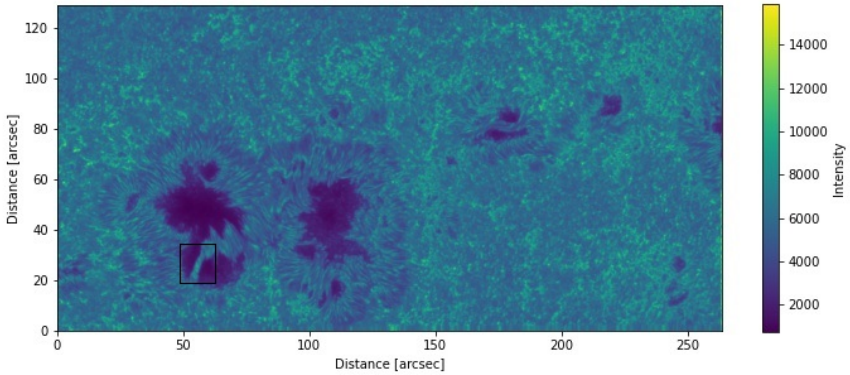

SOURCE: Author.

Stokes parameters (discussed in Section 3.1) are often used to infer properties of the solar atmosphere, and this chapter aims to present and discuss these results. The results were mainly obtained with the pyMilne inversion code from Rodríguez (2019) (see Section 5.4 for more details on the inversion code). However, it is worth remembering that simpler results such as the intensity map (see Figure 6.1), the

linear polarization maps (which indicate the intensity of the magnetic field parallel to the plane), the Stokes V (which tells you how perpendicular the plane is to the field), the continuum and so on. The above-mentioned results can be seen in Figures 6.2 (a), (b), (c) and (d) below.

Figure 6.2 - AR11967 images by different Stokes parameters and at the wavelength of the second line of the $Fe\ I$. (a) corresponds to Stokes I, which indicates luminous intensity. (b) and (c) correspond to linear polarizations that indicate the intensity of the magnetic field parallel to the plane (ie the component parallel to the plane) and are the maps of Q (to (b)) and U (to (c)). While (d) indicates how perpendicular the field is to the plane, that is, the perpendicular component, in addition to corresponding to the Stokes V.

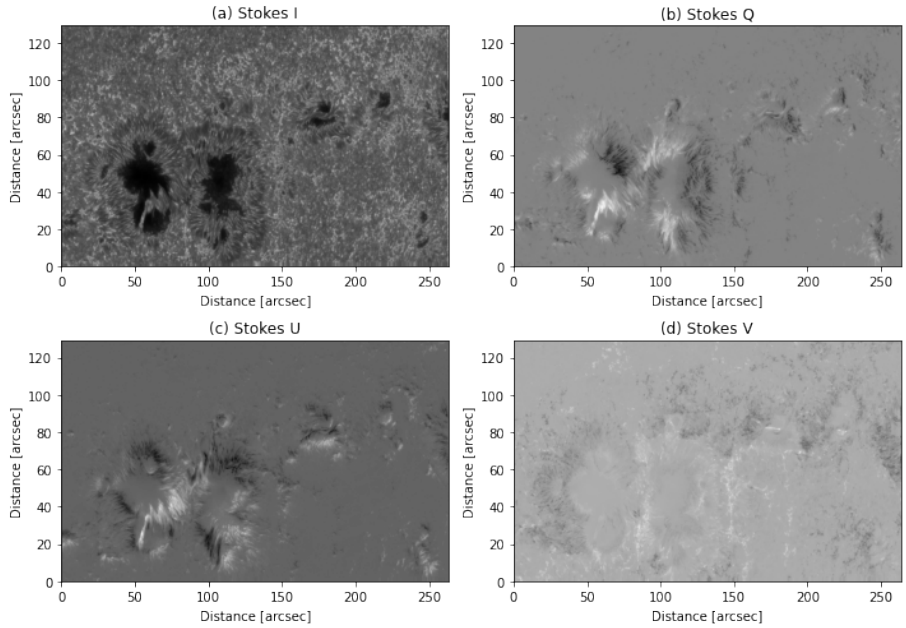

SOURCE: Author.

In addition, among the simplest results, there are also the Stokes profiles and Stokes spectrum. First, consider the four points in Figure 6.3, which were chosen to analyze different regions and behaviors of the Sun. Starting with the points (1) and (2), let the *full Stokes spectra* obtained by the Hinode Mission given in Figure 6.4 where the points (1) and (2) are highlighted on the red line of the full Stokes Spectra. Note that the point (1) is near a region that looks like a lightbridge and the point (2) is on the sunspot.

Figure 6.3 - AR11967 with four points highlighted in red: (1) in a lightbridge, (2) in the sunspot, (3) and (4) in the quiet-Sun region. The white lines serve to indicate that the points (1) and (2) are collinear as are the points (3) and (4).

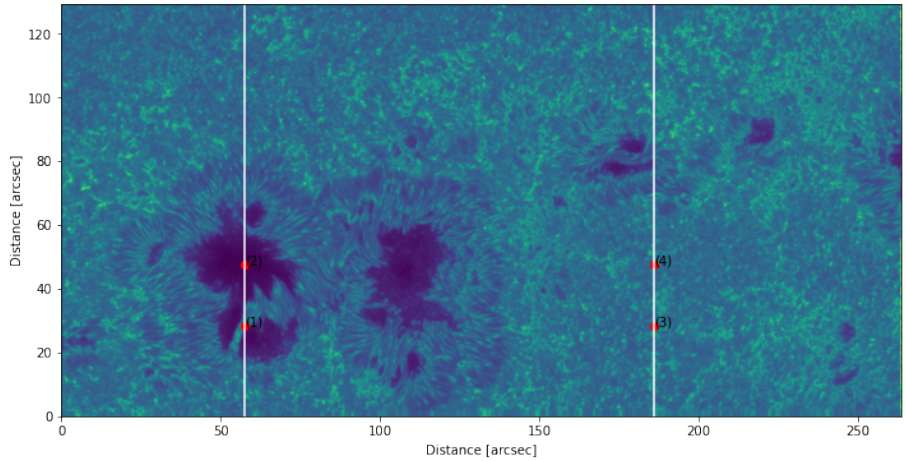

SOURCE: Author.

Note that in Figure 6.4, which represents the full Stokes spectrum. The darkest region (on the vertical axis of the Stokes I spectrum) corresponds to the sunspot heights at 6.3 where the red lines are located. Also, note the separation of the lines into components in the sunspot regions, which are responding to the Zeeman effect (see Section 3.4).

At the height of the point (1) (approximately 28.53 arcsec), the observed Stokes profiles behave as in Figure 6.5. Note that the second spectral line of $Fe\ I$ (with a wavelength of 6302.5 Å) splits into three components in Figure 6.4 which in turn, justifies the three local minima observed in the neighborhood of the 6302.5 wavelength Å in the Stokes profile I of Figure 6.5. On the other hand, at the point (2) of Figure 6.3 and also the red bar of Figure 6.4, note that this point is located on the sunspot. Thus, it can be seen in Figure 6.6 that the maximum of the Stokes I profile is much smaller than the Stokes I of Figure 6.5 because it is a region whose luminous intensity is much smaller in relation to the previous one. Also, note that the Q and U profiles also register much smaller values in Figure 6.6, which in turn shows that the magnetic field parallel to the plane is small.

In the second white line of Figure 6.3 that lies on the vertical axis at 186 arcsec, there are the points (3) and (4). And you can see the difference from the white line

Figure 6.4 - Full Stokes Spectra. The red lines correspond to the highlighted points.

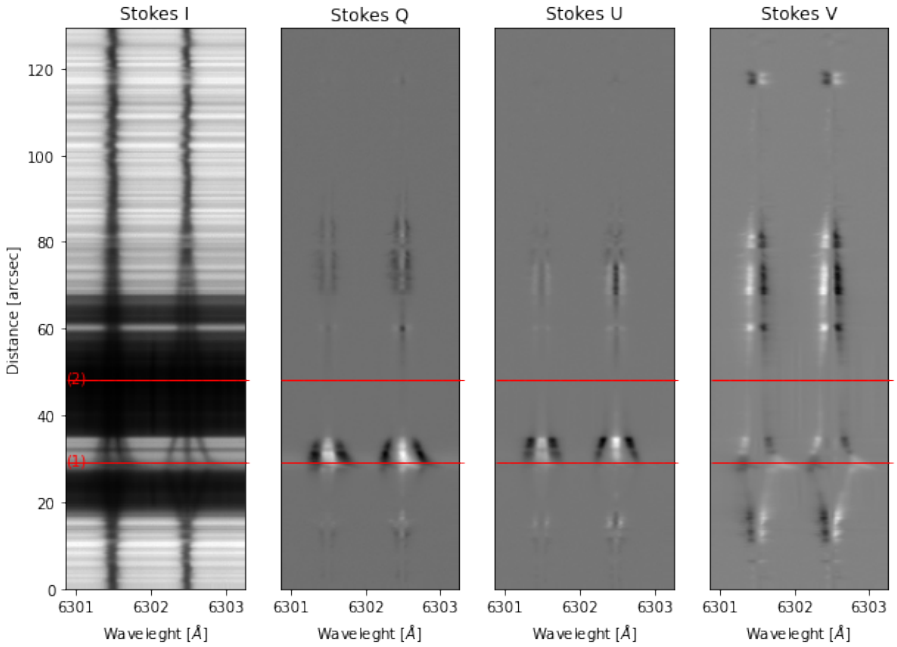

SOURCE: Author.

that is at $57,377$ arcsec horizontally. The second line (at 186 arcsec) lies in a region of the Sun known as *quiet-Sun* (low magnetic activity). In this region as the line map (full Stokes spectra) is given by Figure 6.7. Note that in this region the lines are much better behaved (which shows that it is due to the lack of magnetic activity to divide the lines). In this region, the Stokes profiles at the heights indicated in red have similar behavior (see Figure 6.8).

It is essential to calculate the continuum before presenting the observations of the Stokes profiles and spectra for the spectral line $Fe\ I$. Because the continuum provides a good overview of the active region and is also useful for the inversion process. We call *continuum*, the average of the matrices of the following discrete spectral range with eleven elements: 6302.88 Å to 6303.10 Å. It is worth mentioning that the discrete interval where the continuum is defined has eleven elements, that is, eleven wavelengths, which implies that it is an average of eleven images. The continuous figure is shown in 6.9, where the axes are in units of arcsec, but the image resolution is 408×831 pixels. The continuum is denoted by $\mathbf{I}_{cont}$ and will be used as a reference for all Stokes, as well as being useful to study the chosen active region, which is

Figure 6.5 - Here we have the observed profiles of Stokes at the height of 28.53 arcsec and passing and that correspond to the point (1) in 6.4. Note that in (a) we have several valleys of luminosity, the last three valleys that occur in a neighborhood of $6302,500$ Å, are a consequence of the division of the line responding to the Zeeman effect. In (b) and (c), we have the Stokes Q and U respectively, and in (d) the Stokes V.

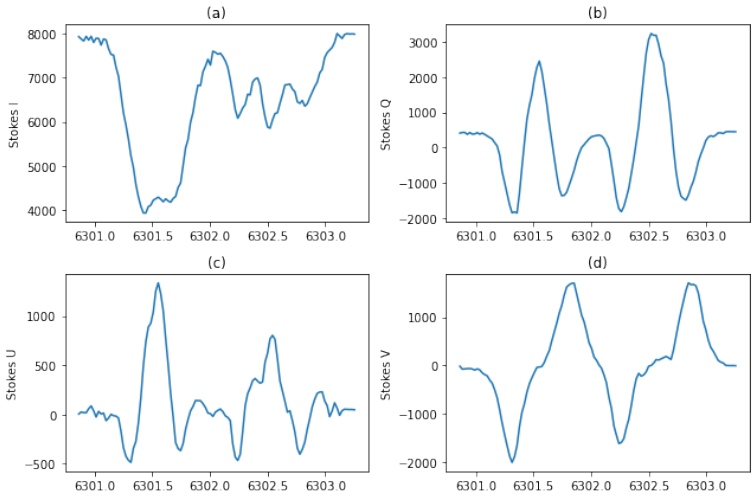

SOURCE: Author.

AR11967, where one of the strongest magnetic fields has ever been observed see Okamoto and Sakurai (2018) and Durán et al. (2020).

Figure 6.6 - Pixel profiles (2). In (a) the Stokes I, in (b) the Stokes Q, in (c) the Stokes U, and in (d) the Stokes V. The intense magnetic activity is observed in (a) and (d). The (2) pixel is a region of the sunspot umbra.

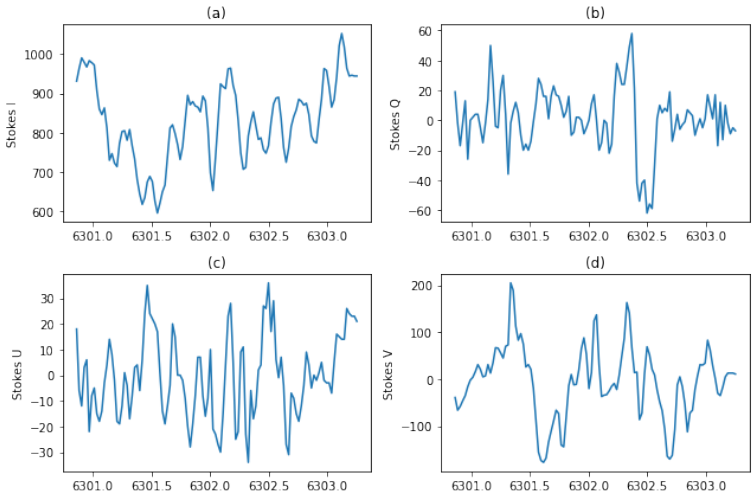

SOURCE: Author.

Figure 6.7 - The following image illustrates the full Stokes spectra for the region where the second white line is located. As already mentioned, this region is an example of the quiet-Sun, which is a region characterized by low magnetic activity. Note that the lines remain well behaved.

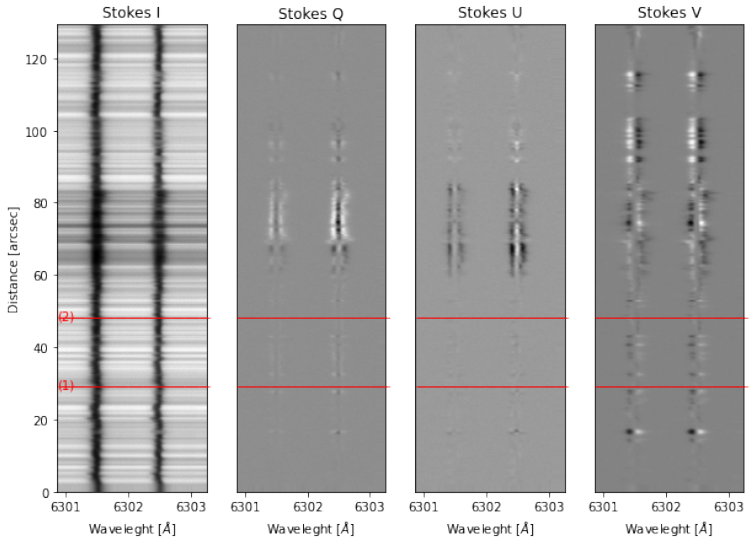

SOURCE: Author.

Figure 6.8 - In the following Stokes profiles, we have the spectra at the height of 28.53 arcsec in the blue color line and the spectra at the height of 47.55 arcsec, where in (a) we have the Stokes I, (b) the Stokes Q, (c) the Stokes U, and (d) the Stokes V. Note also that the behavior of the profiles observed are very similar.

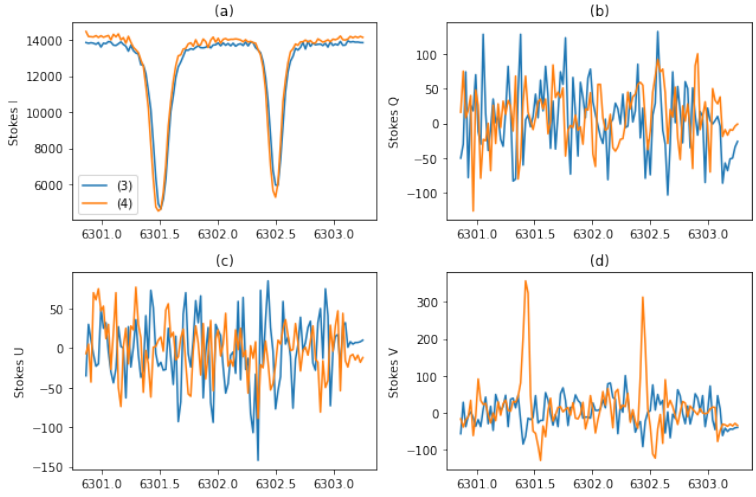

SOURCE: Author.

6.2 Continuum

As stated earlier, the definition adopted was a continuum, it was the average of matrices representing the Stokes I between the wavelengths corresponding to 6302.88 Å to 6303.1 Å (the range from 6302.88 Å to 6303.10 Å is discrete, so it's average is over eleven wavelengths). The continuum maps are useful as they can facilitate the study in several ways, in particular, to "normalize" Stokes profiles, "normalize" maps, as well as helping to identify active regions and bright spots. It is worth mentioning that other definitions of continuum can be adopted in the scientific literature.

According to Silva (2017), the formation of the spectral line is proportional to the height in the solar photosphere, and thus, the study of the shape of structures in different layers of the solar photosphere becomes possible.

Figure 6.9 - Image of the continuum ad AR11967. The continuum image was obtained by averaging matrices of the spectral range from 6302.88 Å to 6303.10 Å. And the colorbar shows the intensity.

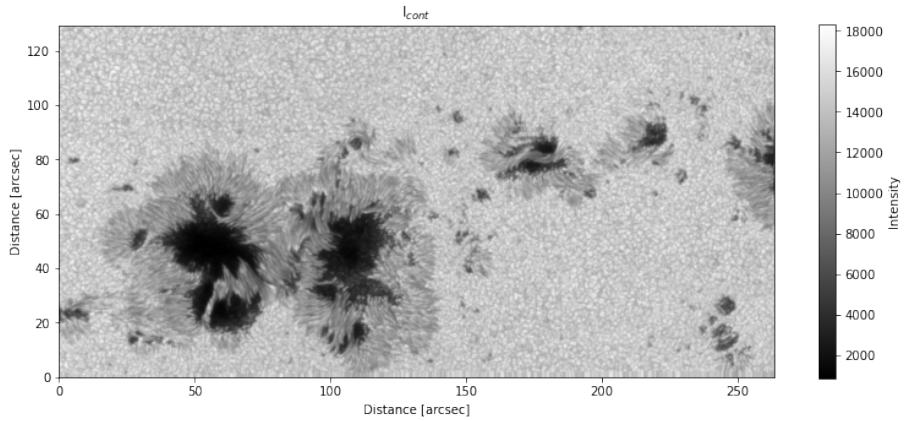

SOURCE: Author.

Figure 6.9 illustrates the continuum of AR11967 that was obtained with our definition. Let $\mathbf{I}_{cont}$ represent the continuum images, we can define the *continuum images* from $\mathbf{I}_{cont}$, as follows:

$$\mathbf{S}_{i,\lambda} \stackrel{\text{def}}{=} \frac{\mathbf{M}_i}{\mathbf{I}_{cont}},\ i \in \{I, Q, U, V\} \tag{6.1}$$

where $\mathbf{M}_{i,\lambda}$ is the image matrix of Stokes parameters generated at wavelength λ and $\mathbf{S}_{i,\lambda}$ is the matrix continuum image of Stokes parameter $i \in \{I, Q, U, V\}$ generated at wavelength λ.

In Figure 6.10, we have an image where the definition of Equation 6.1 is used for $\lambda = 6302.5$ Å.

Figure 6.10 - The following image shows $\mathbf{S}_{i,\lambda}$ for each of the $i \in \{I, Q, UV\}$ and for $\lambda = 6302,500$ Å. (a) $\mathbf{S}_{I,6302,500\ \text{Å}}$. (b) $\mathbf{S}_{Q,6302,500\ \text{Å}}$. (c) $\mathbf{S}_{U,6302,500\ \text{Å}}$. (d) $\mathbf{S}_{V,6302,500\ \text{Å}}$.

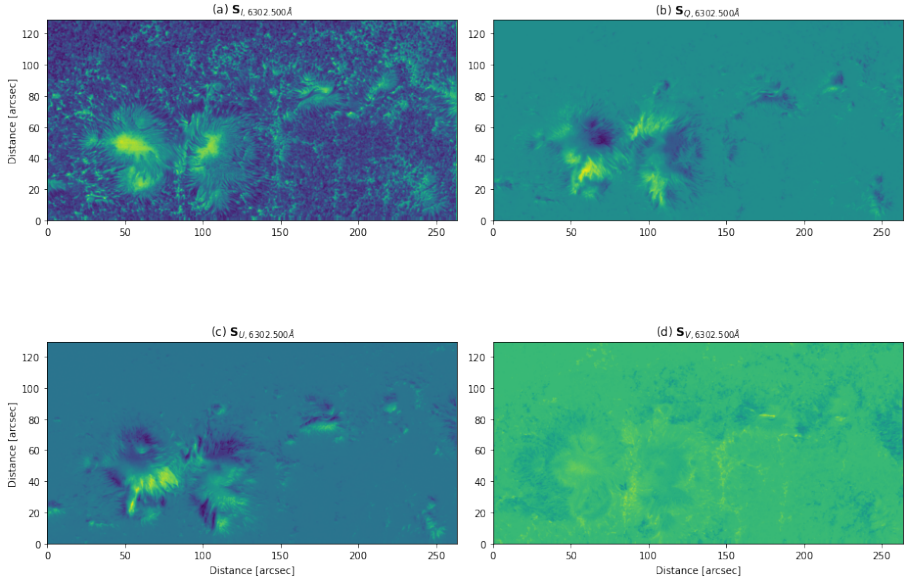

SOURCE: Author.

In the case of the full Stokes spectra that contain the points (1) and (2), which can be seen in Figure 6.11, it can be seen that the images were "filtered", or with reduced noise, so that the spectral lines of iron $Fe\ I$ become more visible in addition to showing the separation into components due to the strong magnetic field observed at points (1) and (2). While in the other two regions of quiet-Sun, which can be seen in the red lines (3) and (4), it can be seen that few differences are noticed.

With the division by the continuum $\mathbf{I}_{cont}$ new Stokes profiles can be obtained, profiles that have the same behavior as those observed in 6.5, 6.6 and in 6.8. The Stokes profile V/I_{cont} reaches higher peaks for points (1) and (2) (which are located in a

Figure 6.11 - Below is the full Stokes spectra of the four Stokes parameters and indicating the location of the points (1), (2), (3) and (4) on the four red lines. The four full Stoke spectra of the first line show a region with strong magnetic activities. The four full Stokes spectra of the second row show a quiet-Sun region.

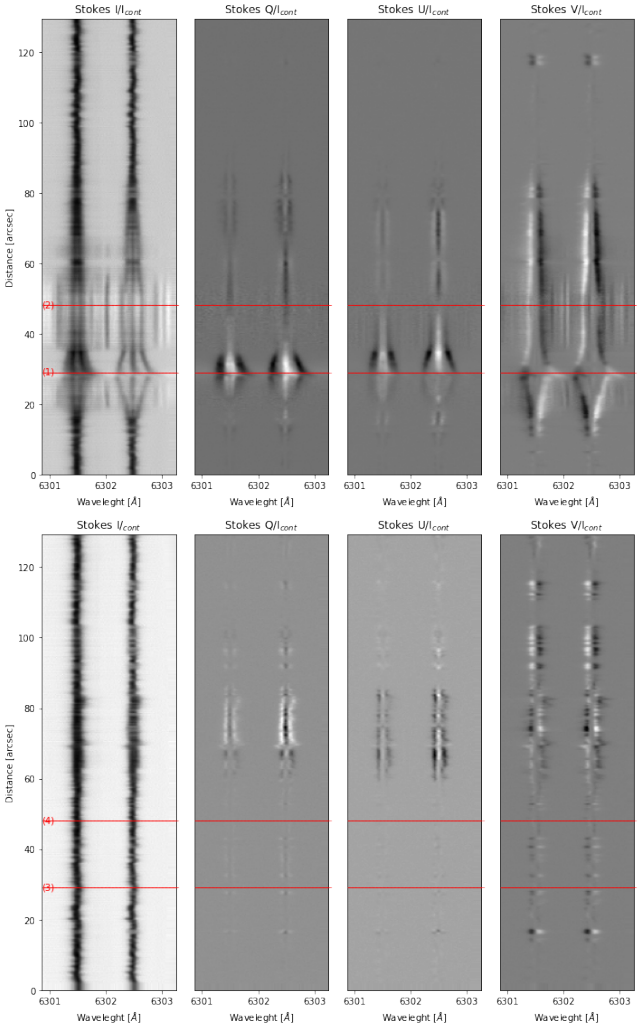

SOURCE: Author.

region of intense magnetic activity) than for points (3) and (4) (which is a quiet-Sun region), which indicates that in the regions (1) and (2) the magnetic field is closer to being perpendicular than in the regions of the points (3) and (4). Furthermore, the absence of a magnetic field in (3) and (4) is also evidenced in the Stokes profiles Q/I_{cont} and in U/I_{cont}.

In Figure 6.12, we have the profiles of the continuum (that is, the profiles I/I_{cont},

Q/I_{cont}, Q/I_{cont} and V/I_{cont}) at each point ((1), (2), (3) and (4)) highlighted in Figure 6.3 and which shows evidence of different behaviors in each region.

Figure 6.12 - Stokes profiles for each of the points in Figure 6.3. Each Stokes parameter has four profiles. In (a) the Stokes I profiles. In (b) the Stokes Q profiles. In U the profiles of Stokes (U). In (d) the Stokes V profiles. In blue, we have the profiles of point (1). In yellow, the profiles of point (2). The green color represents the point profiles (3). And the profiles of point (4), are in red.

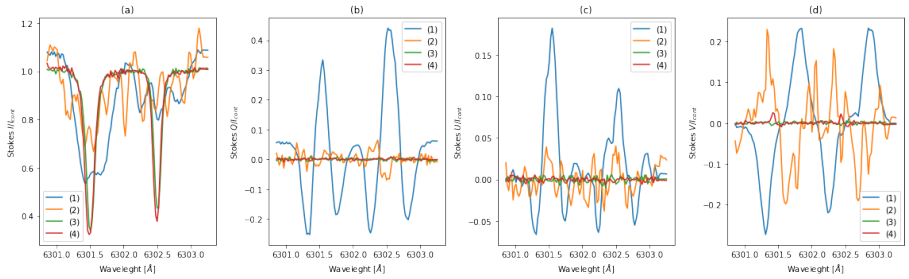

SOURCE: Author.

6.3 Synthetic lines

The shape of the polarized line (ie Stokes parameters I, Q, U and, V) is greatly influenced by various parameters of the solar atmosphere. To see the response behavior of polarized lines to atmospheric parameters, the pyMilne from Rodríguez (2019) inversion code (see Section 5.4) was employed. In this work, the solar atmosphere is described through nine parameters, such parameters that make up our model atmosphere $\mathbf{x}(\tau_c)$. The parameters are: the *magnitude* (or *intensity*) *of the magnetic field* B, the *inclination of the magnetic field* θ, the *azimuth of the magnetic field* φ, the *line-of-sight velocity* v_{LOS}, the *Doppler width of the spectral line* that can appear with the notations v_{Dopp} or $\Delta\lambda$, η_0 (see Equation 3.95), the *damping* a, S_0 and S_1 (from the ME atmosphere, see Equations 3.131 and 3.131).

Through the inversion process that uses the ME approach and atmosphere, it is possible to recover these parameters. The parameters $\Delta\lambda$, η_0, a, S_0 and S_1 are called *atmospheric parameters*. The parameters B, θ, φ and v_{LOS} are called *vector parameters*. The magnetic field vector $\mathbf{B}$ will be retrieved from the parameters B, θ, φ.

Next, we'll see how each line responds to each parameter.

In Figure 6.13, you can see how the polarized lines respond when the magnetic field varies and where the model atmosphere adopted was $\mathbf{x} = [0, \pi/4, 0.0, 0.0, 0.02, 30.0, 0.1, 0.2, 0.8]$. In this case, the analysis takes place only on the second line of $Fe\ I$ (6302.5 Å). Note that as the value of the magnetic field B increases, the profile I takes on smaller values (yellow line of 500 G) until it begins to "split", resulting in two minima (green line) until three local minima appear (purple line). The Q profile grows in the neighborhood of 6302.4 Å, decreases in the neighborhood of 6302.5 Å, and shows an increasing behavior again (starting from 6302.5) until it peaks in the neighborhood of 6302.6 Å. The U profile, for magnetic fields greater than 1000 G, starts to increase at 6302.4 Å until it peaks at 6302.5 and then decreases again. The Stokes V cancels out at 6302.5 Å, however, it may exhibit "oscillatory" behavior depending on the magnetic field strength, as seen in the green, red and purple lines ($B \geq 1000$ G), but it is not observed on the yellow line ($B = 500$ G). In the absence of a magnetic field ($B = 0$) the profiles Q, U and V are 0 (blue line).

In Figure 6.14 the adopted model atmosphere was $\mathbf{x} = [2500, \pi/4, 0.0, 0.0, 0.02, 30, 0.1, 0.2, 0.8]$ shows the behavior of polarized lines

Figure 6.13 - Synthetic lines with the parameter B varying and obtained with the initial guess atmosphere $\mathbf{x} = [0, \pi/4, 0.0, 0.0, 0.02, 30, 0.1, 0.2, 0.8]$.

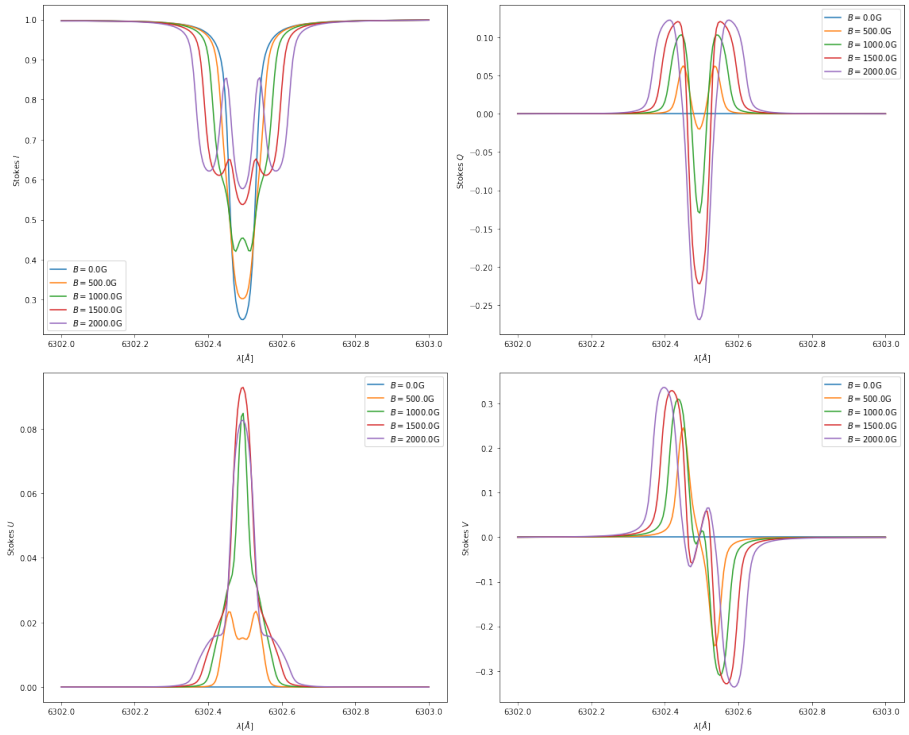

SOURCE: Author.

when the inclination θ varies. First, you can see that the Stokes I varies little after θ passes 22.5°, which leaves the lines overlapping. In Stokes Q there is a local maximum at 6302.4 Å a local minimum at 6302.5 Å and another local maximum at 6302.6 Å, where the values of local maximums increase as θ increases and those of local minimum increase in modulus as θ increases. The peak of the Stokes U parameter is reached at 6302.5 Å, but note that the local maximums get smaller and smaller as θ increases. The Stokes V profile exhibits a behavior that resembles an oscillation when $\theta \geq 22.5°$.

In Figure 6.15 the initial guess atmosphere adopted was $\mathbf{x} = [2500, \pi/2, \pi/8, 0.0, 0.02, 30.0, 0.1, 0.2, 0.8]$. Also, the figure illustrates the responses of the lines when the azimuth φ. Stokes I does not vary with azimuth, which explains the overlapping lines. Stokes Q and U exhibit the same behavior, which is a local maximum in a neighborhood of 6302.4 Å a local minimum in 6302.5 Å and another local maximum in a neighborhood of 6302.6 Å.

Figure 6.14 - Synthetic lines with the parameter θ varying and obtained with the initial guess atmosphere $\mathbf{x} = [2500, \pi/4, 0.0, 0.0, 0.02, 30.0, 0.1, 0.2, 0.8]$.

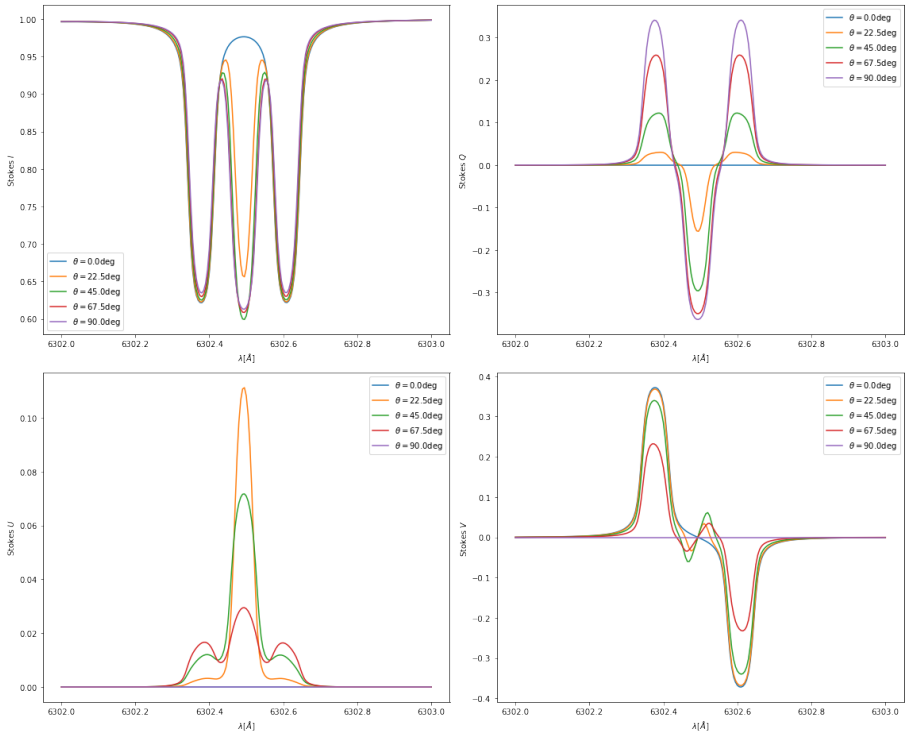

SOURCE: Author.

In Figure 6.16 the initial guess atmosphere adopted was $\mathbf{x} = [2500, \pi/2, \pi/8, 0.1, 0.02, 30, 0.1, 0.2, 0.8]$ and shows the behavior of polarized lines when v_{LOS} varies. In this case, all profiles have the same behavior, which is to shift the lines to the right as v_{LOS} increases. An important note to make is that if v_{LOS} were negative, the rows would be shifted to the left.

Figure 6.15 - Synthetic lines with the parameter φ varying and obtained with the initial guess atmosphere $\mathbf{x} = [2500, \pi/2, \pi/8, 0.0, 0.02, 30.0, 0.1, 0.2, 0.8]$.

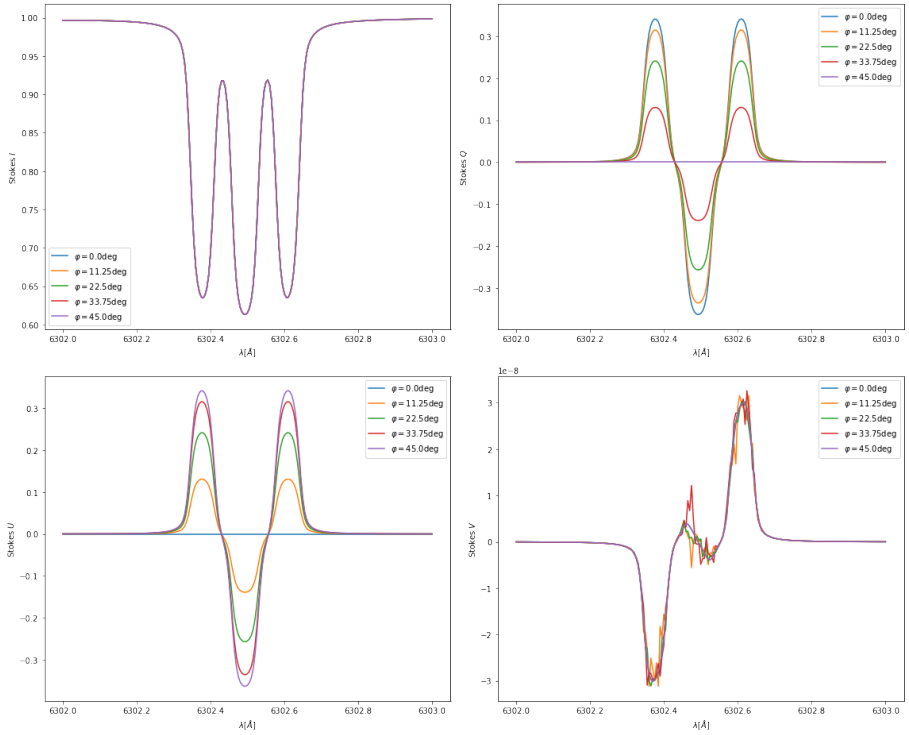

SOURCE: Author.

Figure 6.16 - Synthetic lines with parameter v_{LOS} varying and obtained with the initial guess atmosphere $\mathbf{x} = [2500, \pi/2, \pi/8, 0.1, 0.02, 30, 0.1, 0.2, 0.8]$.

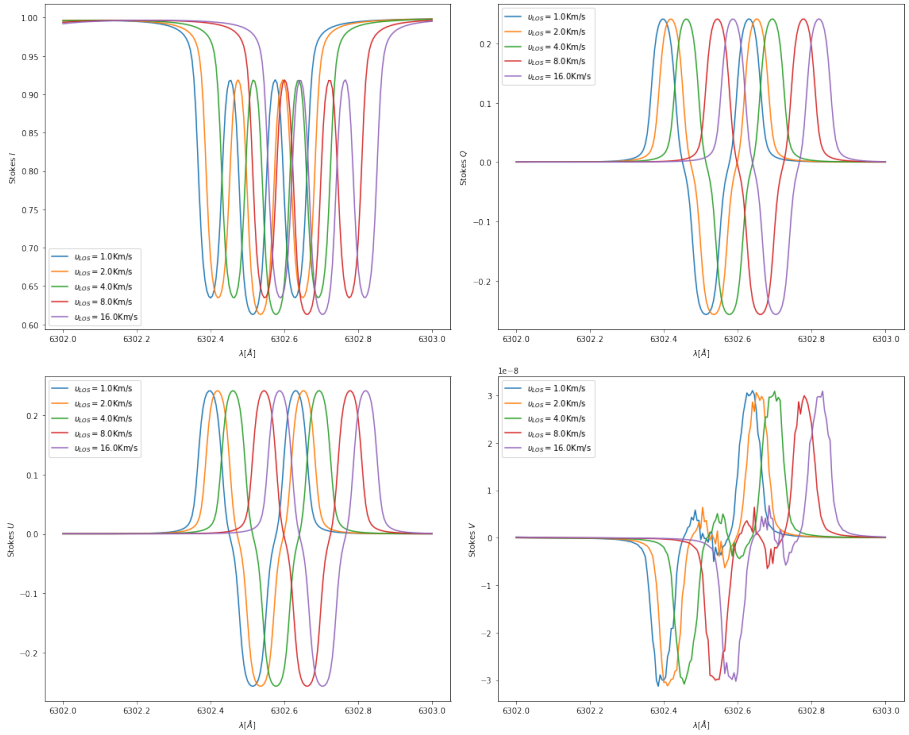

SOURCE: Author.

6.4 Inversion results: pyMilne

The focus will be on regions of interest of the study, so some pixels (points) in the AR will be considered and a comparison of synthetic Stokes profiles with Stokes profiles observed in these pixels will be made. We will also indicate the values of the parameters that were used (parameters that are elements of the model atmosphere vector $\mathbf{x}$).

Assuming that the observer looks down into the solar atmosphere and assuming z pointing down, it is possible to find the solution of the RTE (Equation 3.90) for each light beam at the point (x, y)

$$\frac{d\mathbf{I}}{dz} = \mathbf{K}(\mathbf{S} - \mathbf{I}).$$

To find a solution for the RTE, we will employ the Milne-Eddington inversion code pyMilne of Rodríguez (2019). With the numerical integration seen in Equation 3.97 and with Equation 3.98, the RTE can be rewritten as

$$\frac{d\mathbf{I}}{d\tau_c} = \mathbf{K}(\mathbf{I} - \mathbf{S}).$$

Our investigation in this section (and in this work) is based on the two spectral lines of $Fe\ I$, which were described in Section 3.3. Spectral synthesis was done with our spectral sampling at wavelengths ranging from 6300.8624815 Å to 6303.2544205 Å. For this part, it is attractive and interesting to mention some additional properties of the $Fe\ I$ spectral lines that were mentioned in the work of Borrero et al. (2014) and that can be seen in Table 6.1.

Table 6.1 - In the table, we have the main characteristics and properties of $Fe\ I$, such as the central wavelengths λ_0, the excitation potential of the lower level χ_{low}, the electron configurations of the lower and upper levels, α is the value of the temperature exponent, σ is the value of the exponent of the cross section, and $\log(gf)$ is the strength of the line oscillator.

Element	Ion	λ_0 [Å]	$\log(gf)$	χ_{low}[eV]	α	$\sigma/(a^2)$	Upper	Lower
Fe	I	6301.5	-0.718	3.654	0.243	840	$^5P_2$	$^5D_0$
Fe	I	6302.5	-1.165	3.686	0.241	856	$^5P_1$	$^5D_0$

SOURCE: Adapted from Borrero et al. (2014).

Furthermore, we will work with the approximation (Equation 3.129) and atmosphere (Equations 3.129 and 3.131) Milne-Eddington (ME) which supposes that some important physical parameters for the formation of the spectral line in the solar atmosphere are constants (independent of τ_c), and such parameters are η_0 (which was defined in 3.95), the damping a, the Doppler width of the spectral line ($\Delta\lambda$), the line-of-sight velocity v_{LOS}, and the parameters that form the magnetic field vector $\mathbf{B}$ (the intensity of the magnetic field B, inclination θ and azimuth).

It should also be noted that the ME atmosphere considers that the source function has a linear behavior as a function of the optical depth τ_c, as can be seen in Equation 3.131, $\mathbf{S}(\tau_c) = (S_0 + \tau_c S_1, 0, 0, 0)$.

The atmosphere model will be the same as the one mentioned in Section 6.3, which is given by

$$\mathbf{x}(\tau_c) = \mathbf{x} = [B, \theta, \varphi, v_{LOS}, \Delta\lambda, \eta_0, a, S_0, S_1] \tag{6.2}$$

As the ME inversion is generally limited to the inversion of the Stokes vector $\mathbf{I} = (I, Q, U, V)^{\mathrm{t}}$ observed in only one spectral line. If more than one line is being analyzed then make sure they are close enough in wavelength, as inverting distant spectral lines into wavelengths may require a new atmosphere model $\mathbf{x}$ for each line analyzed. The $Fe\ I$ lines in the lengths of 6301.5 and 6302.5 Å are examples of lines with wavelengths close enough for the inversion to occur without having to change the atmosphere model $\mathbf{x}$ (BORRERO et al., 2014).

Having made the previous considerations, we will show some results and comparisons. Figure 6.17, highlights four points, in three different regions of the Sun: (1) a region that resembles a lightbridge, (2) the sunspot umbra, (3) the sunspot penumbra, and (4) a quiet-Sun region. Let's analyze the behavior in each pixel corresponding to the equivalent region (continuum is for illustration only).

For the analysis of the regions indicated at the points (1), (2), (3) and (4), we will proceed by observing and synthesizing the four Stokes profiles, where the initial model atmosphere (i.e., the initial guess atmosphere) is given by $\mathbf{x} = [500, \frac{\pi}{4}, \frac{\pi}{8}, 0.0, 0.04, 30, 0.5, 0.4, 0.6]$. And then, we plot the observed and synthetic profiles. In Figure 6.18, the result is shown, and note that the first line corresponds to the Stokes profiles I, the second line corresponds to the Stokes profiles Q, the third line corresponds to the Stokes profiles U and the last line to the Stokes V

Figure 6.17 - Intensity of the continuum from Hinode/SOT observations of AR11967 showing the location of pixels that will be inverted through the inversion process. Four distinct points were selected to study different behaviors of different regions of the Sun. The (1) pixel is a region that resembles a lightbridge, the (2) pixel is an umbra region, the (3) pixel is a penumbra, and the (4) pixel is a quiet-Sun region.

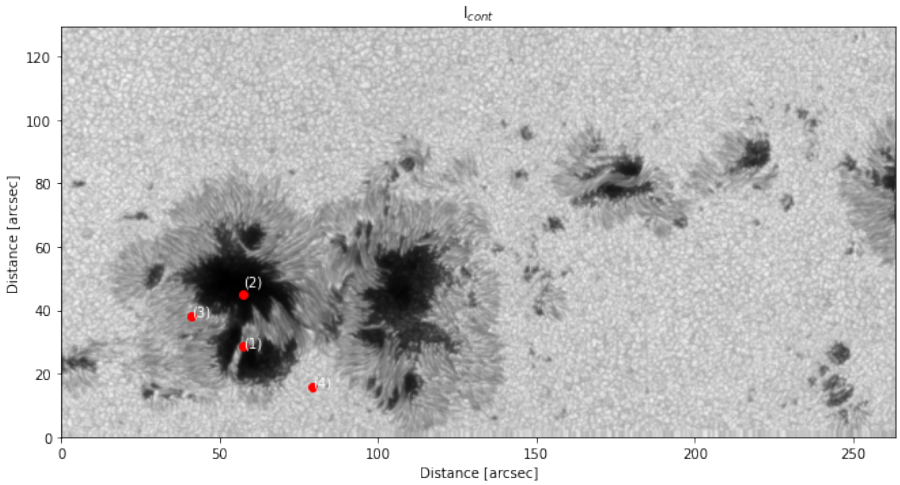

SOURCE: Author.

profiles. Note also that the columns indicate the region analyzed.

The point (1) highlights a region that resembles a lightbridge. Based on a qualitative analysis of the synthetic lines presented above, the Stokes I synthetic profile indicates that a very intense magnetic field whose both in a neighborhood of 6301.5 Å and in a neighborhood of 6302.5 Å. In fact, later on, we will see that the magnetic field in this region is one of the strongest ever observed (see Durán et al. (2020) and Okamoto and Sakurai (2018), in addiction being a very interesting region because there is a debate about whether or not this region is a lightbridge). The synthetic Stokes V profile reinforces that the magnetic field at that point is very strong.

At the point (2), which is located in the sunspot umbra, it can be seen that as in the synthetic line of I presented earlier (see Figure 6.13), the magnetic field is very intense, which is intuitive. The parameters Q, U, and V also indicate a strong magnetic field; but note that, in the Stokes V of the point (2) the observed behavior is to cross the horizontal line (assuming the value of 0) only once (assuming we are observing for the values of the neighborhood of 6302.5 Å where 0 is only hit once).

Figure 6.18 - Below, the comparison of the observed Stokes profiles (Obs) and the synthetic profiles (Fit). In *first column*, it is possible to observe the profiles at point (1), in *second column*, profiles at point (2), profiles at point (3) can be observed in *third column*, and those of point (4) in *fourth column*.

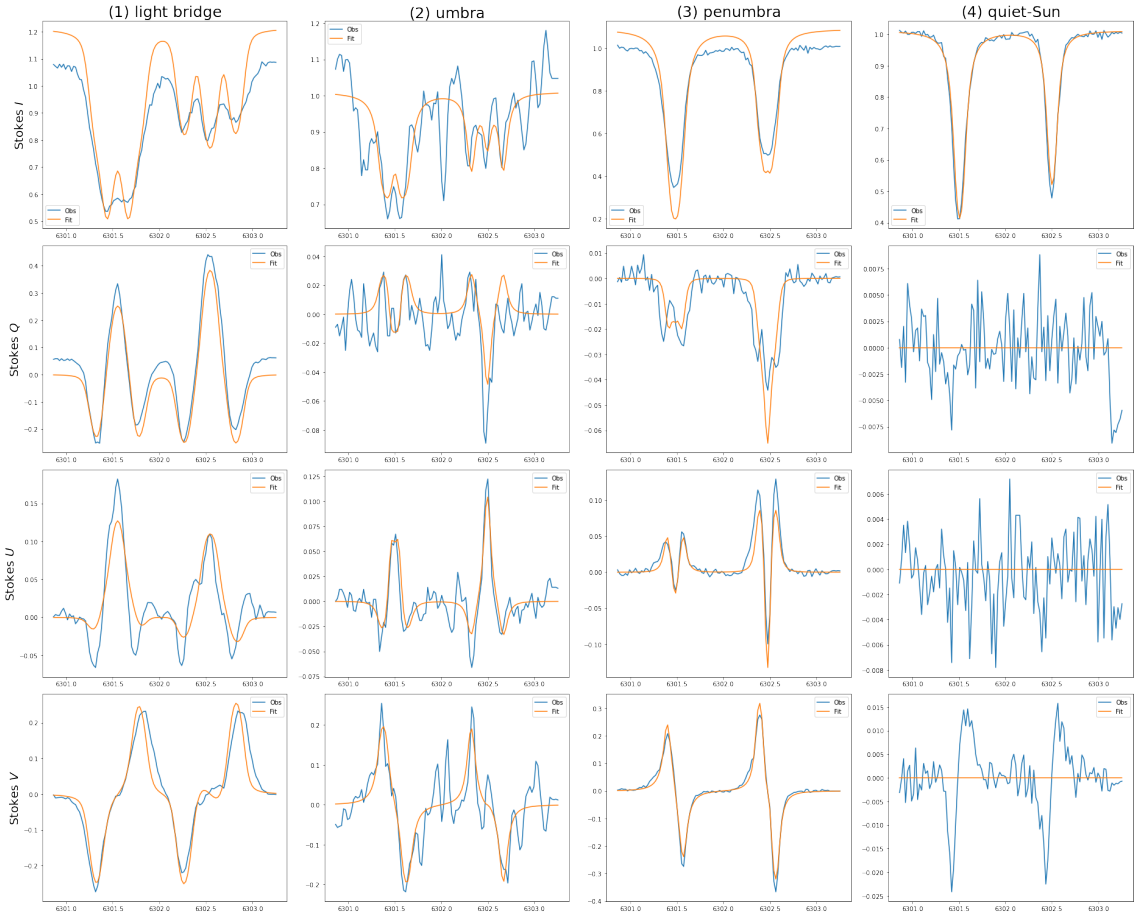

SOURCE: Author.

Such behavior is different from that observed at point (1), wherein a neighborhood of 6302.5 Å we can observe a behavior similar to Stokes V in Figure 6.13 for fields greater than or equal to 1000 G, that is, the observed magnetic field in (1) is greater than in (2). Furthermore, the parameters Q and U indicate that the field is emerging from the solar photosphere.

The point (3) is a penumbra region, so it is intuitive to assume that the region will have an intensity higher than a quiet-Sun region and lower than an umbra, as we can see in Stokes I. The Stokes Q and U indicate that the inclination is approximately 157.5°.

The point (4) is the simplest of the four. This is a quiet-Sun spot. At this point, there is very little variation in the observed profiles and the synthetic ones are practically constant due to the low magnetic activity.

7 RESULTS: pyMilne vs. MERLIN

In this chapter the results of pyMilne will be compared with those of MERLIN, emphasizing the so-called vector parameters, that is, the parameters B (photospheric magnetic field intensity), θ (photospheric magnetic field inclination), φ (photospheric magnetic field azimuth) and υ_{LOS} (line-of-sight velocity). But also shows the map of χ^2 with errors. It is also worth mentioning that the focus of the results was obtained by inverting the parameter maps in the second line of $Fe\ I$, that is, 6302.5 Å. Therefore, unless stated otherwise, the following results were obtained by inverting the line 6302.5 Å.

Next, a composition between B and χ^2, the line-of-sight velocity, the components of the magnetic field **B**, the comparisons will be presented.

7.1 The merit function

Knowing that the metric function χ^2 represents the errors between the synthetic profiles and the observed profiles, it can be seen in Figure 7.1 that the error is quite large (it is important to say that in this image the error was limited to 1000 for the purpose of showing that the error was very large in this region), and a large error is intuitive since one of the strongest magnetic fields ever has been observed in this region. Therefore, regions where the errors are large show an active region with intense magnetic activity and synthetic profiles with larger errors.

Figure 7.1 - In the Figure on the left, we have the magnetic field module and highlight the sunspot umbra. On the right side, the function χ^2 limited between the values of 0 and 1000, which was limited to highlight that the largest errors occur in regions of intense magnetic field such as umbras and in the region that resembles to a lightbridge.

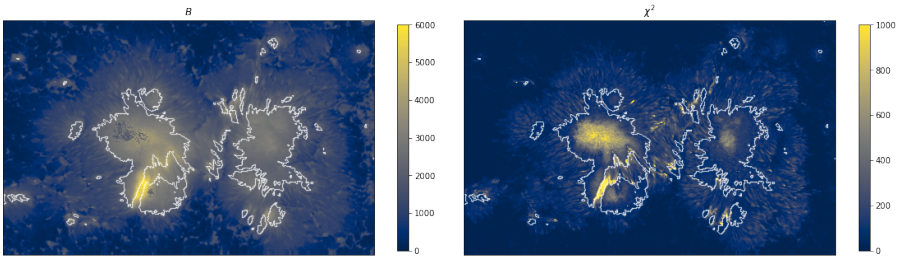

SOURCE: Author.

Also, note that the biggest errors occur in regions where the magnetic fields are strong (umbra and the region that resembles a lightbridge). See Figure 7.2, where we compare B with χ^2 figures with limiter on the first line and without the limiter on the second line. Note that in both lines the largest errors and magnetic fields are concentrated in regions with intense magnetic field.

Figure 7.2 - In the figures on the right we can see the modules of the magnetic field. And on the left side, the images of the merit function can be visualized. In the first row and column on the left, the magnetic field map has been restricted, while in the second row and first column, the magnetic field map across the entire AR is presented. In the two lines of the second column, two maps of χ^2 are presented, in the first line the map has a limiter and in the second line the map is without the limiter. With the limiter in the first row and second column, it serves to highlight that very large error values can be reached. Also in the second row and column, note that it is difficult to identify the error values. As stated in Figure 7.1, the regions where the electric field is more intense are where the highest values (errors) of the merit function χ^2 occur.

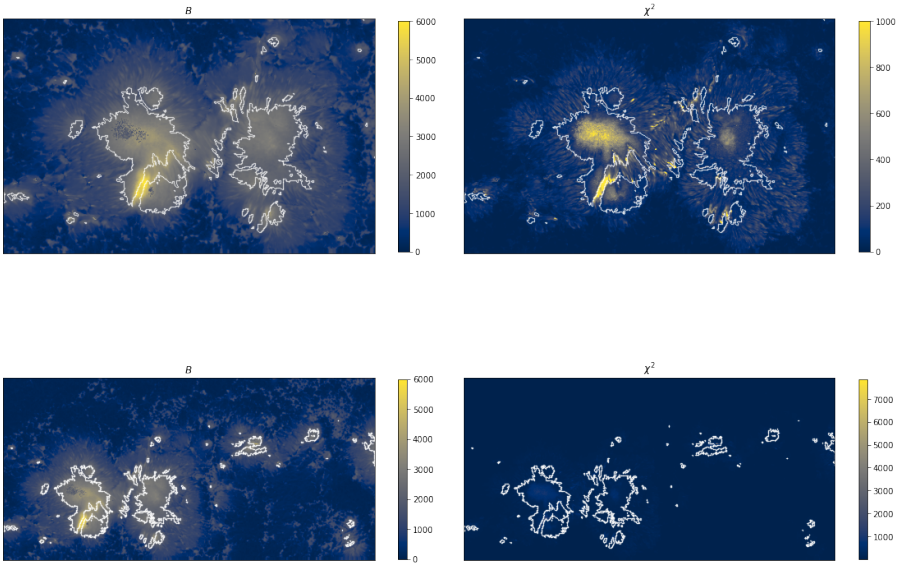

SOURCE: Author.

7.2 Line-of-sight velocity

In the first image of Figure 7.3 we can see that in $v_{LOS,pyMilne}$ blue is the dominant color, that is, blueshifted (in this case the plasma velocity is negative with respect to LOS). In the second image, the map of $v_{LOS,MERLIN}$ red is the dominant color, that is, redshifted (in this case the plasma velocity is positive with respect to LOS). Something that may explain the difference observed between the maps, whether the pyMilne map tends towards blue and the MERLIN map towards red, is the fact that for the map $v_{LOS,pyMilne}$ a correction was not applied , as we will see next. And so, the difference between the maps becomes a lighter blue.

However, in regions where the velocities are more intense, such as pixels with a darker shade of red, the maps were consistent, that is, they presented the same behavior.

For a better description of what was observed, let's consider the Table 7.1, which provides the mean, median and kurtose values of $v_{LOS,pyMilne}$ and $v_{LOS,MERLIN}$. First, from Figure 7.3, it can be qualitatively concluded that the map of $v_{LOS,pyMilne}$ of the maps has more negative velocities than positive ones, and the map of $v_{LOS,MERLIN}$ has more pixels of positive than negative velocity. However, to be sure the Table 7.1 can be useful. Note that the average value of pyMilne, which is -0.318803 km/s is negative, while the average value of MERLIN is positive and given by 0.044189177 km/s. Furthermore, the medina values, which is -0.3054303 km/s for pyMilne, and 0.04679258 km/s for MERLIN, reinforces that the map of pyMilne has more negative pixels and the MERLIN map has more positive pixels. What could explain these differences is that the MERLIN velocity map ($v_{LOS,MERLIN}$) underwent *solar rotation correction*, while the pyMilne velocity ($v_{LOS,pyMilne}$) map did not.

Table 7.1 - Avarage, median and kurtosis of the maps of $v_{LOS,pyMilne}$ and $v_{LOS,MERLIN}$.

	Average [km/s]	Median [km/s]	Kurtosis [km/s]
pyMilne	-0.318803	-0.3054303	17.843119
MERLIN	0.044189177	0.04679258	5.609894

SOURCE: Author.

Figure 7.3 - In *first line* we have $v_{LOS,pyMilne}$, in *second line*, $v_{LOS,MERLIN}$ and in *third line*, $v_{LOS,pyMilne} - v_{LOS,MERLIN}$. Teste

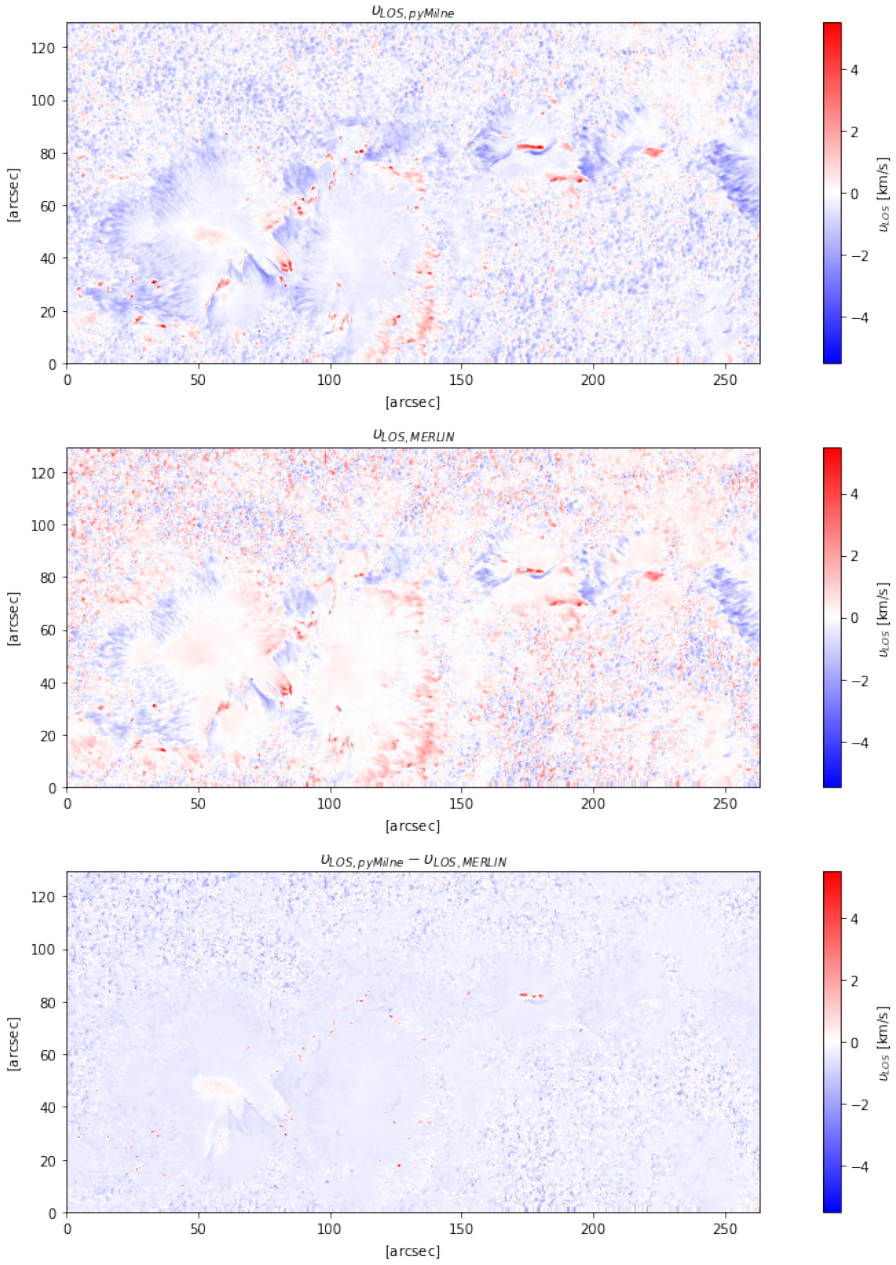

SOURCE: Author.

7.3 The magnetic field

7.3.1 The intensity

The most interesting feature that can be highlighted in the magnetic field maps is the strong magnetic field observed in the region that resembles a lightbridge. One of the strongest magnetic fields ever observed on the Sun is precisely in this region, as can be seen in the work of Sakurai (2018) (we will talk more about this region later on). In the work cited above, the magnetic fields observed in this region were approximately 6.2 kG and to estimate this value, the authors used the inversion code MEKSY. As pyMilne got a value very close to 6000 G and MERLIN got 5000 G, then it can be said that both codes have a limiter (in the case of pyMilne from 6000 G and in the case of MERLIN 5000 G), however, pyMilne was more accurate than MERLIN to estimate the magnetic field in this region. The causes of the strong magnetic field observed in this region is still a matter of debate.

In Figure 7.4, we have the comparison between the magnetic field modules. In the first line the magnitude of the field obtained by pyMilne, in the second line we have the magnitude of the magnetic field obtained by MERLIN, and the difference between the maps ($B_{pyMilne} - B_{MERLIN}$). As in the colorbar there are many values, it is more difficult to draw conclusions. Therefore, if the difference map between the B modules is restricted to the values -1000 G up to 1000 G, more conclusions can be obtained.

Table 7.2 - Avarage, median and kurtosis table of magnetic field intensity maps.

	Average [G]	Median [G]	Kurtosis [G]
pyMilne	808.06476	465.206	2.301087
MERLIN	799.7645	501.2351	2.308051

SOURCE: Author.

In Figure 7.5, the image of the difference between the maps can be seen in addition to being clearer and allowing new observations. Note that the region that resembles a lightbridge appears to have a value of approximately 1000 G, which is another indication that pyMilne was more accurate than MERLIN.

However, we can make a more quantitative analysis of the intensity of the observed magnetic field, which helps us to know, “how close” our procedure was able to get in

the comparison between the inversion codes. For that, let's consider the Table 7.2, which shows the mean, median, and kurtosis values of the maps obtained by pyMilne and MERLIN. First, note that the values were closer than the table values of v_{LOS} (7.1). Note that the average of pyMilne (808.06476 G) and MERLIN (799.7645 G) are close values. In the median, whose values have a minor distortion, the values were also close. And finally, what drew the most attention was the proximity of the kurtosis values, 2.301087 (for pyMilne) and 2.308051 (for MERLIN), which are values greater than 0 and less than 3, so being, it can be said that the maps have a probability function *leptokurtic* and that they have a more tapered distribution than the normal.

Figure 7.4 - Images illustrating the strengths of magnetic fields and the difference between them. *First line*: magnetic field strength due to pyMilne. *Second line*: magnetic field strength due to MERLIN. *Third line*: difference between the magnetic field intensity maps ($B_{pyMilne} - B_{MERLIN}$).

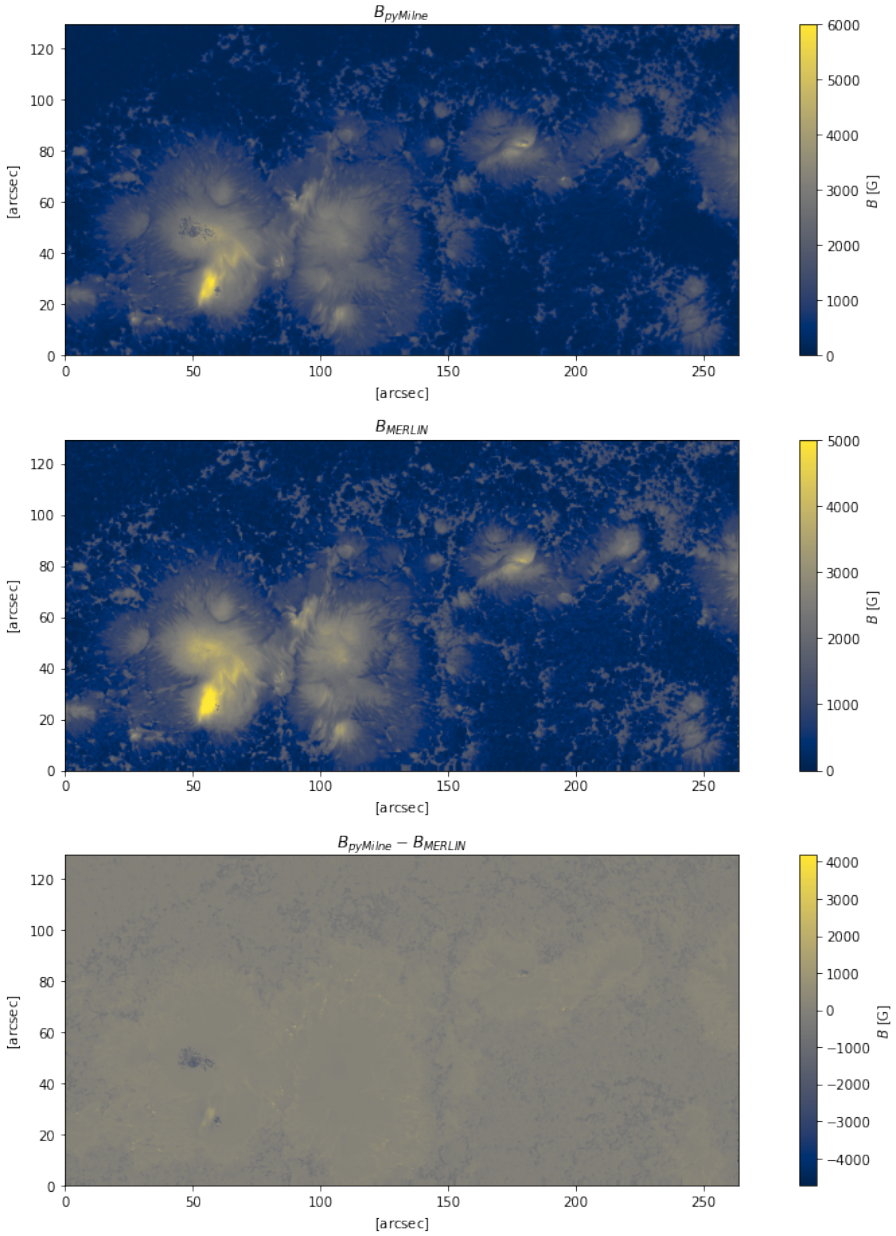

SOURCE: Author.

Figure 7.5 - Difference between magnetic field strengths, restricted between −1000 G and 1000 G.

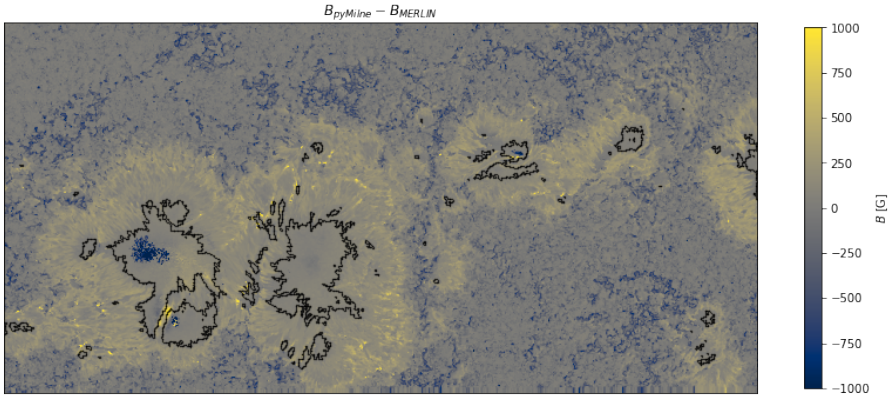

SOURCE: Author.

7.3.2 Inclination

In Figure 7.6, we have the inclination maps of the magnetic field vector that were obtained and the difference between the maps (for comparison). At a given point, the inclination maps range from 0° to 180° and represent the inclination that the magnetic field vector **B** makes with respect to the component z of the coordinate system adopted at the point. Therefore, note that in the white regions the angle is 90°, while in the purple regions the angle is 180° (field entering the plane), and finally, the brown regions represent the fields that are emerging from the plane and have an angle of 0°.

Note that when our pyMilne result produces an apparently accurate result because when compared to the MERLIN result through the difference between maps, the resulting map (see the third map in Figure 7.6) has values that are fine close to zero. Furthermore, the means, medians and kurtosis reinforce this claim (that the pyMilne result was accurate).

Table 7.3 - Avarage, median and kurtosis for maps $\theta_{pyMilne}$ and θ_{MERLIN}.

	Average [°]	Median [°]	Kurtosis [°]
pyMilne	77.90943	76.89668	−0.0807724
MERLIN	76.98434	75.29843	−0.2332747

SOURCE: Author.

And finally, and most surprising, is that the most intense magnetic field (which appeared in the region that resembles a lightbridge) has an inclination of 90°, as can be seen in Figure 7.7

In Figure 7.7, in the magnetic field map (right), the region where the yellow color tone coincides with the yellow colorbar in the 6000 G, is the same region as has a white (90 deg) in the magnetic field inclination map (right). Also, note that the sunspot on the left in both maps is brown on the magnetic field inclination map (on the right), while the sunspots on the right and south (in relation to the brown sunspot) are purple. which suggests that the magnetic field emerges from the sunspot on the right and dips into the sunspots to the south and left.

Sakurai (2018) explain that the region that resembles a lightbridge, is not a light-bridge, and for that they argue using the lilling factor, which in this case, is high in

the region that resembles a light bridge, but in lightbridges, filling factors values are low. The region that resembles a lightbridge is actually part of the southern umbra. The authors suggested that the magnetic field lines in the light bridge region are subducted by the Evershed flux where both the northern and southern umbra supposedly tried to form their own penumbra in the damping area, but the southern one dominated, and so the flow stopped. the northern umbra from forming its penumbra on the south side.

Also note that quantitatively speaking, the pyMilne inclination map ($\theta_{pyMilne}$) had a small relative difference from the MERLIN inclination map (θ_{MERLIN}), see Table 7.3. In Table 7.3, we can see that the averages and medians of the maps were very close. Furthermore, the kurtosis values are negative and therefore the distribution is flattened with respect to the normal distribution, and this behavior is called *platykurtic*. In summary, the pyMilne results for the slope were very close to the MERLIN results.

Figure 7.6 - Image illustrating the magnetic field vector inclinations and difference of inclinations. In *first line*: inclination due to pyMilne. *Second line*: inclination due to MERLIN. And *third line*: $\theta_{pyMilne} - \theta_{MERLIN}$.

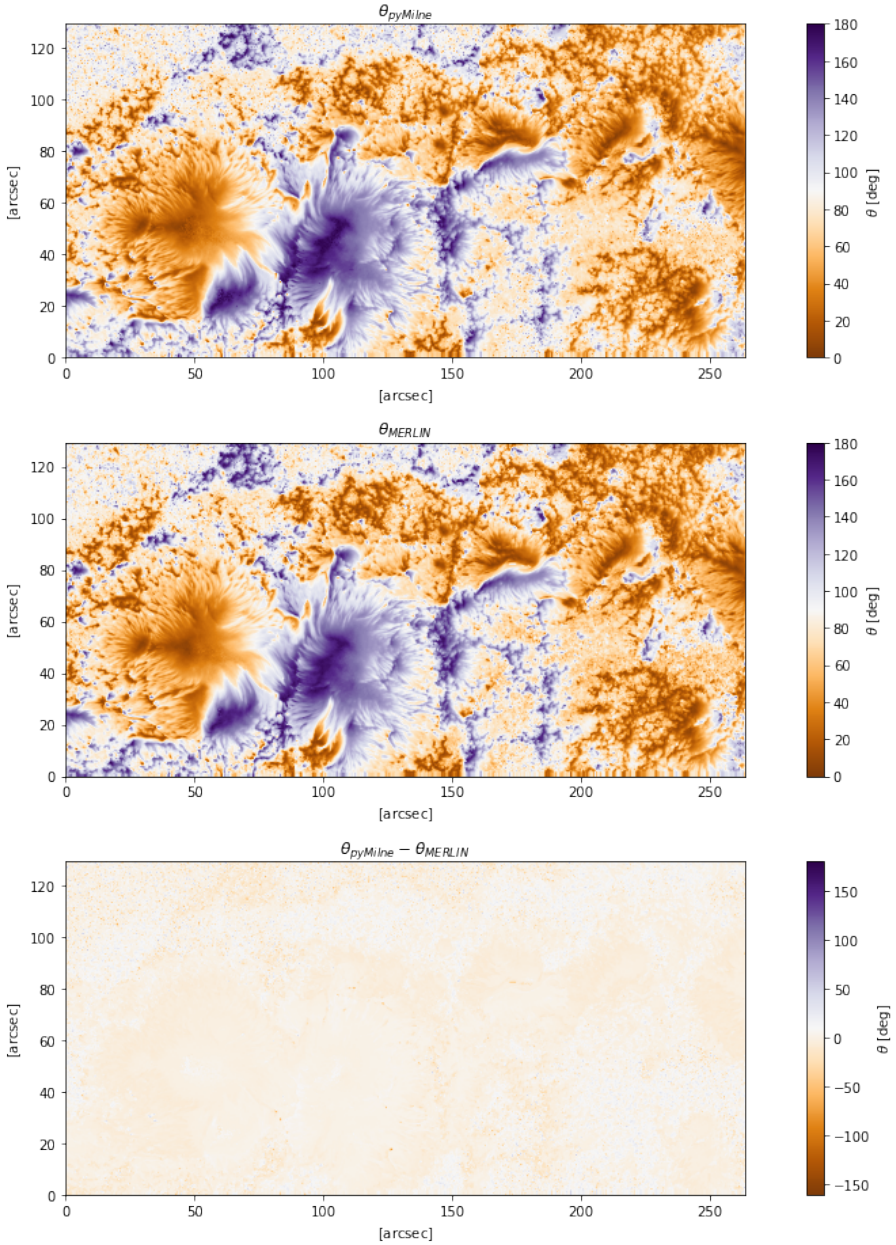

SOURCE: Author.

Figure 7.7 - On *left*, we have the magnitude of the magnetic field. And the *right*, the inclination map. Note that the strongest magnetic field has an inclination of approximately 90°.

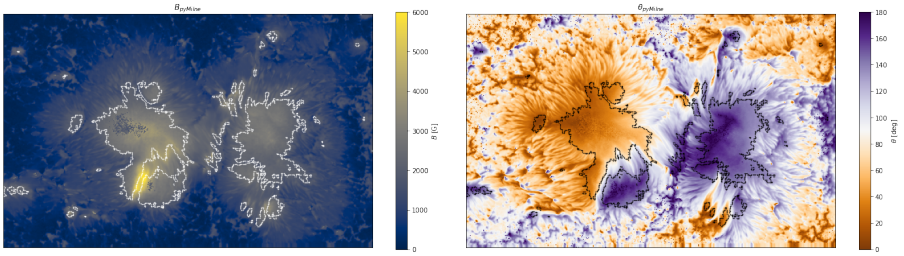

SOURCE: Author.

7.3.3 Azimuth

Figure 7.8, shows the azimuth map which is one of the most accurate results we got work (qualitatively speaking). At each point on the map, the azimuth ranges from 0° to 360°, but in this case the map is ambiguous and therefore the map ranges from 0° to 180°. The azimuth represents the projection angle of the vector $\mathbf{B}$ on the xy plane, and its angle is formed from the axis x to the projection of the vector $\mathbf{B}$

Note that qualitatively, the region where sunspots are found is almost zero in the difference map, see Figure 7.9 to get a better idea, in this Figure (7.9) the pyMilne azimuth map is shown on the left and the difference between the maps is shown on the right. It is possible to notice that the white tone occupies a large part of the difference map and the contours highlight the region where the sunspot umbras are located. Furthermore, the qualitative results shown in Table 7.4 show that the result obtained by pyMilne was accurate, as the values were very close for the avarage, median and kurtosis.

Note also that with the parameters B, θ and φ, the magnetic field vector $\mathbf{B}$ can be recovered. The inversion outputs these three atmospheric parameters that generate $\mathbf{B}$. However, the determination of the magnetic field from the Zeeman effect produces a non-unique solution for the azimuth component of the magnetic field vector. This occurs because the projection of the vector $\mathbf{B}$ on the axis x, y which are perpendicular to the line-of-sight, and over z which is parallel to the line-of-sight, generates the following components of the magnetic field:

$$B_x = |\mathbf{B}| \sin(\theta) \cos(\varphi), \tag{7.1}$$

$$B_y = |\mathbf{B}| \sin(\theta) \sin(\varphi), \tag{7.2}$$

$$B_z = |\mathbf{B}| \cos(\varphi), \tag{7.3}$$

$$\mathbf{B} \stackrel{\text{def}}{=} (B_x, B_y, B_z). \tag{7.4}$$

Through the so-called *weak field approximation*, we can obtain a relationship between the Stokes parameters Q and U which is given in Degl'iinnocenti and Landolfi (2004)

$$Q(\lambda) \propto \sin^2(\theta)\cos(2\varphi), \tag{7.5}$$

$$U(\lambda) \propto \sin^2(\theta)\sin(2\varphi). \tag{7.6}$$

According to Auer et al. (1977) a relationship between Q and U can also be obtained to express the azimuth angle, such a relationship is given by:

$$\varphi = \frac{1}{2}\arctan\left(\frac{U(\lambda)}{Q(\lambda)}\right). \tag{7.7}$$

Table 7.4 - Avarage, median and kurtosis of pyMilne and MERLIN results for azimuth.

	Average [°]	Median [°]	Kurtosis [°]
pyMilne	92.763176	98.0491	−1.3689976
MERLIN	93.167305	98.76111	−1.3595746

SOURCE: Author.

Figure 7.8 - Illustration of azimuth (with ambiguity) and the difference between azimuth. In *first line* the azimuth due to pyMilne, in *second line* the azimuth due to MERLIN, and in *third line* the difference between the azimuths ($\varphi_{pyMilne} - \varphi_{MERLIN}$).

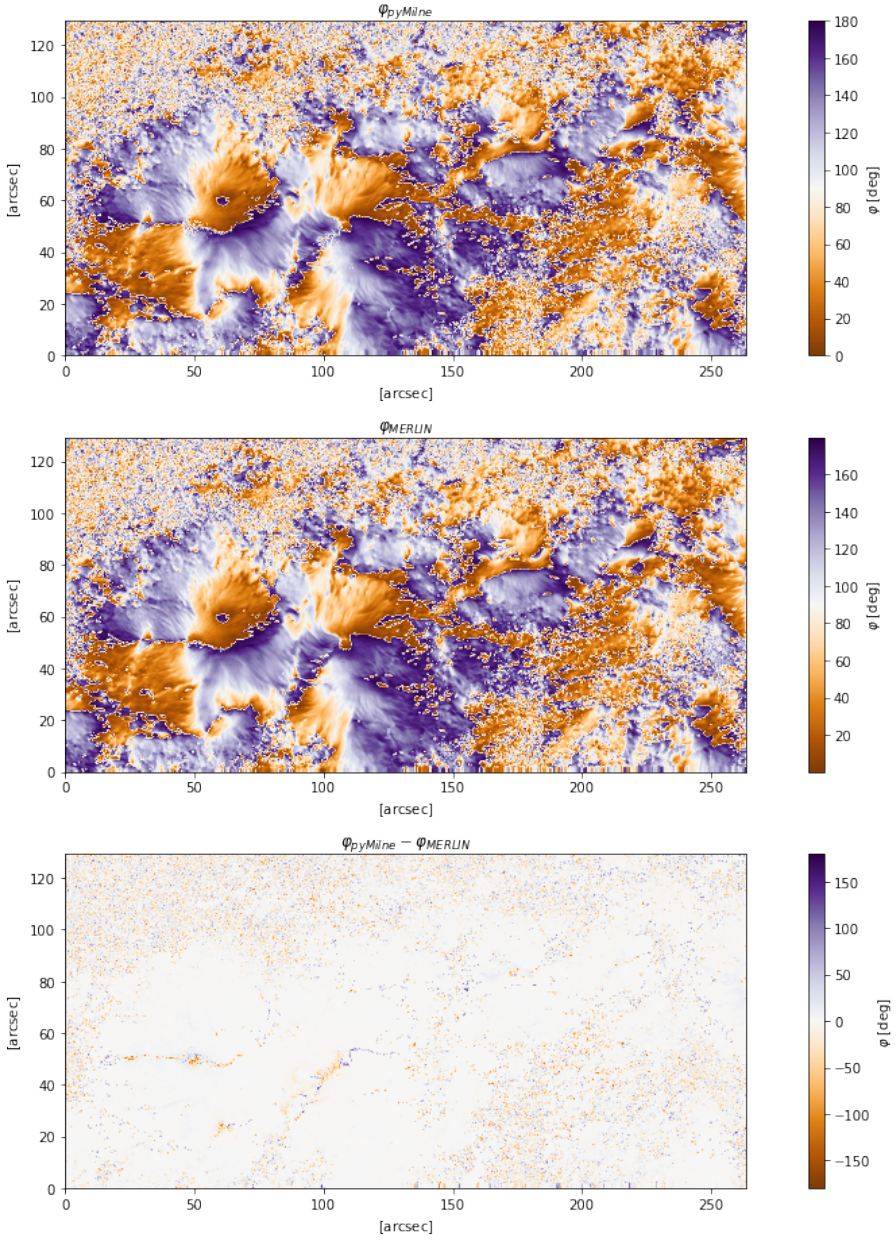

SOURCE: Author.

Figure 7.9 - Image highlighting the sunspot region (*left*) and the difference between maps $\varphi_{pyMilne} - \varphi_{MERLIN}$ (*right*). Note that a qualitative analysis shows that the maps of $\varphi_{pyMilne}$ and φ_{MERLIN} have small relative differences.

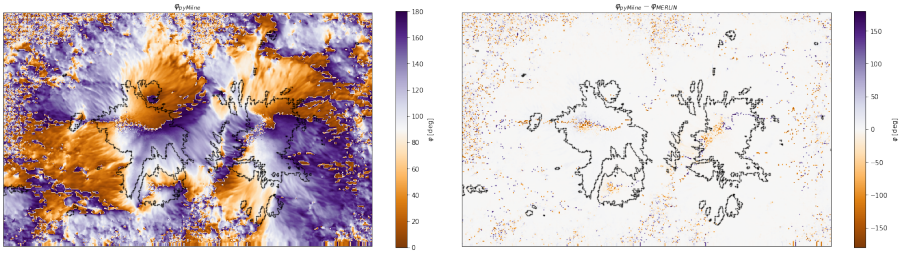

SOURCE: Author.

7.4 Other comparison methods

Figure 7.10 - Scatterplots of pyMilne results (vertical) and MERLIN results (horizontal). The red line represents one-to-one correspondence, and R^2 represents how accurate the statistical measure.

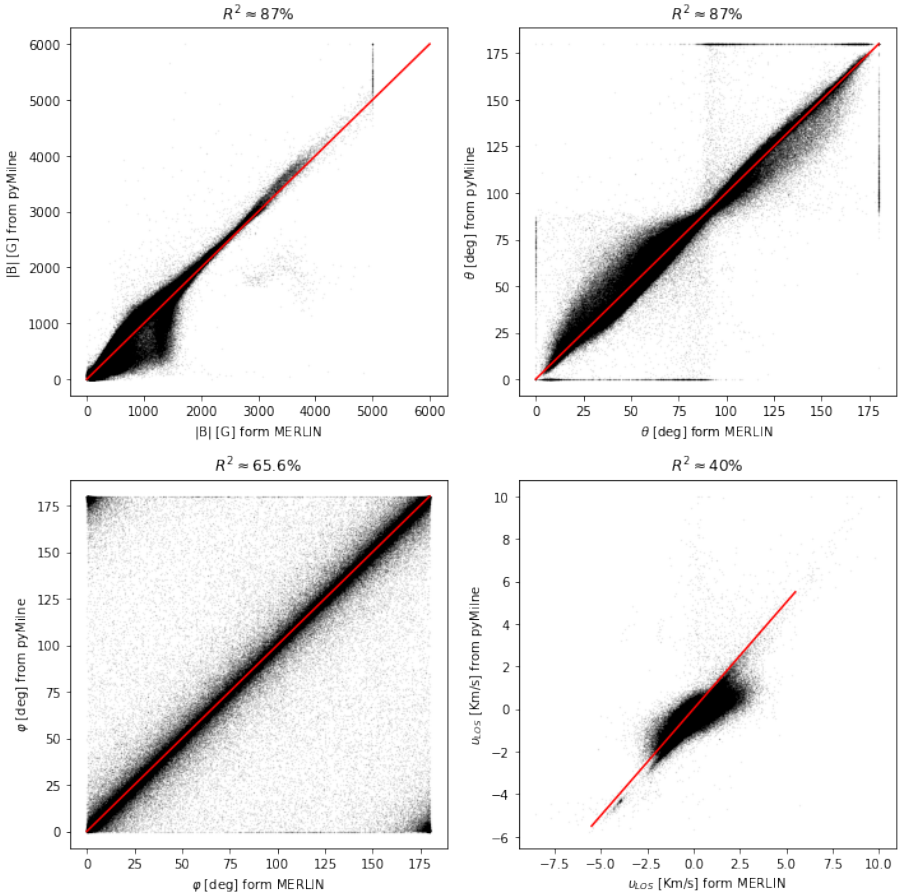

SOURCE: Author.

Another analysis that can be done to compare the results of inversion codes are scatter plots and histograms. Below, we compare the results of the two ME inversions, with the initial guess atmosphere given by $\mathbf{x} = [500, 0.1, 0.1, 0.0, 0.04, 100, 0.5, 0.1, 1.0]$. And we compared pyMilne with MERLIN using histogram and scatterplot methods.

In the previous section, we studied the following atmospheric parameters: B, θ, φ and υ_{LOS}, and the obtained images (maps) seen in the figures in the Section 7.3

(see Figures 7.3, 7.4, 7.6 and 7.8). In Figure 7.10, we present the scatter plots for each vector parameter B (in the first row and first column), θ (in the first row and second column), φ (second row and first column) and v_{LOS} (second row and second column) where the ME inversion codes are compared. On the vertical axis, pyMilne results and on the horizontal axis, MERLIN results. All scatter plots in Figure 7.10 have a red line representing one-to-one correspondence, in addition to having the statistical measure R^2 that indicates agreements between the results.

All scatter plots show satisfactory results at 7.10, with the exception of the v_{LOS} plot, which is below 50 %. The best concordances between pyMilne and MERLIN can be seen in the scatter plots of B and θ, whose concordance was $\approx$ 87 %. While in the φ scatter plot, the agreement was $\approx$ 65.6 % and for v_{LOS}, it was $\approx$ 40 % that presented many points of difference. The divergence points observed in the scatterplot of v_{LOS}, are probably due to the lack of correction (of rotation) in the map $v_{LOS,pyMilne}$. Also note that on the B scatterplot, the 5000 G points on the x axis (from MERLIN) begin to "accumulate"/clump together at the point 5000 G from the y axis (from pyMilne) to 6000 G, and this is another evidence that inversion algorithms have limits: from 5000 G for MERLIN, and 6000 G for pyMilne.

In general, it can be said that the inversion codes had a lot of agreement, with the exception of the scatterplot of v_{LOS}. Note that the scatterplot of B shows a small disagreement in a neighborhood of 1000 G for MERLIN and a neighborhood of a value below 1000 G ($\approx$ 700 G, say) to pyMilne before it got well behaved. The discordance between the points of the scatter plot of v_{LOS} can be visualized both in the graph and in the statistical mean $R^2 \approx 40\%$.

To complement the results obtained in the Section 7.3, where one map was subtracted from another, histograms can provide a quantitative interpretation of the observed events, because if we are dealing with images (matrixes composed of pixels with numerical values), then , histograms can indicate the number of pixels with a certain value that exist in the image being analyzed.

Figure 7.11 shows the histograms related to B in the first line, related to θ in the second line, related to φ in the third line, and in the fourth line, the histograms related to v_{LOS}. The first column corresponds to pyMilne results, the second column to MERLIN, the third culona is the histogram of the difference map (pyMilne - MERLIN), and the last column is the difference results but restricted to a certain range.

Figure 7.11 - Histograms. In the *first line*, the results related to B. In *second line*, results related to θ, in *third line*, results related to φ and in *fourth line*, results related to v_{LOS}. Also, in *first column*, you are asked to see results from pyMilne, in *second column*, those from MERLIN, and the differences can be seen in *third* and *fourth* column, with a range constraint on the histograms of B, θ, and v_{LOS}.

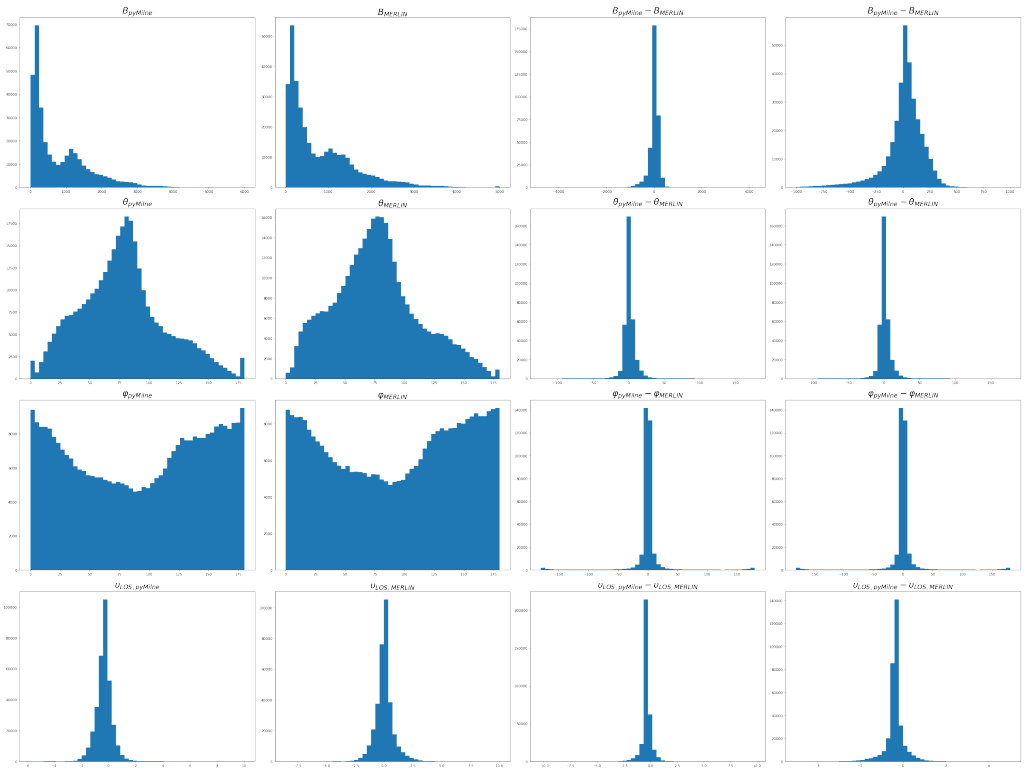

SOURCE: Author.

The similar shape of the histograms is not reproduced for the map of v_{LOS}, and therefore, it is possible to see that in the case of the histogram of $v_{LOS,pyMilne}$ it has a greater number of negative pixels (to the left of 0), which explains the predominantly blue coloring of the map $v_{LOS,pyMilne}$ in Figure 7.3. Considering that the histogram of $v_{LOS,MERLIN}$ has a greater number of positive pixels (to the right of 0), this may explain the predominantly red coloring in Figure 7.3. And so, the histogram of $v_{LOS,pyMilne} - v_{LOS,MERLIN}$, has the maximum shifted to the left of 0, and that explains the light blue color in the difference map $v_{LOS,pyMilne} - v_{LOS,MERLIN}$. Furthermore, the peak of the histogram $v_{LOS,pyMilne} - v_{LOS,MERLIN}$ shows this behavior in the full histogram (last row and third column) and in the constrained range histogram (last row and column in Figure 7.11).

The third columns of the first, second and third rows were peaked at 0 or close to 0 (in $\varphi_{pyMilne} - \varphi_{MERLIN}$ the range was not restricted as values other than 0 appeared, but less frequently). When the range was narrowed the peaks continued to appear in a neighborhood of 0. Thus, the histograms and scatter plots show that the results for B, θ and φ were accurate, while for v_{LOS} the accuracy was lower.

8 SUMMARY AND CONCLUSIONS

In this work, our main objective was the comparison between inversion codes, and the recovery of the solar magnetic field (and other less relevant parameters for this work) through the inversion process, in AR11967 on 04 of February 2014, around 19:00 UT and using the data obtained by the SOT/SP from the Hinode Mission. For this, we provide a theoretical basis on Zeeman effect, RTE, RTE Solution, Fe I spectral lines (6301.5 Å and 6302.5 Å) in addition to ME approach/atmosphere. For the inference of photospheric magnetic fields starting from the observations of polarization signals in the lines of the Fe I, the ME inversion codes for the RTE are widely used tools, and to fulfill the objectives of the work, we compared the results obtained by the ME inversion code MERLIN from the Hinode mission and compared with the results obtained by the ME pyMilne inversion code.

Initial analyzes were done by looking at AR1967 and defining the continuum to help with the analysis, and looking at points (pixels) from different regions. We found that the profiles had different behavior depending on the region analyzed, where in a region with a lot of magnetic activity such as the umbra and the region that resembles a lightbridge it is possible to observe the Stokes Q, U and V reaching relatively high values, In addition, low values of local minima were observed in Stokes I.

Next, we study the behavior of synthetic lines, that is, synthetic Stokes profiles that are used to compare with the observed ones, but in this case, we study them in isolation to observe their behavior in response to variations of the model atmosphere vector profiles, that is, in response to variations in B (magnetic field strength), θ (magnetic field inclination), φ (magnetic field azimuth) and v_{LOS} (line-of-sight velocity). With a model atmosphere $\mathbf{x}$, where only B varies, we observed how the Stokes profiles responded. The Stokes I was starting to divide and a forming local minimum and the Stokes Q was forming a local minimum in the vicinity of the lines (6301.5 Å or 6302.5 Å), while the U formed local maximums and the V behaved like an oscillation in the vicinity of the line frequencies. Such behavior is due to the Zeeman effect, which separated lines into components.

Assuming that the value of the magnetic field strength is positive, we study the behavior of my synthetics by varying other parameters such as θ, φ and v_{LOS}. As the slope increases the Stokes I forms new local minima (with $\approx 90^{\circ}$ we are in the umbra and several local minima appear). When the φ parameter varies, the only parameters that respond are Q and U. And finally, by varying the v_{LOS} parameter,

we can see that the line moves to the right with positive velocities and to the left with negative velocities.

The ME pyMilne code was used to invert the synthetic Stokes profiles and obtain the results classified as Level 2 data and thus compare with the Level 2 results obtained by MERLIN. For the inversion, the focus was on the second spectral line of $Fe\ I$, that is, 6302.5 Å. And for the comparison of Level 2 data, we used subtraction of maps, histograms, and scatter plots.

The noise was considered small, and so we entered an initial guess atmosphere, to start the inversion process. The parameters considered were B, θ, φ, υ_{LOS}, $\Delta\lambda$, η_0, a, S_0 and S_1.

Due to the χ^2 map, which is one of the outputs of the inversion, we were able to contact that some errors can be large when only one pixel is considered, but with a satisfactory and sufficiently good fitting. Other outputs of the inversion code are the synthetic Stokes parameters and the model atmosphere parameter maps.

Once we got our Level 2 data, we compared it to MERLIN's. First we subtract the pyMilne maps from the MERLIN maps. With this, we were able to make a qualitative analysis of the map resulting from the subtraction, and in addition, such maps presented values close to zero. However, this alone was not enough to draw conclusions, so the need arose to proceed in such a way that the conclusions were more rigorous.

Therefore, the means, medians and costs were calculated for the parameters B, θ, φ υ_{LOS}. In addition, we also proceeded by assembling the scatter plots and histograms of the inversion codes, and of the differences between the maps.

In Tables 7.2, 7.3 and 7.4 the values of average, median, and kurtosis of pyMilne and MERLIN are very close and this indicates a similar behavior of the results of pyMilne and MERLIN. The only results that diverged were those from υ_{LOS}, where both the difference map ($\upsilon_{LOS,pyMilne} - \upsilon LOS, MERLIN$), and the statistics from Table 7.1 presented very distant values, which led us to theorize that it was necessary to apply a rotation correction value to the pyMilne map so that the result would be more similar to what was observed by the Hinode Mission.

Regarding the scatter plots, the parameters showed a concordance of (by means of the statistical measure R^2), of $R^2 \approx 87\%$ for B and for θ, and from $R^2 \approx 65.6\%$ to φ, the values are considered good and indicate how close the results of pyMilne

and MERLIN were. Furthermore, it can also be observed that the histograms of B, θ, and φ, have the same shape and the histograms of the differences, that is, $B_{pyMilne} - B_{MERLIN}$, $\theta_{pyMilne} - \theta_{MERLIN}$ and $\varphi_{pyMilne} - \varphi_{MERLIN}$, peaked close to zero.

However, as we said before, a correction factor is needed for v_{LOS}, which was missing, since the result of the map $v_{LOS,pyMilne} - v_{LOS,MERLIN}$, was not as close to zero as it should be, and besides, it is possible to see in the histograms of v_{LOS} that the map for pyMilne has more pixels with negative than positive speeds (and the same occurs for the MERLIN map). The histograms show the same behavior, as the $v_{LOS,pyMilne}$ histogram has more negative than positive values and the $v_{LOSM,MERLIN}$ histogram has more positive than negative values, and the difference shows a predominance of negative values in the histogram, which helps to explain the blue color observed in the map $v_{LOS,pyMilne} - v_{LOS,MERLIN}$. not to mention that the agreement in the scatter plot is $R^2 \approx 40$ %. But, such results can be corrected with the rotation correction factor.

In other words, we can conclude that, apart from the correction that can be applied in v_{los}, the ME inversion code pyMilne, presented excellent results, since the maps of B, θ and φ showed concordance in the scatter plots (R^2), in the statistical tables, and the histograms. Furthermore, pyMilne was able to obtain more accurate results than MERLIN for solar magnetic fields, as recent work by Durán et al. (2020) and Okamoto and Sakurai (2018) has shown a magnetic field of approximately 6.2 kG in the region resembling a lightbridge, while the code MERLIN got a result of 5000 kG in the region in question, pyMilne was able to get a value much closer to the mentioned value. The value pyMilne got was 6000 kG. That is, pyMilne is a very accurate inversion code.

REFERENCES

AGOSTINI, M.; ALTENMÜLLER, K.; APPEL, S.; ATROSHCHENKO, V.; BAGDASARIAN, Z.; BASILICO, D.; BELLINI, G.; BENZIGER, J.; BIONDI, R.; BRAVO, D.; CACCIANIGA, B.; CALAPRICE, F.; CAMINATA, A.; CAVALCANTE, P.; CHEPURNOV, A.; D'ANGELO, D.; DAVINI, S.; DERBIN, A.; GIACINTO, A. D.; MARCELLO, V. D.; DING, X. F.; LUDOVICO, A. D.; NOTO, L. D.; DRACHNEV, I.; FORMOZOV, A.; FRANCO, D.; GALBIATI, C.; GHIANO, C.; GIAMMARCHI, M.; GORETTI, A.; GÖTTEL, A. S.; GROMOV, M.; GUFFANTI, D.; IANNI, A.; IANNI, A.; JANY, A.; JESCHKE, D.; KOBYCHEV, V.; KORGA, G.; KUMARAN, S.; LAUBENSTEIN, M.; LITVINOVICH, E.; LOMBARDI, P.; LOMSKAYA, I.; LUDHOVA, L.; LUKYANCHENKO, G.; LUKYANCHENKO, L.; MACHULIN, I.; MARTYN, J.; MERONI, E.; MEYER, M.; MIRAMONTI, L.; MISIASZEK, M.; MURATOVA, V.; NEUMAIR, B.; NIESLONY, M.; NUGMANOV, R.; OBERAUER, L.; OREKHOV, V.; ORTICA, F.; PALLAVICINI, M.; PAPP, L.; PELICCI, L.; PENEK, Ö.; PIETROFACCIA, L.; PILIPENKO, N.; POCAR, A.; RAIKOV, G.; RANALLI, M. T.; RANUCCI, G.; RAZETO, A.; RE, A.; REDCHUK, M.; ROMANI, A.; ROSSI, N.; SCHÖNERT, S.; SEMENOV, D.; SETTANTA, G.; SKOROKHVATOV, M.; SINGHAL, A.; SMIRNOV, O.; SOTNIKOV, A.; SUVOROV, Y.; TARTAGLIA, R.; TESTERA, G.; THURN, J.; UNZHAKOV, E.; VILLANTE, F. L.; VISHNEVA, A.; VOGELAAR, R. B.; FEILITZSCH, F. von; WOJCIK, M.; WURM, M.; ZAVATARELLI, S.; ZUBER, K.; ZUZEL, G. Experimental evidence of neutrinos produced in the cno fusion cycle in the sun. **Nature**, v. 587, n. 7835, p. 577–582, 2020. Available from: <https://doi.org/10.1038/s41586-020-2934-0>. 5, 9

ASCHWANDEN, M. J. **New millennium solar physics**. [S.l.]: Springer, 2018. (Astrophysics and Space Science Library). ISBN 978-3-030-13956-8. 54, 56, 59

AUER, L.; HEASLEY, J.; HOUSE, L. Non-lte line formation in the presence of magnetic fields. **Astrophysical Journal**, v. 216, p. 531–539, 1977. Available from: <https://ui.adsabs.harvard.edu/abs/1977ApJ...216..531A/abstract>. 114

BASU, S.; ANTIA, H. Changes in solar dynamics from 1995 to 2002. **The Astrophysical Journal**, v. 585, n. 1, 2003. 10

BASU, S.; ANTIA, H. M. Helioseismology and solar abundances. 2007. Available from: <https://arxiv.org/abs/0711.4590>. 5

BERGER, T. **Hinode solar optical telescope data analysis guide: version 3.3**. [s.n.], 2009. Available from: <https://hesperia.gsfc.nasa.gov/ssw/hinode/sot/doc/guide/SAGv3.3.pdf>. 66, 67

BORRERO, J.; LITES, B.; LAGG, A.; REZAEI, R.; REMPEL, M. Comparison of inversion codes for polarized line formation in mhd simulations i. milne-eddington codes. **Astronomy & Astrophysics**, v. 572, n. A54, p. 13, 2014. Available from: <https://doi.org/10.1051/0004-6361/201424584>. 95, 96

BRUN, A.; REMPEL, M. Large scale flows in the solar convection zone. **Space Science Reviews**, v. 144, n. 151–173, 2009. 11

CENTENO, R. **The idiosyncrasies of Milne-Eddington inversions**. 2020. Available from: <https://drive.google.com/file/d/1gYRH4K7uKxE0uKjA0bfBxaWgmAS8_-1K/view>. 72, 73

CHARBONNEAU, P. Dynamo models of the solar cycle. **Living Reviews in Solar Physics**, v. 17, 2020. Available from: <https://doi.org/10.1007/s41116-020-00025-6>. 12, 13

CHARBONNEAU, P.; CHRISTENSEN-DALSGAARD, J.; HENNING, R.; LARSEN, R.; SCHOU, J.; THOMPSON, M.; TOMCZYK, S. Helioseismic constraints on the structure of the solar tachocline. **American Astronomical Society**, v. 527, n. 1, p. 445–460, 1999. 10

CHIPMAN, R. A.; LAM, W.-S. T.; YOUNG, G. **Polarized light and optical systems**. [S.l.]: CRC Press, 2018. 1036 p. ISBN 9781351129121. 28, 29

COBO, B.; INIESTA, J. del T. Inversion of stokes profiles. **Astrophysical Journal**, v. 398, p. 375 – 385, 1992. Available from: <https://ui.adsabs.harvard.edu/link_gateway/1992ApJ...398..375R/doi:10.1086/171862>. 30

CULHANE, J.; HARRA, L.; JAMES, A.; AL-JANABI, K.; BRADLEY, L.; CHAUDRY, R.; REES, K.; TANDY, J.; THOMAS, P.; WHILLOCK, M.; WINTER, B.; DOSCHEK, G.; KORENDYKE, C.; BROWN, C.; MYERS, S.; MARISKA, J.; SEELY, J.; LANG, J.; KENT, B.; SHAUGHNESSY, B.; YOUNG, P.; SIMNETT, G.; CASTELLI, C.; MAHMOUD, S.; MAPSON-MENARD, H.; PROBYN, B.; THOMAS, R.; DAVILA, J.; DERE, K.; WINDT, D.; SHEA, J.; HAGOOD, R.; MOYE, R.; HARA, H.; WATANABE, T.; MATSUZAKI, K.;

KOSUGI, T.; HANSTEEN, V.; WIKSTOL, Ø. The euv imaging spectrometer for hinode. **Solar Physics**, v. 243, n. 1, 2007. 56

DEGL'IINNOCENTI, E. L.; LANDOLFI, M. **Polarizaton in spectral line**. [S.l.]: Springer Dordrecht, 2004. (Astrophysics and Space Science Library). ISBN 1-4020-2415-0. 35, 113

DEGL'INNOCENTI, E. L. **Fisica solare**. [S.l.]: Springer, 2007. (Collana di Fisica e Astronomia). ISBN 978-88-470-0677-5. 5, 9

_____. **Atomic spectroscopy and radiative processes**. [S.l.]: Springer Milano, 2014. (UNITEXT for Physics). ISBN 978-88-470-2808-1. 35, 36

DURÁN, S. C.; LAGG, A.; SOLANKI, S.; NOORT, M. Detection of the strongest magnetic field in a sunspot light bridge. **The Astrophysical Journal**, v. 895, n. 2, p. 18, 03 2020. 13, 83, 97, 123

EINSTEIN, A. Ist die trägheit eines körpers von seinem energieinhalt abhängig? **Annalen der Physik**, v. 323, n. 1, p. 639—641, 1905. 5

EUROPEAN SPACE AAGENCY (ESA). **Secrets for solar orbiter to solve**. 2020. Available from: <https://www.esa.int/Science_Exploration/Space_Science/Solar_Orbiter/Secrets_for_Solar_Orbiter_to_solve>. Access in: Mar. 7, 2022. 3

FRANZ, M. **Spectropolarimetry of sunspot penumbrae a comprehensive study of the evershed effect using high resolution data from the space-borne solar observatory HINODE**. 164 p. Dissertation — Kiepenheuer Institut für Sonnenphysik, Freiburg im Breisgau, 2011. Available from: <http://www.leibniz-kis.de/fileadmin/user_-upload/forschung/publikationen/dissertation/Dissertation_Franz.pdf>. Access in: July 28, 2021. 4, 43, 54

GOLUB, L.; DELUCA, E.; AUSTIN, G.; BOOKBINDER, J.; CALDWELL, D.; CHEIMETS, P.; CIRTAIN, J.; COSMO, M.; REID, P.; SETTE, A.; WEBER, M.; SAKAO, T.; KANO, R.; SHIBASAKI, K.; HARA, H.; TSUNETA, S.; KUMAGAI, K.; TAMURA, T.; SHIMOJO, M.; MCCRACKEN, J.; CARPENTER, J.; HAIGHT, H.; SILER, R.; WRIGHT, E.; TUCKER, J.; RUTLEDGE, H.; BARBERA, M.; PERES, G.; VARISCO, S. The x-ray telescope (xrt) for the hinode mission. **Solar Physics**, v. 243, n. 1, 2007. 56

HALE, G. On the probable existence of a magnetic field in sun-spots. **Astrophysical Journal**, v. 28, p. 315–343, 1908. 11

(HAO), H. A. O. **CSAC SPECTRAL LINE INVERSIONS**. 2020. Available from: <https://www2.hao.ucar.edu/csac/csac-spectral-line-inversions>. 76

_____. **SP data products**. 2022. Available from: <https://www2.hao.ucar.edu/csac/csac-data/sp-data-description>. 67

HARA, H. Coronal heating: Issues revealed from hinode observations. In: SHIMIZU, T.; IMADA, S.; KUBO, M. (Ed.). **First ten years of hinode solar on-orbit observatory**. [S.l.]: Springer, 2018, (Astrophysics and Space Science Library). p. 65–77. 16, 17, 18

HARRA, L. The first decade of hinode: Understanding coronal mass ejections. In: **first ten years of hinode solar on-orbit observatory**. [S.l.]: Springer, 2018, (Astrophysics and Space Science Library). p. 149–159. 15

HOEKSEMA, J. T.; LIU, Y.; HAYASHI, K.; SUN, X.; SCHOU, J.; COUVIDAT, S.; NORTON, A.; BOBRA, M.; CENTENO, R.; LEKA, K. D.; BARNES, G.; TURMON, M. The helioseismic and magnetic imager (hmi) vector magnetic field pipeline: overview and performance. **Solar Physics**, v. 289, p. 3484–3530, 2014. Available from: <https://link.springer.com/article/10.1007/s11207-014-0516-8>. 69

ICHIMOTO, K.; LITES, B.; ELMORE, D.; SUEMATSU, Y.; TSUNETA, S.; KATSUKAWA, Y.; SHIMIZU, T.; SHINE, R.; TARBELL, T.; TITLE, A.; KIYOHARA, J.; SHINODA, K.; CARD, G.; LECINSKI, A.; STREANDER, K.; NAKAGIRI, M.; MIYASHITA, M.; NOGUCHI, M.; HOFFMANN, C.; CRUZ, T. Polarization calibration of the solar optical telescope onboard hinode. **Solar Physics**, v. 249, n. 2, 2008. 58, 61, 62, 63, 64, 65

INIESTA, J. C. del T. **Introduction to spectropolarimetry**. [S.l.]: Cambridge University Press, 2003. ISBN 0-511-03920-4. 19, 23, 41, 42, 43, 44, 46, 48, 49, 73, 74, 75

INIESTA, J. del T.; COBO, B. Inversion of the radiative transfer equation for polarized light. **Living Reviews in Solar Physics**, v. 13, 2016. Available from: <https://doi.org/10.1007/s41116-016-0005-2>. 48, 50, 73

KANO, R.; SAKAO, T.; HARA, H.; TSUNETA, S.; MATSUZAKI, K.; KUMAGAI, K.; SHIMOJO, M.; MINESUGI, K.; SHIBASAKI, K.; DELUCA, E.; GOLUB, L.; BOOKBINDER, J.; CALDWELL, D.; CHEIMETS, P.; CIRTAIN, J.; DENNIS, E.; KENT, T.; WEBER, M. The hinode x-ray telescope (xrt): camera design, performance and operations. **Solar Physics**, v. 249, n. 2, 2007. 56

KOSUGI, T.; MATSUZAKI, K.; SAKAO, T.; SHIMIZU, T.; SONE, Y.; TACHIKAWA, S.; HASHIMOTO, T.; MINESUGI, K.; OHNISHI, A.; YAMADA, T.; TSUNETA, S.; HARA, H.; ICHIMOTO, K.; SUEMATSU, Y.; SHIMOJO, M.; WATANABE, T.; SHIMADA, S.; DAVIS, J.; HILL, L.; OWENS, J.; TITLE, A.; CULHANE, J.; HARRA, L.; DOSCHEK, G.; GOLUB, L. The hinode (solar-b) mission: an overview. **Solar Physics**, v. 243, n. 1, 2007. 1, 53, 55, 56, 60

KUBO, M. New insights into sunspots through hinode observations. In: SHIMIZU, T.; IMADA, S.; KUBO, M. (Ed.). **First ten years of hinode solar on-orbit observatory**. Singapore: Springer Singapore, 2018, (Astrophysics and Space Science Library). p. 105–114. ISBN 978-981-10-7742-5. Available from: <https://doi.org/10.1007/978-981-10-7742-5_10>. 12

LEKA, K.; BARNES, G.; CROUCH, A. An automated ambiguity-resolution code for hinode/sp vector magnetic field data. In: **HINODE SCIENCE MEETING: BEYOND DISCOVERY-TOWARD UNDERSTANDING ASP CONFERENCE**. [s.n.], 2009. v. 415, p. 365–368. Available from: <https://ui.adsabs.harvard.edu/abs/2009ASPC..415..365L/abstract>. 69

LITES, B.; AKIN, D.; CARD, G.; CRUZ, T.; DUNCAN, D.; EDWARDS, C.; ELMORE, D.; HOFFMANN, C.; KATSUKAWA, Y.; KATZ, N.; KUBO, M.; ICHIMOTO, K.; SHIMIZU, T.; SHINE, R.; STREANDER, K.; SUEMATSU, A.; TARBELL, T.; TITLE, A.; TSUNETA, S. The hinode spectro-polarimeter. **Solar Physics**, v. 283, n. 579–599, 2013. 30, 57, 58

LITES, B.; CASINI, R.; GARCIA, J.; SOCAS-NAVARRO, H. A suite of community tools for spectro-polarimetric analysis. **Memorie della Società Astronomica Italiana**, v. 78, p. 6, 2007. Available from: <https://ui.adsabs.harvard.edu/abs/2007MmSAI..78..148L/abstract>. 1, 76

MATSUZAKI, K.; SHIMOJO, M.; TARBELL, T.; HARRA, L.; DELUCA, E. Data archive of the hinode mission. **Solar Physics**, v. 243, n. 1, 2007. Available from: <https://link.springer.com/article/10.1007/s11207-006-0303-2>. 66, 67, 68

METCALF, T. Resolving the 180-degree ambiguity in vector magnetic field measurements: the 'minimum' energy solution. **Solar Physics**, v. 155, p. 235–242, 1994. Available from: <https://ui.adsabs.harvard.edu/abs/1994SoPh..155..235M/abstract>. 69

MIESCH, M. Large-scale dynamics of the convection zone and tachocline. **Living Reviews in Solar Physics**, v. 2, n. 1, 2005. 10

MITALAS, R.; SILLS, K. R. On the photon diffusion time scale for the sun. **Astrophysical Journal**, v. 401, p. 759–760, 1992. Available from: <https://ui.adsabs.harvard.edu/abs/1992ApJ...401..759M/abstract>. 9

NARAYANAN, A. S. **An introduction to waves and oscillations in the Sun**. [S.l.]: Springer, 2013. (Astronomy and Astrophysics Library). ISBN 978-1-4614-4400-8. 5, 11, 14, 15, 16

NATIONAL SCHOOLS' OBSERVATORY (NSO). **Hertzsprung-Russel diagram**. 2022. Available from: <https://www.schoolsobservatory.org/learn/astro/stars/class/hrdiagram>. Access in: Oct. 26, 2022. 4

NORDLUND, A.; STEIN, R. F.; ASPLUND, M. Solar surface convection. **Living Reviews in Solar Physics**, v. 6, Dec 2009. Available from: <https://doi.org/10.12942/lrsp-2009-2>. 30

OKAMOTO, T. J.; SAKURAI, T. Super-strong magnetic field in sunspots. **The Astrophysical Journal**, v. 852, n. 1, p. L16, jan 2018. Available from: <https://doi.org/10.3847/2041-8213/aaa3d8>. 13, 14, 79, 83, 97, 123

PARKER, E. N. The formation of sunspots from the solar toroidal field. **Astrophysical Journal**, v. 121, p. 491–507, 1955. Available from: <https://ui.adsabs.harvard.edu/link_gateway/1955ApJ...121..491P/doi:10.1086/146010>. 13

_____. Topological dissipation and the small-scale fields in turbulent gases. **The Astrophysical Journal**, v. 174, p. 499, 1972. 17

_____. The generation of magnetic fields in astrophysical bodies. x. magnetic buoyancy and the solar dynamo. **Astrophysical Journal**, v. 198, p. 205–209, 1975. Available from: <https://ui.adsabs.harvard.edu/link_gateway/1975ApJ...198..205P/doi:10.1086/153593>. 13

_____. Nanoflares and the solar x-ray corona. **Astrophysical Journal**, v. 330, p. 474, 1988. 17

RODRÍGUEZ, J. de la C. A method for global inversion of multi-resolution solar data. **Astronomy & Astrophysics**, v. 631, n. A153, p. 12, 2019. Available from: <https://doi.org/10.1051/0004-6361/201936635>. 1, 77, 78, 79, 90, 95

RUSSELL, H.; SAUNDERS, F. New regularities in the spectra of the alkaline earths. **The Astrophysical Journal**, v. 61, p. 38, 1925. Available from: <https://ui.adsabs.harvard.edu/abs/1925ApJ....61...38R/abstract>. 36

SAKURAI, T. Hinode's contributions to solar physics. In: SHIMIZU, T.; IMADA, S.; KUBO, M. (Ed.). **first ten years of hinode solar on-orbit observatory**. Singapore: Springer Singapore, 2018. p. 19–26. ISBN 978-981-10-7742-5. Available from: <https://doi.org/10.1007/978-981-10-7742-5_2>. 53, 105, 109

SANTIAGO, J. M. B. **The fine structure of the sunspot penumbra**. 153 p. Dissertation (Doktorgrades - Mathematisch–Naturwissenschaftlichen) — Fakultäten der Georg–August–Universität zu Göttingen, 2004. 51

SEVERINO, G. **The structure and evolution of the Sun**. [S.l.]: Springer, 2017. (Undergraduate Lecture Notes in Physics). ISBN 978-3-319-64961-0. 5, 9

SHELYAG, S. **Spectro-polarimetric diagnostics of magneto-convection simulations of the solar photosphere**. 105 p. Dissertation (Doktorgrades - Mathematisch-Naturwissenschaftlichen) zur Erlangung des Doktorgrades — Fakultäten der Georg-August-Universität zu Göttingen, 2004. 30

SHENSTONE, A.; BLAIR, H. A method for the magnetic analysis of a spectrum by means of unresolved zeeman patterns, and its application to *ag ii*. **The London, Edinburgh, and Dublin Philosophical Magazine and Journal of Science**, v. 8, n. 52, p. 765–771, 1929. Available from: <https://doi.org/10.1080/14786441108564938>. 39

SHIBATA, K.; CHEN, P. An emerging flux trigger mechanism for coronal mass ejections. **The Astrophysical Journal**, v. 545, n. 1, 2000. Available from: <https://iopscience.iop.org/article/10.1086/317803>. 15

SHIMIZU, T.; NAGATA, S.; TSUNETA, S.; TARBELL, T.; EDWARDS, C.; SHINE, R.; HOFFMANN, C.; THOMAS, E.; SOUR, S.; REHSE, R.; ITO, O.; KASHIWAGI, Y.; TABATA, M.; KODEKI, K.; NAGASE, M.; MATSUZAKI, K.;

KOBAYASHI, K.; ICHIMOTO, K.; SUEMATSU, Y. Image stabilization system for hinode (solar-b) solar optical telescope. **Solar Physics**, v. 249, n. 2, 2007. 55

SILVA, A. C. A. **Evolution of active regions based on solar-surface magnetic flux observations and coronal magnetic fields extrapolations: a case-study of NOAA 12443**. 155 p. Dissertation (master in Space Geophysics) — Instituto Nacional de Pesquisas Espaciais - INPE, São José dos Campos, 2017. Available from: <http://www.inpe.br/posgraduacao/ges/arquivos/dissertacoes/dissertacao$_$andre$_$chicrala$_$2017.pdf>. 86

SOLANKI, S. Sunspots: an overview. **The Astronomy and Astrophysics Review**, v. 11, 2003. 11, 12

SOLANKI, S. K. **The photospheric layers of solar magnetic fluxtubes**. 191 p. Dissertation (PhD in natural Science) — Swiss Federal Institute of Technology, Zürich, 1987. 43

STEKEL, T. R. C. **Study of magnetic structures of an arch filament system in the photosphere and chromosphere**. 208 p. Thesis (PhD in Space Geophysics) — Instituto Nacional de Pesquisas Espaciais - INPE, São José dos Campos, 2019. 24, 32, 38, 40, 47, 50

SUÁREZ, D.; BELLOT-RUBIO, L.; INIESTA, J. del T. Milne-eddington inversion of the $fe\ i$ line pair at 630 nm (research note). **Astronomy & Astrophysics**, v. 518, n. A3, 2010. Available from: <https://doi.org/10.1051/0004-6361/201014374>. 30

SUÁREZ, D.; INIESTA, J. del T. The usefulness of analytic response functions*. **Astronomy & Astrophysics**, v. 462, n. 3, p. 1137 – 1145, 2007. Available from: <https://doi.org/10.1051/0004-6361:20066201>. 30

TAPIA, A. L. S. **Normal and counter Evershed flows in the penumbra of sunspots: HINODE observations and MHD simulations**. 183 p. Dissertation — Mathematisch-Naturwissenschaftlichen Fakultäten der Georg-August University School of Science (GAUSS), Göttingen, Germany, 2018. 33

TOBIAS, S. The solar tachocline: Formation, stability and its role in the solar dynamo. In: **Fluid dynamics and dynamos in astrophysics and geophysics**. [S.l.]: CRC press, 2005. 10

TOBIAS, S.; WEISS, N. The solar dynamo and the tachocline. In: **The solar tachocline**. Cambridge University Press (CUP), 2007. Available from: <https://doi.org/10.1017/CBO9780511536243>. 10

TSUNETA, S.; ICHIMOTO, K.; KATSUKAWA, Y.; NAGATA, S.; OTSUBO, M.; SHIMIZU, T.; SUEMATSU, Y.; NAKAGIRI, M.; NOGUCHI, M.; TARBELL, T.; TITLE, A.; SHINE, R.; ROSENBERG, W.; HOFFMANN, C.; JURCEVICH, B.; KUSHNER, G.; LEVAY, M.; LITES, B.; ELMORE, D.; MATSUSHITA, T.; KAWAGUCHI, N.; SAITO, H.; MIKAMI, I.; HILL, L.; OWENS, J. The solar optical telescope for the hinode mission: an overview. **Solar Physics**, v. 249, n. 2, 2008. 55, 57, 61

WIEGELMANN, T.; THALMANN, J.; SOLANKI, S. The magnetic field in the solar atmosphere. **The Astronomy and Astrophysics Review**, v. 22, n. 1, 2014. 14

ZEEMAN, P. On the influence of magnetism on the nature of the light emitted by a substance. **Astrophysical Journal**, v. 5, p. 332–347, 1897. Available from: <https://adsabs.harvard.edu/full/1897ApJ.....5..332Z>. 31